Nonlinear Weighted Immersed Boundary Method for Numerical Analysis in Compressible Flow

압축성 유동에서의 수치해석을 위한 가중치
가상경계기법 연구

2021 년 2 월

서울대학교 대학원

기계항공공학부

정한아침

Nonlinear Weighted Immersed Boundary Method for Numerical Analysis in Compressible flow

압축성 유동에서의 수치해석을 위한 가중치 가상경계기법 연구

지도교수 이 수 갑

이 논문을 공학박사 학위논문으로 제출함

2020 년 10 월

서울대학교 대학원
기계항공공학부
정한아침

정한아침의 공학박사 학위논문을 인준함
2020 년 12 월

위 원 장 : 李 福 植

부위원장 : 李 和 甲

위　　원 : 이 승 수

위　　원 : 김 상 호

위　　원 : 정 희 석

Nonlinear Weighted Immersed Boundary Method for Numerical Analysis in Compressible Flow

Hanahchim Choung

Department of Aerospace Engineering

Seoul National University

Abstract

Computational challenges arise for the immersed boundary method (IBM) when dealing with compressible flow, where discontinuous and smoothly varying flow regions appear near the immersed boundary. In this study, a new ghost-cell approach, nonlinear-weighted IBM (NWIBM), is developed to address the issues that the conventional ghost-cell IBM provides inaccurate results for smoothly varying regions when a low-order interpolation is used, or it suffers from a numerical instability for the discontinuous flow when a high-order interpolation is used. Inspired by a variety of weighted nonoscillatory interpolation methods, this work combines the high- and low-order polynomials during ghost-cell value estimation to enforce proper boundary conditions in the immersed boundary. A multidimensional smoothness indicator is designed to evaluate flow discontinuities. The nonlinear weighting obtained from the smoothness indicator makes the high-order polynomial dominant and the low-order polynomial negligible in the smoothly varying region, and vice versa in the discontinuous region. In addition, flow field reconstruction method is also addressed for the nearest the ghost cell with smoothness condition satisfied in order to reduce the jump-discontinuity that causes spurious oscillations in the conventional IBM. The enhanced performance and applicability of the proposed method were validated through various numerical tests in compressible

flow. It was demonstrated that the NWIBM provides more stable and accurate numerical solutions compared with conventional ghost-cell approaches.

Contents

Chapter 1. Introduction

1.1 Background

Conventional boundary conforming grid approaches such as body-fitted and unstructured grid methods need complex grid generation and demanding re-meshing process in deforming bodies, which results in computational cost increment. As the demand for efficient calculation in computational analysis gradually increases, the immersed boundary method (IBM) has attracted much attention because of its flexibility in treating complex geometries.

The IBM, also known as the "immersed interface method," "embedded boundary method," and "level-set method," has evolved and been modified to solve grid-based computational fluid dynamics problems since it was introduced by Peskin [1], and it has two key advantages. One is the flexibility to treat geometries in a stationary Cartesian coordinate system, regardless of geometrical complexity and deformation, which overcomes the complex grid generation process. The other one is the use of straightforward governing equations without transformations with respect to the geometry, which makes the algorithm simple and enhances code efficiency.

In general, IBMs are classified into diffuse or sharp interface methods in terms of their realization of the fluid–solid interface [2]. The diffuse interface methods function by smearing the geometry into the surrounding grids by disturbing singular forces. Although the diffuse interface type [3–7] has the advantage of easy implementation because it does not adhere to spatial discretization, it cannot accurately track the interface but is rather "diffused" within the localized area. The sharp interface method [8–30] can precisely describe the complex or thin interface, strongly coupled with the boundary interface. Cut-cell [8–11], ghost-cell [12–28], and many other versions [28,29] of sharp interface methods are being developed.

Similar to the other numerical schemes, each type of sharp interface IBM also has its advantages and disadvantages. The cut-cell method, which is known for its good accuracy and conservation property, produces unstructured cells that make the algorithm cumbersome and high-order extension problematic [2]. However, the ghost-cell method is straightforward in implementation and high-order extension. Although it does not necessarily ensure the conservation property by its finite-

difference characteristics, the ghost-cell approach has been used widely because of its suitability and efficiency to analyze moving complex geometry. This is because it requires no cell-reshaping procedure for the newly emerged cells. Flow-reconstructed [28,29], immersed-interface [16,30], and hybrid Cartesian [15–17] IBMs can be regarded as a subset of the ghost-cell-based approach.

One of the main challenges in IBM may lie with the proper enforcement of boundary conditions on the body interface because it directly influences the accuracy and stability of the numerical solution. Generally, direct linear (bilinear in two dimensions and trilinear in three dimensions) interpolation [22] is utilized for the second-order reconstruction of the ghost-cell values. However, it causes critical stability issues when the immersed boundary is close to the neighboring fluid cell or the required number of interpolation stencils is not satisfied. The inverse distance weighting (IDW) interpolation method is another option that reproduces the values of the mirror-image point in the ghost cell without new local extrema. Mirror-image interpolation [13] provides up to formally second-order accuracy with good stability. However, it produces dispersive solutions when the flow velocity approaches the incompressible limit, or the flow field is smoothly varying where the numerical dissipation becomes small and jump discontinuity [31] across the interface occurs.

More recently, high-order IBMs [14,16,17,25] have been developed. They result in less dispersive and dissipative solutions in the vicinity of the body interface.

The need to address aeroacoustics problems [14], which require high resolution, along with high-order spatial schemes and fluid–structure interaction problems, which require correct information about surface traction forces at the immersed boundary, is increasing. Hence, high-order sharp interface methods are attracting more attention. However, interpolation based on high-order polynomials is often numerically unstable when there are discontinuities in the large interpolating region, especially in compressible flow simulations.

Many researchers have addressed accuracy and stability [17,32], but few studies have considered the robustness and versatility for various types of flow field. Thus, it is necessary to choose between a stable low-order approach that provides inaccurate solutions and an accurate high-order approach that provides unstable solutions, which makes sharp interface IBMs highly problem dependent. Moreover,

2

in real-world problems in aerodynamics, structure, and propulsion systems, the intrinsic phenomenon of shock interaction with obstacles leads to complex flow patterns involving a large variation in flow properties with the generation of large aerodynamic force for a short duration. This phenomenon has attracted significant interest because of the drastic changes in flow at the boundaries of smooth and discontinuous regions. Because of the complex flow physics, the proper implementation of the IBM would be far more effective. Hence, there is a clear need to overcome the limitations of conventional ghost-cell reconstruction techniques.

1.2 Novelty and Scope of Present Study

In this work, a new ghost-cell approach, nonlinear-weighted IBM (NWIBM), is suggested. Inspired by various weighted essentially nonoscillatory (WENO) interpolation methods [33–36] and multidimensional limiting processes [37–39] that handle both smooth and discontinuous flow by using nonlinear stencil coefficients in flux calculation, this study combines high- and low-order reconstruction to achieve stable and accurate solutions in an immersed boundary formulation. The main algorithm is composed of three steps. In the ***first step***, high- and low-order polynomials are calculated with respect to a given geometry, and the corresponding ghost-cell values are obtained using boundary conditions, which is basically the same as the conventional version of ghost-cell IBM. Direct sharp interface method [21,40] is adopted for high-order interpolation, and mirror-image approaches [13,20] are considered for low-order interpolation. From each polynomial, spatial derivatives at the body-intercept point can be evaluated simultaneously. In the ***second step***, previously obtained spatial derivatives for each interpolant at the body-intercept point are utilized to obtain the smoothness indicator. The smoothness indicator is designed multi-dimensionally to evaluate nonlinear weightings. These nonlinear weightings combine the interpolation stencil coefficients of each polynomial, resulting in a new corrected polynomial that has new interpolation stencil coefficients. When the high-order stencils are spread in the smoothly varying region, weightings from the high-order polynomials become dominant, while the weightings from the low-order polynomials become negligible; vice versa in the

discontinuous region. Thus, the stencils are constructed from polynomials with a different order of accuracy, which are combined by nonlinear weightings. In the **_third step_**, flow field nearest to the ghost-cell is reconstructed based on the stencil coefficients obtained from the previous step using Lagrange multiplier method. Through this step, jump-discontinuity across the immersed boundary is minimized. It should be noted that the last step is only performed when smoothly varying condition by nonlinear weighting process is satisfied where the errors due to jump-discontinuity becomes significant.

Because the proposed algorithm maintains a fully high order of accuracy in the smooth region and transits to a low order of accuracy in the discontinuous region, the NWIBM represents an improved alternative to the conventional high-order sharp interface IBMs that can fail, depending on the flow field, because they only consider linear stencil coefficients from one polynomial.

The remainder of this paper is organized as follows. A brief introduction of governing equations and numerical methods is presented in Chapter 2. In Chapter 3, the detailed mathematical derivation of the nonlinear weighting process is discussed, including the conventional low-order and high-order reconstruction methods for IBM. A concept for reducing the jump discontinuity, which can occur in smoothly varying regions, by a flow-extension approach is presented as well. In Chapter 4, the numerical accuracy and stability of the present algorithm are discussed and compared with those of the conventional approaches. In addition, various numerical test problems in compressible flow, used to validate the present method, are described. In Chapter 5, Two engineering application problems were introduced as an application of NWIBM with FSI which have rarely been dealt with previously. The conclusions are summarized in the last chapter.

Chapter 2. Numerical Methods

2.1 Fluid Dynamics

The compressible Navier–Stokes equations that include models for compressible flow convection and diffusion can be written as

$$
\begin{aligned}
&\rho_t + \nabla \cdot \rho \boldsymbol{u} = 0 \\
&(\rho \boldsymbol{u})_t + \nabla \cdot (\rho \boldsymbol{u}\boldsymbol{u}) + \nabla p + \nabla \cdot \boldsymbol{\tau} = 0 \\
&(\rho e)_t + \nabla \cdot \big(\boldsymbol{u}(\rho e + p)\big) + \nabla \cdot (\boldsymbol{u} \cdot \boldsymbol{\tau} + \kappa \nabla T) = 0
\end{aligned}
\qquad , \qquad (1)
$$

where ρ is the density, $\boldsymbol{u}$ is the velocity component, p is the thermodynamic static pressure, κ is the thermal conductivity and e is the specific total energy. The equation of state for an ideal gas is used as a closure, which is given by

$$
p = (\gamma - 1)\left[\rho e - \frac{1}{2}\rho(u^2 + v^2 + w^2) \right], \qquad (2)
$$

where γ is the specific heat ratio and $\boldsymbol{\tau} = \rho \nu\,(2/3(\nabla \cdot \boldsymbol{u})\boldsymbol{I} - \nabla \boldsymbol{u} + \nabla \boldsymbol{u}^{\mathrm{T}})$ is the stress tensor.

If one considers a semi-discretized form of the convective flux derivative at a node i in one direction, it becomes

$$
\frac{\partial \mathcal{F}_i}{\partial x} = \frac{1}{\Delta x}\left[\mathcal{F}_{i+1/2} - \mathcal{F}_{i-1/2} \right], \qquad (3)
$$

where $\mathcal{F}_{i\pm 1/2}$ is the numerical flux at the interface between the nodes or cells. To ensure the upwinding property of the numerical flux, the fifth-order WENO method is used. The procedure to implement WENO [36] is as follows.

First, at each cell interface, right $\boldsymbol{R}_{i\pm1/2}$ and left $\boldsymbol{L}_{i\pm1/2}$ eigenvectors of the flux Jacobian matrix are computed using the Roe-averaged primitive variable $q_{i\pm1/2}$. Then, solution and flux vectors are readily projected into the characteristic space at every cell center:

$$
\hat{\mathcal{Q}}_i = \boldsymbol{L}_{i\pm1/2}\mathcal{Q}_i \quad \text{and} \quad \hat{\mathcal{F}}_i = \boldsymbol{L}_{i\pm1/2}\mathcal{F}_i. \qquad (4)
$$

From local characteristic flux splitting, decomposed positive and negative flux vectors in the characteristic space are expressed as

$$\hat{\mathcal{F}}_i^{\pm} = \frac{1}{2}\left(\hat{\mathcal{Q}}_i \pm |\alpha|\hat{\mathcal{F}}_i\right). \tag{5}$$

According to Lax–Friedrich splitting, α becomes the maximal real eigenvalues of each component of the flux Jacobian matrix. Then, a fifth-order WENO method is implemented to reconstruct the cell interface characteristic flux through the convex combination of three approximations using Eq. (4). To obtain the numerical flux $\mathcal{F}_{i+1/2}$ by the WENO procedure, one can start with the positive characteristic flux at the cell interface.

$$\hat{\mathcal{F}}_{i+1/2}^{+} = w_0 h^0 + w_1 h^1 + w_2 h^2, \tag{6}$$

in which three third-order accurate approximations are

$$h^0 = \frac{1}{3}\hat{\mathcal{F}}_{i-2}^{+} - \frac{7}{6}\hat{\mathcal{F}}_{i-1}^{+} + \frac{11}{6}\hat{\mathcal{F}}_{i}^{+}, \quad h^1 = -\frac{1}{6}\hat{\mathcal{F}}_{i-1}^{+} + \frac{5}{6}\hat{\mathcal{F}}_{i}^{+} + \frac{1}{3}\hat{\mathcal{F}}_{i+1}^{+},$$
$$h^2 = \frac{1}{3}\hat{\mathcal{F}}_{i}^{+} + \frac{5}{6}\hat{\mathcal{F}}_{i+1}^{+} - \frac{1}{6}\hat{\mathcal{F}}_{i+2}^{+} \tag{7}$$

and the nonlinear weights are defined as

$$w_j = \frac{\overline{w}_j}{\overline{w}_0 + \overline{w}_1 + \overline{w}_2}, \quad \overline{w}_j = \frac{d_j}{\left(\beta_j + 10^{-6}\right)^2} \quad (j=0,1,2) \tag{8}$$

where the coefficients d_j are taken as 1, 6, and 3. The smoothness indicators, β_j, that automatically distinguish the discontinuity are defined as

$$\beta_0 = \frac{13}{12}\left(\hat{\mathcal{F}}_{i-2}^{+} - 2\hat{\mathcal{F}}_{i-1}^{+} + \hat{\mathcal{F}}_{i}^{+}\right)^2 + \frac{1}{4}\left(\hat{\mathcal{F}}_{i-2}^{+} - 4\hat{\mathcal{F}}_{i-1}^{+} + 3\hat{\mathcal{F}}_{i}^{+}\right)^2$$
$$\beta_1 = \frac{13}{12}\left(\hat{\mathcal{F}}_{i-1}^{+} - 2\hat{\mathcal{F}}_{i}^{+} + \hat{\mathcal{F}}_{i+1}^{+}\right)^2 + \frac{1}{4}\left(\hat{\mathcal{F}}_{i-1}^{+} - \hat{\mathcal{F}}_{i+1}^{+}\right)^2 \quad . \tag{9}$$
$$\beta_2 = \frac{13}{12}\left(\hat{\mathcal{F}}_{i}^{+} - 2\hat{\mathcal{F}}_{i+1}^{+} + \hat{\mathcal{F}}_{i+2}^{+}\right)^2 + \frac{1}{4}\left(3\hat{\mathcal{F}}_{i}^{+} - 4\hat{\mathcal{F}}_{i+1}^{+} + \hat{\mathcal{F}}_{i+2}^{+}\right)^2$$

In the same way that $\hat{\mathcal{F}}_{i+1/2}^{+}$ is obtained from Eqs. (6)–(9), $\hat{\mathcal{F}}_{i+1/2}^{-}$ can be obtained by an index shift from i to $i-1$ and a sign-change from $\pm$ to $\mp$ for both the subscript and the superscript of each variable. Then, the flux vector in the characteristic space is completed:

$$\hat{\mathcal{F}}_{i+1/2} = \hat{\mathcal{F}}_{i+1/2}^{+} + \hat{\mathcal{F}}_{i+1/2}^{-}. \tag{10}$$

Finally, $\hat{\mathcal{F}}_{i+1/2}$ is projected back to the numerical flux $\mathcal{F}_{i+1/2}$ by multiplying the right eigenvectors:

$$\mathcal{F}_{i+1/2} = \boldsymbol{R}_{i+1/2}\hat{\mathcal{F}}_{i+1/2} . \tag{11}$$

After the spatial discretization is finished, in this study, the time integration of Eq. (1) is performed by a third-order total variation diminishing Runge–Kutta scheme [40] as

$$
\begin{aligned}
U^{(1)} &= U^n + \Delta t L(U^n) \\
U^{(2)} &= \frac{1}{4}\left[3U^n + U^{(1)} + \Delta t L(U^{(1)})\right] \\
U^{n+1} &= \frac{1}{3}\left[U^n + 2U^{(2)} + 2\Delta t L(U^{(2)})\right]
\end{aligned}
\tag{12}
$$

where U is the solution variables. Since the solver developed in this study is explicit, the stability of the overall integration is dominated by Courant-Friedrichs-Lewy (CFL) restriction,

$$\Delta t = CFL / \max[(|u|+c)/\Delta x + (|v|+c)/\Delta y + (|w|+c)/\Delta z] \tag{13}$$

where c is the local speed of sound, and the CFL number is fixed to 0.5 in the whole calculation of the current study.

2.2 Structure Dynamics

For structural analysis, the CR (Co-Rotational) formulation [41–43] was adopted to consider the nonlinear behavior of the flexible structure. The nonlinear time-transient analyses of structures are established by employing the Hilbert Hughes Taylor (HHT) method, which is a variant of the Newmark algorithm [42,44]. Newmark time-integration formulas enforce displacements and velocities such that they are updated according to the following relationships.

$$\mathbf{q}_G^{n+1} = \mathbf{q}_G^n + h\dot{\mathbf{q}}_G^n + h^2\left\{\left(\frac{1}{2} - \beta\right)\ddot{\mathbf{q}}_G^n + \beta\ddot{\mathbf{q}}_G^{n+1}\right\}, \tag{14}$$

$$\dot{\mathbf{q}}_G^{n+1} = \dot{\mathbf{q}}_G^n + h\left\{(1-\gamma)\ddot{\mathbf{q}}_G^n + \gamma\ddot{\mathbf{q}}_G^{n+1}\right\} \tag{15}$$

where $\mathbf{q}_G$, $\dot{\mathbf{q}}_G$, and $\ddot{\mathbf{q}}_G$ denote the structural displacement, velocity, and acceleration vectors, respectively. Moreover, h denotes the size of the time step, and the superscript n indicates an index of the time step. α, β, and γ represent coefficients in the HHT method. The displacements, velocities, and accelerations must be obtained at each time step in an iterative manner, that is, through the Newton–Raphson method.

Algorithm 1 Fluid-structure coupling procedure

1:　**Generate** the immersed boundary information from given geometry

2:　**for** $i := 1$ *to ntime*

　　Time marching loop

3:　　　**Update** HHT α scheme parameter Eqs. (12) and (13)

4:　　　**for** $j := 1$ *to itermax*

　Pseudo time loop

5:　　　　**Call** Fluid (i) : CFD solver based on explicit time marching

6:　　　　**Transfer** NWIBM boundary pressure to structure

7:　　　　**Call** Structure (j)

8:　　　　**Transfer** New geometry (NWIBM)

9:　　　　**Check** convergence

10:　　**end**

11:　　**Update** time-varying quantities

12:　**end**

The nonlinear governing equation of motion can be expressed as

$$\mathbf{f}_e - \mathbf{f}_{K,G} - \mathbf{f}_G = \mathbf{0}, \tag{16}$$

where $\mathbf{f}_e$ denotes the external load vector, and $\mathbf{f}_{K,G}$ and $\mathbf{f}_G$ denote the inertial force vector and the internal force vector with respect to CR kinematics [44]. In the HHT method, the time-transient equilibrium equation is rewritten as

$$(1+\alpha)\mathbf{f}_e^{n+1} - (1+\alpha)\mathbf{f}_G^{n+1} - \mathbf{f}_{K,G}^{n+1} + \alpha\left(\mathbf{f}_G^n - \mathbf{f}_e^n\right) = 0. \tag{17}$$

To obtain the tangent stiffness matrix, the linearization of the inertial load vector is expressed as

8

$$\delta \mathbf{f}_{K,G} = \mathbf{K}_{Dyn,G} \delta \mathbf{q}_G = \left[\frac{1}{\beta h^2} \mathbf{M}_G + \frac{\gamma}{\beta h} \mathbf{C}_{K,G} + \mathbf{K}_{K,G} \right] \delta \mathbf{q}_G, \qquad (18)$$

where, $\mathbf{M}_G$, $\mathbf{C}_{K,G}$, and $\mathbf{K}_{K,G}$ denote mass, gyroscopic, and centrifugal matrices, respectively, referring to the global frame [44].

An implicit coupling approach was used to couple the structural analysis with fluid dynamics analysis. Thus, updated coupled solutions were obtained for the same time-step at the end of the subiteration routine. The numerical coupling between the fluid flow and the structural dynamics models is performed through boundary conditions imposed by NWIBM, which imposes a pressure distribution on the structure boundary. This pressure distribution on the structure boundary is given by NWIBM, and it is transferred to the structural element as an external force. The present FSI framework is described in Algorithm 1.

Chapter 3. Development of Nonlinear Weighted Immersed Boundary Methods

3.1 Ghost-Cell Immersed Boundary Formulation

Before introduction of the nonlinear-weighted IBM, a brief description of two conventional low-order methods and a high-order method for ghost-cell reconstruction are presented.

Let us consider a two-dimensional body within the discretized fluid system with a grid size of Δ where fluid values are defined as ϕ_k within a local support $\boldsymbol{x}_k = (x_k, y_k) \in \Omega_{fluid}$ ($k = 1,2,...,N$) by N data points.

In the case of the low-order method, as illustrated in Fig. 1 (a), the mirror-image value is first defined by executing the piecewise linear reconstruction of fluid cells surrounding the mirror-image point as

$$\phi_{IP} = \sum_{k=1}^{N} \gamma_k \phi_k, \quad \left(\sum_{1}^{N} \gamma_k = 1 \right). \qquad (19)$$

where γ_k is chosen by inverse-distance weighting (IDW) interpolation [13] as

$$\gamma_k = \Delta_k^{-2} \left(\sum_{l=1}^{N} \Delta_l^{-2} \right)^{-1} . \tag{20}$$

Once the interpolation stencil coefficients and mirror-image values are properly calculated, values at the BI point read

$$\phi_{BI} = \frac{1}{2}(\phi_{IP} + \phi_{GC}) + O(\Delta_0^2) \quad \text{and} \quad \frac{\partial \phi_{BI}}{\partial n} = \frac{\phi_{IP} - \phi_{GC}}{\Delta_0} + O(\Delta_0) \tag{21}$$

Here, Δ_0 is the length of the normal line segment extending from the ghost cell to the mirror-image point. From Eq. (20), the above equations become

$$\phi_{BI} = \frac{1}{2}\phi_{GC} + \sum_{k=1}^{N} \frac{\gamma_k}{2} \phi_k \quad \text{and} \quad \frac{\partial \phi_{BI}}{\partial n} = -\frac{1}{\Delta_0}\phi_{GC} + \sum_{k=1}^{N} \frac{\gamma_k}{\Delta_0} \phi_k \tag{22}$$

Applying the Dirichlet and Neumann boundary conditions to Eq. (22) as zero, one can finally achieve the ghost cell values as

$$\phi_{GC} = \mp \sum_{k=1}^{N} \gamma_k \phi_k . \tag{23}$$

The minus–plus sign is expressed in the order of Dirichlet and Neumann boundary conditions, respectively.
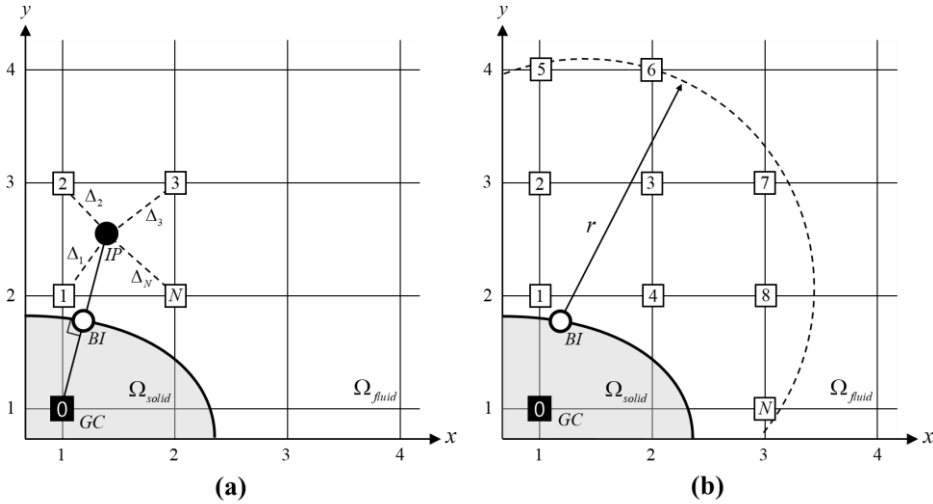
Figure 1. Schematic for (a) low- and (b) high-order immersed boundary reconstruction: ■ ghost-cell, □ fluid cell, ○ body-intercept point, and ● mirror-image point

The IDW interpolation constrains all absolute values of the stencil coefficients to be less than unity and their summation to be unity, which results in the generation of new local extrema that does not satisfy $|\phi_{IP}| \le \phi_k|_{max}$. However, this does not necessarily imply that the boundary can be well described by the interpolated image-point value when its distance from the boundary is $\Delta_0 \gg \Delta$, because the accuracy cannot exceed $O(\Delta_0^2)$. This implies that the order of accuracy can degenerate, especially in the smoothly varying region. This inherent issue can be addressed by a direct ghost-cell interpolation method with an overconstrained system such as high-order interpolation, which is illustrated in Fig. 1 (b).

When it comes to high-order interpolation, the ghost-cell value is determined based on the weighted least squares (WLS) interpolation. If N-stencil data, including fluid cell and ghost point defined as ϕ_k, are approximated from the BI point in terms of an mth-order polynomial form, it reads

$$
\begin{aligned}
\phi_k \approx \bar{\phi}_k &= c_1 + c_2 x'_k + c_3 y'_k \\
&+ c_4 (x'_k)^2 + c_5 x'_k y'_k + c_6 (y'_k)^2 + \cdots + c_M (x'_k)^p (y'_k)^q, \quad p+q=m
\end{aligned}
\tag{24}
$$

where $x'_k = x_k - x_{BI}$, $y'_k = y_k - y_{BI}$ and c_j is the stencil coefficient, the number of which is determined by the order of the polynomial as

$$
M = \frac{(m+1)(m+2)}{2!} \quad \text{and} \quad M = \frac{(m+1)(m+2)(m+3)}{3!}
\tag{25}
$$

for two and three dimensions, respectively. Finally, the unknown coefficient c_j is cast in the WLS problem by the error defined as

$$
\varepsilon = \sum_{k=0}^{N} w_k^2 \left(\bar{\phi}_k - \phi_k \right)^2,
\tag{26}
$$

where w_k refers to the weight function

$$
w_k = 0.5[1+\cos(\pi r_k / r)] \quad \text{for} \quad r_k \le r,
\tag{27}
$$

where r is the radius of the local support, and r_k is the distance from the BI point to the stencil data points. Because the condition for ε to be a minimum is

$$
\frac{\partial \varepsilon}{\partial c_j} = 0,
\tag{28}
$$

the solution of Eq. (21) is given by

$$c = (w\mathcal{V})^+ w\phi, \tag{29}$$

where c and ϕ contain the components of M unknown coefficients and N stencil data, respectively, w is an $N \times N$ diagonal weight matrix, and $\mathcal{V}$ is an $N \times M$ Vandermonde matrix. The pseudo-inverse of the matrix denoted by $(\cdot)^+$ can be computed by singular value decomposition. If one expresses $c = \mathcal{A}\phi$ with a $M \times N$ matrix of $\mathcal{A}(j,k)$ as

$$c_j = \sum_{k=1}^{N} \mathcal{A}(j,k)\phi_k, \quad (j = 1, 2, ..., M). \tag{30}$$

Considering that the Taylor expansion of ϕ_k in terms of x_{BI} is

$$\phi_k \approx \bar{\phi}_k = \phi_{BI} + \frac{\partial \phi_{BI}}{\partial x} x_k' + \frac{\partial \phi_{BI}}{\partial y} y_k' + \frac{1}{2}\frac{\partial^2 \phi_{BI}}{\partial x^2}(x_k')^2 + \frac{\partial^2 \phi_{BI}}{\partial x \partial y} x_k' y_k' + \frac{1}{2}\frac{\partial^2 \phi_{BI}}{\partial y^2}(y_k')^2 + \cdots, \tag{31}$$

c_j in Eq. (30) can be mapped to the values and derivatives of ϕ_{BI}.

Thus, Eq. (30) for each j becomes

$$\phi_{BI} = \sum_{k=1}^{N} \mathcal{A}(1,k)\phi_k, \quad \frac{\partial \phi_{BI}}{\partial x} = \sum_{k=1}^{N} \mathcal{A}(2,k)\phi_k, \quad \frac{\partial \phi_{BI}}{\partial y} = \sum_{k=1}^{N} \mathcal{A}(3,k)\phi_k,$$

$$\frac{\partial^2 \phi_{BI}}{\partial x^2} = 2\sum_{k=1}^{N} \mathcal{A}(4,k)\phi_k, \quad \frac{\partial^2 \phi_{BI}}{\partial xy} = \sum_{k=1}^{N} \mathcal{A}(5,k)\phi_k, \quad \cdots \tag{32}$$

Because the interpolation stencil coefficients with respect to x_{BI} are given, the Dirichlet and Neumann boundary conditions can be expressed in terms of $\phi_{GC} = \phi_1$, where

$$\phi_{GC} = \frac{\phi_{BI} - \sum_{k=1}^{N} \mathcal{A}(1,k)\phi_k}{\mathcal{A}(1,1)} + O(\Delta^{m+1}) \tag{33}$$

for the Dirichlet boundary condition and

$$\phi_{GC} = \frac{\frac{\partial \phi_{BI}}{\partial n} - n_x \sum_{k=2}^{N} \mathcal{A}(2,k)\phi_k - n_y \sum_{k=2}^{N} \mathcal{A}(3,k)\phi_k}{n_x \mathcal{A}(2,1) + n_y \mathcal{A}(3,1)} + O(\Delta^{m+1}) \tag{34}$$

for the Neumann boundary condition. As a result, an $O(\Delta^{m+1})$ order of accuracy is ensured for the mth-order polynomial least-squares interpolation. Thus, ghost-cell

12

values with high-order accuracy can be achieved using WLS compared with the low-order approach.

The local support area should contain sufficient data points such that $N \gg M$ to preserve stability and avoid the ill-conditioned least-squares problem. However, preserving a sufficient number of data points and formulating a well-conditioned matrix does not necessarily satisfy the numerical stability requirements. When the data values contain severe discontinuities, the reconstructed ghost-cell value can be adversely and unpredictably affected because the order constraints by Taylor series expansion in Eq. (31) do not hold true anymore. There is a need to use the high-order interpolation by WLS conditionally to address the numerical instability issue.

3.2 Nonlinear Weighting Process

The use of high- and low-order polynomials to reconstruct the ghost-cell values that satisfy the boundary conditions has been addressed in the previous chapter. In a numerical analysis with IBM for compressible flow, a low-order mirror-image immersed boundary formulation by IDW is commonly used, which helps avoid the possible local extrema that hampers stability. However, there are accuracy issues when the flow field contains smoothly varying regions with a relatively low gradient, where low-order interpolation can fail. Hence, an algorithm is proposed that implicitly applies high-order interpolation to low-order interpolation by introducing nonlinear weighting coefficients. The proposed algorithm can be classified into three steps. Following is the procedures of nonlinear weighting process containing the first and the second steps, and the third step will be discussed in the chapter 3.3, separately.

Remark 1. For the first step, the high- and low-order polynomials for IBMs are first constructed. It was shown in Eqs. (21), (22), and (32) that the values (or derivatives) in terms of the boundary-intercept point are in the form

$$f_{BI}^{j} = \sigma_1^{j}\phi_{GC} + \sum_{k=2}^{N_j} \sigma_k^{j}\phi_k + O(\Delta^{\delta_j}), \tag{35}$$

where σ_k^{j} is the polynomial coefficient, j is a type of interpolation method, and δ_j refers to the order of accuracy. If an appropriate proper boundary condition is

applied to f_{BI}^j, the ghost-cell values can be obtained. Subsequently, the derivatives at the BI point can be calculated, and this is used in the following correction step.

Remark 2. As the second step, suppose there is another polynomial corrected by the sum of two different sets of polynomials from Eq. (35) as

$$f_{BI}^C = \omega^H f_{BI}^H + \omega^L f_{BI}^L, \tag{36}$$

where ω is the weighting coefficients for combining two different approximations to the final corrected one, and the superscripts H, L, and C denote high-order, low-order, and corrected polynomials, respectively.

If the corrected new polynomial can be expressed in the same form as Eq. (35), Eq. (36) is rearranged as

$$\begin{aligned}
&(\sigma_0^C - \omega^H \sigma_0^H - \omega^L \sigma_0^L)\phi_{GC} + (\sigma_1^C - \omega^H \sigma_1^H - \omega^L \sigma_1^L)\phi_1 + (\sigma_2^C - \omega^H \sigma_2^H - \omega^L \sigma_2^L)\phi_2 + \cdots \\
&+(\sigma_{N_H+1}^C - \omega^H \sigma_{N_H+1}^H)\phi_{N_H+1} + \cdots + (\sigma_{N_H-1}^C - \omega_1 \sigma_{N_H-1}^H)\phi_{N_H-1} + (\sigma_{N_H}^C - \omega^H \sigma_{N_H}^H)\phi_{N_H} = 0
\end{aligned} \tag{37}$$

where it has been assumed that the number of stencils of the high-order polynomial always outnumbers that of the low-order polynomial ($N^H > N^L$), and the stencils of the low-order polynomial are a subset of the high-order polynomial ($N^C = N^H$).

To satisfy the interpolation property,

$$\sum_{k=1}^{N_H} \sigma_k^{C,H,L} = \begin{cases} 0 & for \quad f_{BI}^{C,H,L} = \phi_{BI} \\ 1 & for \quad f_{BI}^{C,H,L} = \partial_{x,y,z}\phi_{BI} \end{cases} \tag{38}$$

should hold true. Thus, the stencil coefficients of the corrected polynomial σ^C can be obtained as

$$\sigma_k^C = \begin{cases} \omega^H \sigma_k^H + \omega^L \sigma_k^L & for \quad k \le N^L \\ \omega^H \sigma_k^1 & for \quad N^L < k \le N^H \end{cases}. \tag{39}$$

The corrected polynomial at the BI point can be written as

$$f_{BI}^C = \sigma_1^C \phi_{GC}^C + \sum_{k=2}^{N_H} \sigma_k^C \phi_k + O(\Delta^{\delta_C}). \tag{40}$$

Thus, the coefficient is composed of the values at the ghost cell and flow fields in Eq. (28), and the order of accuracy of the corrected interpolant reads

$$O(\Delta^{\delta_C}) = \omega^H O(\Delta^{\delta_H}) + \omega^L O(\Delta^{\delta_L}). \tag{41}$$

Remark 3. The corrected polynomial ϕ_{BI}^C, which is the convex combination of ϕ_{BI}^H and ϕ_{BI}^L, does not guarantee a high-order approximation unless the number of polynomials is equal to the number of stencils. Hence, a modified nonlinear weighting inspired by a previous study [33] is suggested to eliminate the effects of the low-order approximation when the smoothness within the polynomial stencils of the high-order approximation is ensured. The nonlinear weighting is defined as

$$\omega^j = \begin{cases} \dfrac{\alpha^j}{\gamma^j} & for \ j = H \\ 1 - \omega^H & for \ j = L \end{cases} \tag{42}$$

where α^j and γ^j are the sub-nonlinear and linear weighting coefficients, respectively.

It is assumed that α^j can be varied from 0 to γ^j with respect to the relative smoothness of the interpolation polynomials. If the interpolant ϕ_{BI}^H is reconstructed within the smoothly varying flow region, a high order of accuracy can be ensured by making the contribution of ω^H dominant over those of the other nonlinear weightings. The sufficient condition for high-order reconstruction is $\alpha^H = \gamma^H$ because the stencils of the lower-order polynomials are always the subset of the stencils of the high-order polynomials. However, if ϕ_{BI}^H is not sufficient to ensure smoothness and cover discontinuities, ω_1 becomes negligible, while the lower-order polynomials become active. The necessary condition for low-order reconstruction is $\alpha^H \ll \gamma^H$. The above statements indicate that ω^j should transit from the high order to low order or vice versa when α^j is deliberately designed. Although there are other possible approaches to design α^j, in this study, α^j was designed using a multidimensional smoothness indicator [45,46].

The sub-nonlinear weighting coefficient α^j should be designed such that maximum accuracy is achieved for the given data, while information coming from nonsmooth data should be switched off to prevent the onset of spurious oscillations in nonsmooth regions. Similar to the WENO-type schemes, the sub-nonlinear weighting coefficient is

$$\alpha^j = \frac{\bar{\alpha}^j}{\bar{\alpha}^H + \bar{\alpha}^L}, \quad \bar{\alpha}^j = \gamma^j \left[1 + \frac{(\beta^H - \beta^L)^2}{(\varepsilon + \beta^j)^2} \right], \tag{43}$$

where β^j is a smoothness indicator for a polynomial j, and ε is a small positive number to avoid the denominator from being zero.
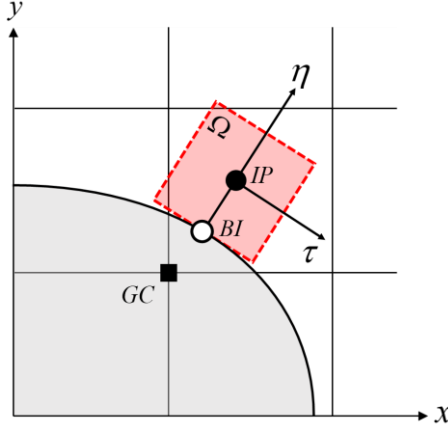
Figure 2. Illustration of the virtual cell zone Ω in normal (η) and tangential (τ) coordinates with respect to the BI point.

Remark 4. To find a suitable value of the smoothness indicator for each polynomial, consider a Lipschitz-continuous virtual cell zone Ω centered at the mirror-image point with a size Δ, as shown in Fig. 2. For each Ω, a local set of coordinates is given by $(\tau, \eta) \in [-\Delta/2, \Delta/2] \times [-\Delta/2, \Delta/2]$, where $\Delta/2$ is defined as the distance between BI and IP. The Legendre polynomial basis, suitably modified for the present domain, is given by

$$\mathcal{L}_0 = 1, \ \mathcal{L}_1(a) = a, \ \mathcal{L}_2(a) = a^2 - \frac{1}{12}, \ \mathcal{L}_3(a) = a^3 - \frac{3}{20}a, \tag{44}$$

which has a diagonal mass matrix and an orthogonal property. One can arbitrarily express the cell-averaged value with respect to $\bar{\phi}_{IP}$ as

$$
\begin{aligned}
\bar{\phi}_{IP} = {}& \phi_{BI}\mathcal{L}_0 + \phi_\tau \mathcal{L}_1(\tau) + \phi_\eta \mathcal{L}_1(\eta) \ \leftarrow second\ order \\
& + \phi_{\tau\tau}\mathcal{L}_2(\tau) + \phi_{\eta\eta}\mathcal{L}_2(\eta) + \phi_{\tau\eta}\mathcal{L}_1(\tau)\mathcal{L}_1(\eta) \ \lrcorner\ third\ order \\
& + \phi_{\tau\tau\tau}\mathcal{L}_3(\tau) + \phi_{\eta\eta\eta}\mathcal{L}_3(\eta) + \phi_{\tau\tau\eta}\mathcal{L}_2(\tau)P_1(\eta) + \phi_{\eta\eta\tau}\mathcal{L}_2(\eta)\mathcal{L}_1(\tau) \ \lrcorner\ fourth\ order
\end{aligned}
\tag{45}
$$

where subscripts τ and η refer to the partial derivatives of ϕ_{BI}. The arrows denote the subset to achieve the order of accuracy of a polynomial.

One can now calculate the smoothness indicator based on the polynomial in Eq. (45). The smoothness indicator that measures the smoothness of a polynomial $\bar{\phi}_{IP}$ is defined as

$$\beta^j = \sum_{|\kappa|=1}^{3} \int_{\Omega} \Delta^{2(|\kappa|-1)} (D_\kappa \bar{\phi}_{IP}^j)^2 \, d\Omega \,, \tag{46}$$

where D is a multidimensional differential operator and $\kappa = (\kappa_x, \kappa_y, \kappa_z)$ is a multi-index denoting derivatives.

For the mirror-image method case, $\bar{\phi}_{IP}$ is given by a piecewise constant, which results in $\beta^L = 0$. However, for the high-order interpolation method, Eq. (46) must be directly computed as

$$
\begin{aligned}
\beta^j = {}& h^2(\phi_\tau^2 + \phi_\eta^2) \quad \leftarrow \textit{second order} \\
&+ \frac{13}{3} h^4 \left(\phi_{\tau\tau}^2 + \phi_{\eta\eta}^2 \right) + \frac{7}{6} h^4 \phi_{\tau\eta}^2 \quad \lrcorner \textit{third order} \\
&+ \frac{1953}{50} h^6 \left(\phi_{\tau\tau\tau}^2 + \phi_{\eta\eta\eta}^2 \right) + \frac{1}{5} h^6 \left(\phi_\tau \phi_{\eta\eta\eta} + \phi_\eta \phi_{\tau\tau\tau} \right) + \frac{47}{10} h^6 \left(\phi_{\tau\eta\eta}^2 + \phi_{\tau\tau\eta}^2 \right) \quad \lrcorner \textit{fourth order}
\end{aligned}
\tag{47}
$$

for two dimensions.

The three-dimensional smoothness indicator can be obtained straightforwardly.

$$
\begin{aligned}
\beta^j = {}& h^2(\phi_\tau^2 + \phi_\eta^2 + \phi_\varsigma^2) \quad \leftarrow \textit{second order} \\
&+ \frac{13}{3} h^4 \left(\phi_{\tau\tau}^2 + \phi_{\eta\eta}^2 + \phi_{\varsigma\varsigma}^2 \right) + \frac{7}{6} h^4 \left(\phi_{\tau\eta}^2 + \phi_{\eta\varsigma}^2 + \phi_{\tau\varsigma}^2 \right) \quad \lrcorner \textit{third order} \\
&+ \frac{1953}{50} h^6 \left(\phi_{\tau\tau\tau}^2 + \phi_{\eta\eta\eta}^2 + \phi_{\varsigma\varsigma\varsigma}^2 \right) + \frac{1}{5} h^6 \left(\phi_\tau \phi_{\tau\tau\tau} + \phi_\eta \phi_{\eta\eta\eta} + \phi_\varsigma \phi_{\varsigma\varsigma\varsigma} \right) \\
&+ \frac{47}{10} h^6 \left(\phi_{\tau\eta\eta}^2 + \phi_{\tau\tau\eta}^2 + \phi_{\tau\varsigma\varsigma}^2 + \phi_{\tau\tau\varsigma}^2 + \phi_{\eta\varsigma\varsigma}^2 + \phi_{\eta\eta\varsigma}^2 \right) + \frac{144}{157} h^6 \phi_{\tau\eta\varsigma}^2 \quad \lrcorner \textit{fourth order}
\end{aligned}
\tag{48}
$$

Finding partial derivatives of ϕ_{BI}^H requires a ghost-cell value that is not known before achieving β^L. Such implicitly coupled characteristics are handled using the predicted ghost-cell value, which is given by ϕ_{GC}^H in Eqs. (40) and (41). Because $\beta^L = 0$ when using the mirror-image method in low-order interpolation, this predicted ghost-cell value does not affect the weightings of $\bar{\alpha}^L$.

After all nonlinear weightings from Eq. (42) and the stencil coefficients from Eq. (39) are found, the values and derivatives at the BI point can be readily given as Eq. (40). By applying a boundary condition that is zero for the Dirichlet and Neumann boundary conditions, the corrected ghost-cell value that is ultimately needed is formulated as

$$\phi_{GC}^{C} = -1 / \sigma_1^{C} \sum_{k=2}^{N_H} \sigma_k^{C} \phi_k \, . \tag{49}$$

Depending on σ^C, which is affected by nonlinear weightings, the above equation results in an optimal ghost-cell value based on the smooth transition between high-order and low-order reconstruction, and it can be reduced to exactly one of them.

Algorithm 2. Nonlinear-weighted IBM procedure

1: **Generate** the immersed boundary information from a given geometry

for j = 1 to number of *BI do*

2: **Construct** polynomial coefficients: σ^H and σ^L for each *BI* values and derivatives

3: **Calculate** the predicted values: ϕ_{GC}^{H}

4: **Estimate** smoothness indicator: β^H ▶ prediction step finished

5: **Obtain** nonlinear weighting coefficients: ω^H and ω^H

7: **Construct** corrected polynomial coefficients: σ^C for each *BI* value and derivative

8: **Calculate** the corrected values: ϕ_{GC}^{C} ▶ correction step finished

end for

9: **Repeat** 2–8 for all physical properties

3.3 Jump-Discontinuity Minimization Process

Let us define a one-dimensional grid distribution $\mathbb{S} = \{x_i \mid -2 \leq i \leq 4\}$ where the immersed boundary is located in between x_0 and x_1. In Fig. 3, a schematic of solution $\psi_j(x_j)$ is expressed as an example in both analytic space by solid lines and discretized space by dashed lines with a particular boundary condition $\psi^{(n)} = b$ at $x = x_\xi$. The superscript stands for the $n^{\text{th}} -$ derivative. Even if the ghost-cell values based on nonlinear weighting process are properly calculated, there is a high chance that the jump-discontinuity occurs in between the boundary because the ghost-cell values are only designed to match the boundary conditions. Unless an artificial damping or upwind characteristics are applied in a non-smooth solution, it is known that the standard central spatial scheme fails, resulting in oscillations because they are basically constituted by the Taylor expansions. Wiegmann [31] and Linnick [16] mathematically managed this jump-discontinuity problem, using corrected finite differences by manipulating the Taylor series. If the generic solution variable ψ is assumed to be analytic $\forall x \in [x_0, x_\xi]$ and $\forall x \in [x_\xi, x_1]$, then the corrected Taylor series of an infinitely differentiable function with respect to x_0 can be expressed as a power series

$$\psi(x) = \sum_{n=0}^{m} \frac{\Delta^n}{n!} \psi^{(n)}(x_0) + \mathcal{O}(\Delta^{n+1}) + \mathcal{J}, \quad (\Delta = x - x_0) \tag{50}$$

where the jump-correction term $\mathcal{J}$ is added so that the jump across the interface at $x = \xi$ could be considered. At $x = x_1$,

$$\left| \psi(x_1) - \sum_{n=0}^{m} \frac{\Delta^n}{n!} \psi^{(n)}(x_0) - \sum_{n=0}^{m} \frac{(\Delta^+)^n}{n!} \left[\psi^{(n)} \right]_\xi \right| \leq \frac{\mathcal{K}}{(m+1)!} \Delta^{m+1}, \quad (\Delta^+ = x_1 - x_\xi) \tag{51}$$
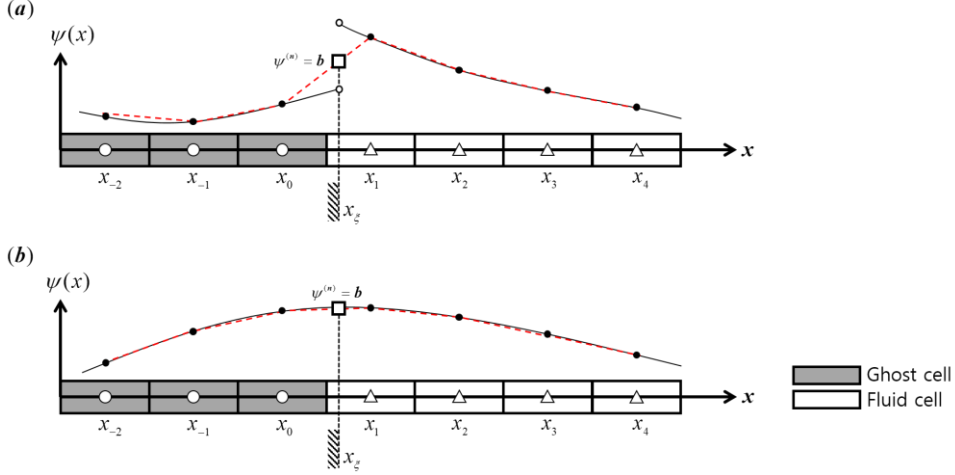
where

$$\mathcal{K} = \max \left(\max_{x \in [x_0, x_\xi]} \left| (\psi^-)^{(m+1)}(x) \right|, \max_{x \in [x_\xi, x_1]} \left| (\psi^+)^{(m+1)}(x) \right| \right) \tag{52}$$

holds true from lemma.

Superscript $\pm$ stands for the direction of limit values. Thus, the jump-correction term is readily found to be

$$\mathcal{J} = \sum_{n=0}^{m} \frac{(\Delta^+)^n}{n!} \left[\psi^{(n)} \right]_\xi , \quad \left(\Delta^+ = x_1 - x_\xi \right)$$ (53)

where the limit value is $\left[\psi^{(n)} \right]_\xi = \lim\limits_{x \to x_\xi^+} \psi^{(n)}(x) - \lim\limits_{x \to x_\xi^-} \psi^{(n)}(x)$.

Figure 3. A schematic diagram of solution $\psi(x)$ with the boundary condition at $x = x_\xi$. (a) A solution with discontinuity; (b) a solution with reduced discontinuity.

This corrected Taylor series is utilized to reformulate the numerical flux derivatives. To calculate the jump-correction term defined in Eq. (53), the limit values should be found in an appropriate manner. In incompressible flow, limit values approaching from the fluid domain is obtained by proper interpolations, and the limit values inside the solid domain were not considered because the no-slip boundary condition makes all the velocity components zero at the solid boundary. However, it seems quite tricky to directly find the jump-correction for compressible flow of our interest where the limit values approaching from solid domain should be defined because of Neumann boundary condition, which also makes high-order extension problematic near the boundary. This jump-discontinuity seldom induces spurious oscillations in the immersed boundary method, especially when an undefined cell (fresh-cell) emerges. When it comes to the fluid–structure interaction problem where transient deformation occurs, it is more important to evade such spurious waves that degrade the accuracy of the solution.

20

To overcome this problem, the flow field reconstruction combined with a nonlinear weighting process is introduced in this study.

If jump-discontinuity with $n = 0$ is written as

$$\mathcal{J} = \phi_{BI} - \phi_{BI}^+ , \tag{54}$$

where ϕ_{BI}^+ is the limit value approaching from the fluid zone, the reconstructed fluid cell nearest to the ghost cell becomes

$$\phi_F = a_1 \phi_{BI}^+ + \sum_{k=2}^{N_F} a_k \phi_k^F , \tag{55}$$

where a_k is the interpolation coefficient to reconstruct the flow field value, ϕ_F using near fluid cells, ϕ_k^F and BI value at the fluid side, ϕ_{BI}^+. Since this reconstruction is performed in the analytic fluid zone, it can be assumed that there is no jump discontinuity.

To minimize $\mathcal{J}$ upon including the boundary condition of Eq. (33) as an additional constraint, the Lagrangian multiplier reads

$$\mathcal{L} = \left(\phi_{BI} - \phi_{BI}^+ \right)^2 + \lambda f_{BI}^C , \tag{56}$$

where ϕ_{BI} is already obtained by the nonlinear weighting process in Eq. (33). Expanding Eq. (56) yields three unknowns ϕ_F, ϕ_G and λ. The conditions for minimization are

$$\frac{\partial \mathcal{L}}{\partial \phi_F} = 0, \quad \frac{\partial \mathcal{L}}{\partial \phi_G} = 0, \quad \frac{\partial \mathcal{L}}{\partial \lambda} = 0. \tag{57}$$

After simple mathematical calculation, the fluid and ghost cell values can be readily found. The above field-reconstruction procedure successfully couples the ghost and fluid-cell values in addition to the nonlinear weighting process. It is effective in damping out the spurious oscillation induced by jump discontinuity. Moreover, the additional computational cost is negligible because field reconstruction is performed only when fresh cells occur.
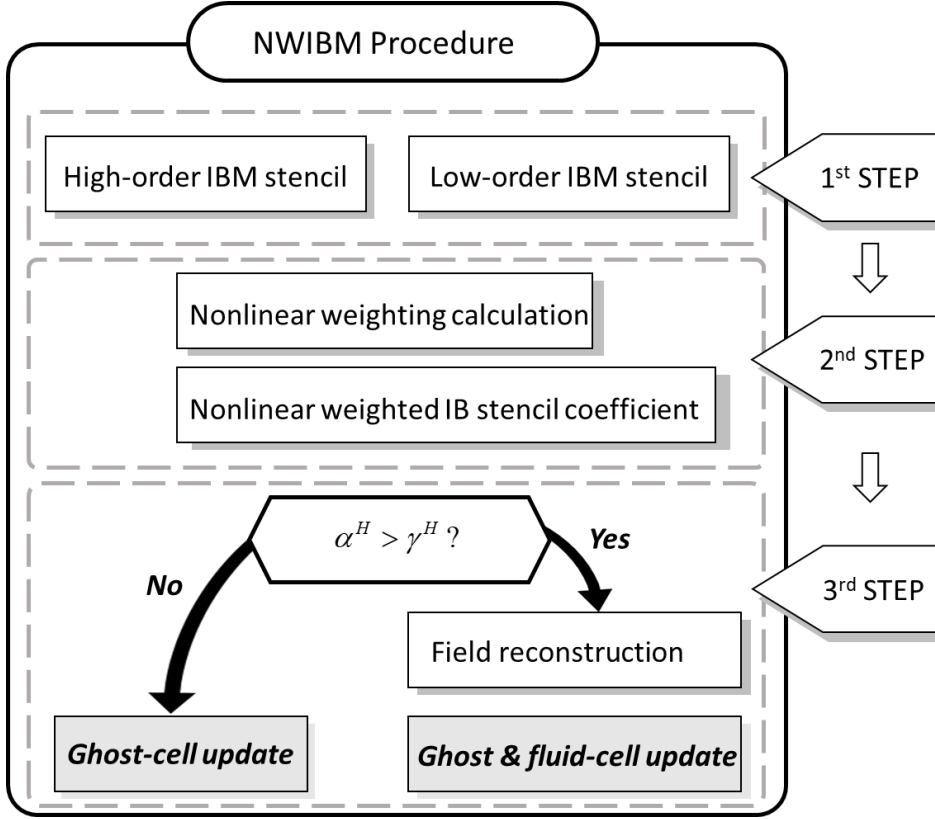
Figure 4. Schematic of three step procedure for NWIBM

3.4 Stability Analysis

The linear stability analysis was carried out based on the well-known Lax–Richtmyer equivalence theorem. Because it is known that the stability of a complex system can be sufficiently modeled by a scalar equation [47], the semidiscretized form of the one-dimensional linear convection equation was used to investigate the Lax stability of Euler equations. If $\mathcal{M} \in \mathbb{R}^{N \times N}$ is the discrete representation of analytic domain $\mathbb{R}$ by a bounded linear operator $\mathcal{L}$ for a spatial discretization, the linear operator yields

$$\frac{\partial \phi}{\partial t} = \mathcal{L}\phi \ \rightarrow \ \frac{\partial \phi_i}{\partial t} = \mathcal{M}_{ij}\phi_j \quad (i, j = 1, 2, \cdots, N). \tag{58}$$

Its exact solution is written as

$$\phi(x,t) = e^{\mathcal{M}t}\phi(x). \tag{59}$$

To investigate the stability, a transformation to the spectral domain can be applied by diagonalization of matrix $\mathcal{M}$ with the eigenvalue matrix Λ and invertible eigenvector matrix $\mathcal{P}$ as $\mathcal{M} = \mathcal{P}\Lambda\mathcal{P}^{-1}$.
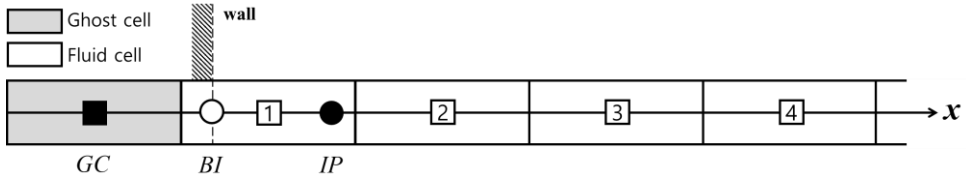
By defining $\varphi \equiv \mathcal{P}^{-1}\phi$, Eq. (59) is readily transformed to

$$\frac{\partial \varphi_i}{\partial t} = \Lambda_{ij}\varphi_j. \tag{60}$$

Thus, the transformed exact solution can be written as

$$\varphi(x,t) = e^{\Lambda t}\varphi(x). \tag{61}$$

It can be found that the stability is dependent on the properties of the complex eigenvalues of matrix $\mathcal{M}$ by obtaining the temporal divergence with the positive real part of the eigenvalues.

Figure 5. One-dimensional grid system with immersed boundary

When a generic solution variable ϕ_i is given in the analytic fluid zone at the ith cell as in Fig. 5, a semidiscretized form of the explicit finite-difference scheme is written as

$$\frac{\partial \phi_i}{\partial t} = \frac{c}{\Delta x} \sum_{j=-k}^{k} a_i \phi_{i+j} \tag{62}$$

where c and Δx are the advection speed and the grid-spacing with $c/\Delta x = -1$. Moreover, a_i represents the linear coefficients for flux derivatives. Because the focus is on the relative stability of the proposed immersed boundary approach compared with conventional ones, simple standard finite-difference stencils of a_i are used for the flux derivative, such as $a_{-1} = -0.5, a_0 = 0, a_1 = 0.5$.

The immersed boundary is located on the left border, and it is not updated with time. It was defined that the ghost-cell value could be expressed by a linear combination of fluid cells as

$$\phi_{GC} = \sum_{j=1}^{n} b_j \phi_j \tag{63}$$

where b_j is the interpolation coefficients with respect to the IBMs. In this study, the Dirichlet wall boundary condition was utilized with respect to different values of nonlinear weightings, α^H.

Eq. (62) is changed into the form of the system matrix

$$\frac{\partial \phi_i}{\partial t} = \mathcal{M}_{ij}\phi_j = \frac{c}{\Delta x} \begin{bmatrix} a_0 + a_{-1}b_1 & a_1 + a_{-1}b_2 & \cdots & b_n & 0 \\ a_{-1} & a_0 & a_1 & & \\ & a_{-1} & a_0 & a_1 & \\ & & \ddots & \ddots & \\ 0 & & & a_{-1} & a_0 + a_1 \end{bmatrix} \begin{bmatrix} \phi_1 \\ \vdots \\ \phi_j \\ \vdots \\ \phi_N \end{bmatrix} \tag{64}$$

where the number of cells $N = 50$, and the artificial boundary condition [32] is introduced at the right border so that the instability of left border is not inhibited. Complex eigenvalues of matrix $\mathcal{M}$ were computed at three immersed boundary positions moving away from the first ghost cell with a distance $\xi = \{0.1\Delta x$, $0.5\Delta x, 0.9\Delta x\}$. In Figs. 6(a)–(c), the eigenvalue distributions with a central difference scheme are plotted in the complex domain. Here, all the complex eigenvalues are shown to be located within the left half-plane.

When $\alpha^H = 0$

It can be found that least stability has been shown when only high-order IBM is used ($\alpha^H = 1.0$). The stability region gets increased as low-order IBM is combined with decreased α^H. When the location of the boundary intersection point is close to the ghost cell ($\xi = 0.1\Delta x$), degeneracy of stability for low-order IBM ($\alpha^H = 0.0$) is shown compared to the other cases. It can be attributed to the fact that the low-order IBM, which is equivalent to mirror-image method, cannot but use fewer stencil points when $\xi < 0.5\Delta x$. It should be noted that the combined interpolation with nonlinear weighting shows stable results.
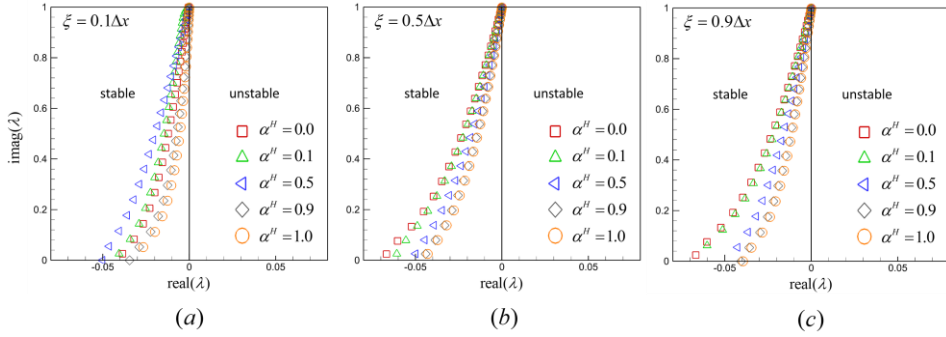
Figure 6. Eigenvalues of matrix $\mathcal{M}$ with respect to nonlinear weightings at three different immersed boundary positions.

Additionally, the stability results when field reconstruction is used. In this case, linear stability is also calculated based on the 4th order standard finite-difference scheme since field reconstruction is used for smoothly varying flow region. In Fig. 7, comparisons between filed reconstructed and no reconstructed high-order IBM are plotted. Even if all the complex eigenvalues are shown to be located within the left half-plane, it can be found that flow reconstruction brings about enhanced stability.
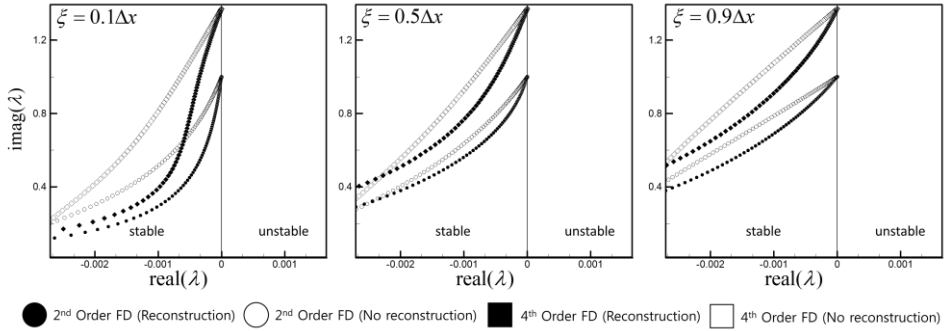
Figure 7. Eigenvalues of matrix $\mathcal{M}$ for no-weighted interpolation for flow reconstruction and no reconstruction are used at three different immersed boundary positions.

3.5 Accuracy Study

The method of manufactured solutions (MMS) [17] is utilized to verify the code by constructing analytical solutions to the differential equations that form the basis of a simulation code. This method differs from a conventional verification approach, such as the method of exact solutions, in that the analytical solution of the governing equations is given *a priori*, and code mistakes or bugs can be readily identified.

In the MMS, a manufactured analytic solution is built that considers the boundary conditions of the immersed boundary. The selected, manufactured solution does not necessarily need to be physically relevant. It can be chosen as long as the derivatives up to the order required by the governing equations are continuous. Then, the differential operator for the governing equations is applied to this chosen analytical solution, and the analytical source terms are added to the right-hand side of the governing equations to balance the system. These source terms are implemented within the code, and the modified governing equations (including the source terms) are then discretized, solved numerically, and compared with the exact solution. A steady-state divergence-free flow problem [17] was considered to evaluate the formal order of accuracy of the spatial scheme incorporated with the imposed IBM. The accuracy study is performed within the computational domain of $\Omega = [-1,1] \times [-1,1]$ with a full period for the velocity and pressure fields. The manufactured solutions for the divergence free velocity fields that satisfy the continuity equation in the incompressible limit are chosen to consider the Dirichlet condition at the immersed boundary as

$$u = \cos(2\pi x)\sin(2\pi y), \quad v = -\sin(2\pi x)\cos(2\pi y) \tag{65}$$

and the pressure field is set to consider the Neumann condition as

$$p = 0.5 + r^2 - 2rr_0 \tag{66}$$

where r is the distance from the center to grid point (x, y), and r_0 is the radius of the circular cylinder located at $(0,0)$, which is set to 0.5. The density field is set to constant unity. The boundary conditions at the immersed boundary, Γ can be imposed as

$$u = u\big|_\Gamma, \quad v = v\big|_\Gamma, \quad \frac{dp}{dn}\bigg|_\Gamma = 0 \tag{67}$$

The analytical source terms, which are mathematically calculated by the manufactured solution, are given in Fig. 8 (a).
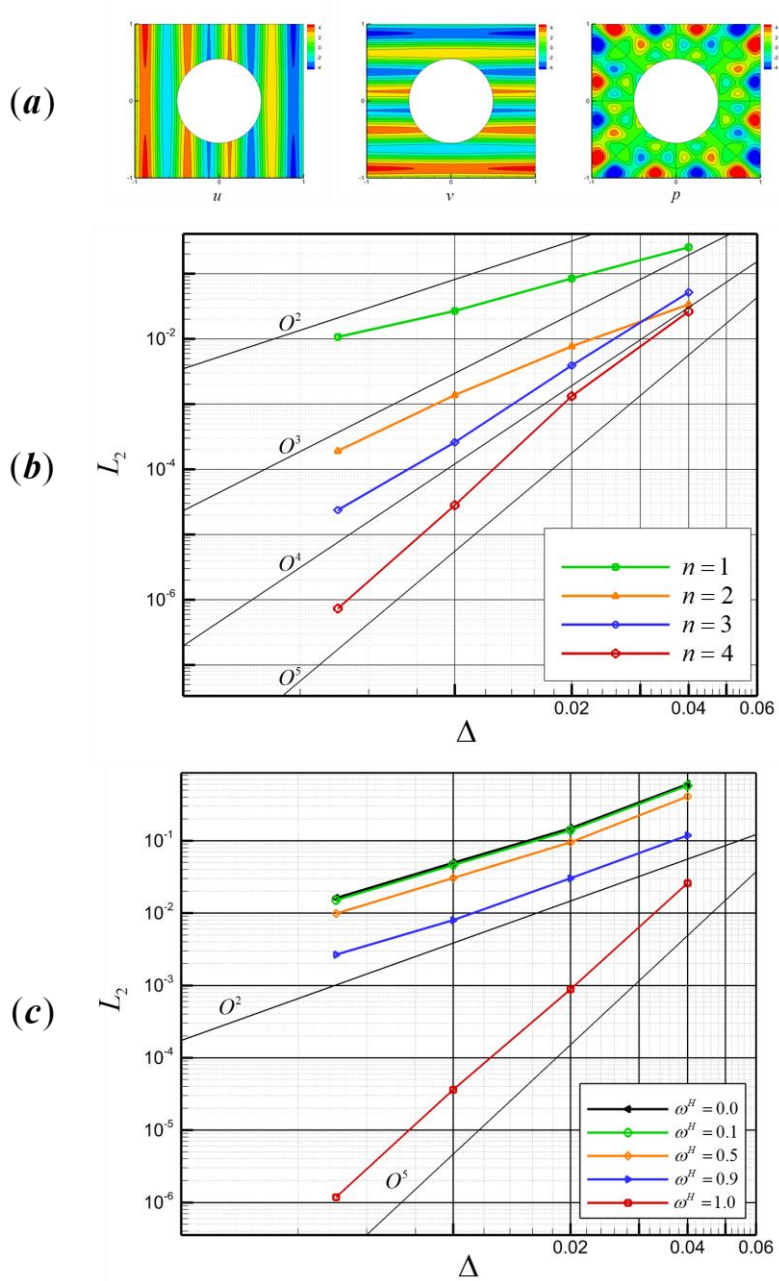
Figure 8. (a) Manufactured solutions, and its global error convergence when (b) $\omega^H = 1.0$ and (c) $\omega^H \neq 1.0$.

Firstly, the ghost-cell is calculated when only high-order interpolation is used ($\omega^H = 1.0$) so that the field reconstruction algorithm is activated. In Fig. 8 (b), the global convergence results from high-order interpolation with 1 to 4-degree polynomial interpolations are shown. The slope behavior of L_2 – norm follows the order of polynomial and the order of accuracy has been shown to degenerate as the interpolation order decreases. It is found that the nth -degree polynomial interpolation by WLS preserves the global order of accuracy within the 5th-order WENO scheme.

Secondly, the ghost-cell is calculated using both high-order and low-order interpolation in order to verify the convergence by nonlinear weighting process. In this case, field reconstruction is not included since it has been shown in Fig. 8 (b). In Fig. 8 (c), the global convergence results using 4-degree polynomial for high-order interpolation, and IDW for low order interpolation. The constant nonlinear weighting values are enforced to compare the convergence as the high-order and low-order IBMs are combined. As ω^H decreases by taking the low-order polynomial into account in the corrected polynomial, the convergence is switched to second order, and the error increases. In addition to showing good stability performance, as discussed in the previous subchapter, it has been verified that WLS and IDW can be used as a high-order and low-order polynomial in the NWIBM, respectively.

Chapter 4. Numerical Results

4.1 Subsonic flow problems

4.1.1 Low-Mach-number study

To investigate the NWIBM, a low-Mach-number flow study with a uniform flow is performed. The use of low Mach number studies to examine the performance of the compressible flow solver should not be dismissed [48], because in the proposed method, along with the nonlinear weighting process, the focus is on the reduction of the jump-discontinuity in the smooth flow region. Therefore, the Low-Mach-number study seems to be favorable for showing the performance of the suggested NWIBM

via flow reconstruction concept, compared to conventional high-order IBM without field reconstruction. As a demonstration of the present simulation, a two-dimensional circular cylinder of diameter $D=1$ is analyzed within the mean flow of Mach number $M=0.05$. Two set of 60×60 domains are considered with a uniform grid size $\Delta=D/80$ and $\Delta=D/160$ [49]. The Euler equations are used with slip-boundary conditions to consider the convectional effects only. The enhanced performance of the current method has been evaluated by the jump-correction term. Rewriting the jump-correction term in Eq. (53) in the $x-$ direction,

$$\mathcal{J}=[\psi]_{\Gamma}+\left[\psi^{(1)}\right]_{\Gamma}\Delta^{+}+\frac{1}{2!}\left[\psi^{(2)}\right]_{\Gamma}(\Delta^{+})^{2}+\frac{1}{3!}\left[\psi^{(3)}\right]_{\Gamma}(\Delta^{+})^{3},\quad\left(\Delta^{+}=x_{j}-x_{\Gamma}\right) \tag{68}$$

where $\left[\psi^{(n)}\right]_{\Gamma}=\lim\limits_{x\to x_{\Gamma}^{+}}\psi^{(n)}(x)-\lim\limits_{x\to x_{\Gamma}^{-}}\psi^{(n)}(x)$, and x_{Γ} denotes the boundary point.

Since three ghost cells and one boundary points are given, all the terms up to the 5th-order jump-correction term can be approximated.

The one-sided finite-difference approximation for the limit values can be expressed as

$$\psi_{\Gamma}^{(n)}=\alpha_{\Gamma}\psi_{\Gamma}+\alpha_{j}\psi_{j}+\alpha_{j+1}\psi_{j+1}+\alpha_{j+2}\psi_{j+2} \tag{69}$$

where

$$\begin{bmatrix}\alpha_{\Gamma}\\\alpha_{j}\\\alpha_{j+1}\\\alpha_{j+2}\end{bmatrix}=\begin{bmatrix}1&1&1&1\\0&\Delta_{j}&\Delta_{j+1}&\Delta_{j+2}\\0&\Delta_{j}^{2}&\Delta_{j+1}^{3}&\Delta_{j+2}^{3}\\0&\Delta_{j}^{3}&\Delta_{j+1}^{3}&\Delta_{j+2}^{3}\end{bmatrix}^{-1}\begin{bmatrix}\delta_{n0}\\\delta_{n1}\\2!\delta_{n2}\\3!\delta_{n3}\end{bmatrix},\quad\Delta_{j}=x_{j}-x_{\Gamma}, \tag{70}$$

and δ_{ij} is the Kronecker delta function.

Mass conservation has also been evaluated in order to verify whether the proposed method satisfies the conservation. For two-dimensional compressible flow, mass conservation inside the computational domain including the immersed boundary can be written as

$$\int_{\Gamma}\rho\mathbf{U}_{\Gamma}\cdot\mathbf{n}_{\Gamma}\,d\Gamma+\frac{\partial}{\partial t}\int_{\Omega_{f}}\rho\,d\Omega+\int_{\partial\Omega_{f}}\rho\mathbf{U}_{f}\cdot\mathbf{n}_{f}\,dS=0 \tag{71}$$

29

where U and ρ is the velocity vector and density, and n is the surface normal unit vector. The first term in Eq. (71) represents the conservation by moving solid body which is not considered here. When the solution is sufficiently converged, the jump-correction term is calculated at each intersection point around the immersed boundary. In Figs. 9 (a) and (b), Mach contours over the three-dimensional pressure surface for the fine grid $\Delta = D/160$ are shown for the reconstructed and non-reconstructed case.
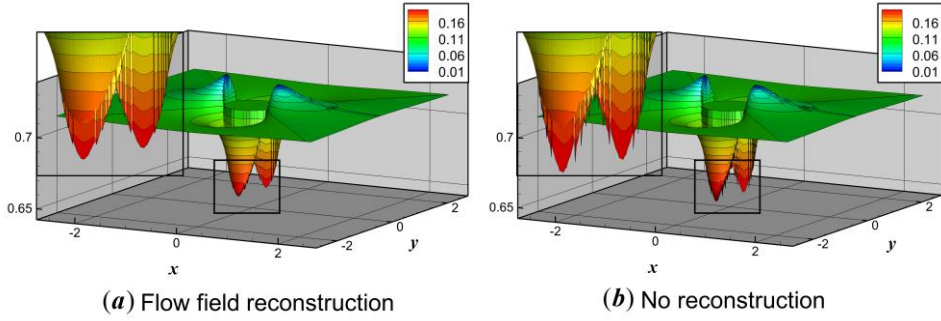

Figure 9. The Mach number contours on the three-dimensional pressure surface plot when flow reconstruction is used (a) and no reconstruction is used (b).
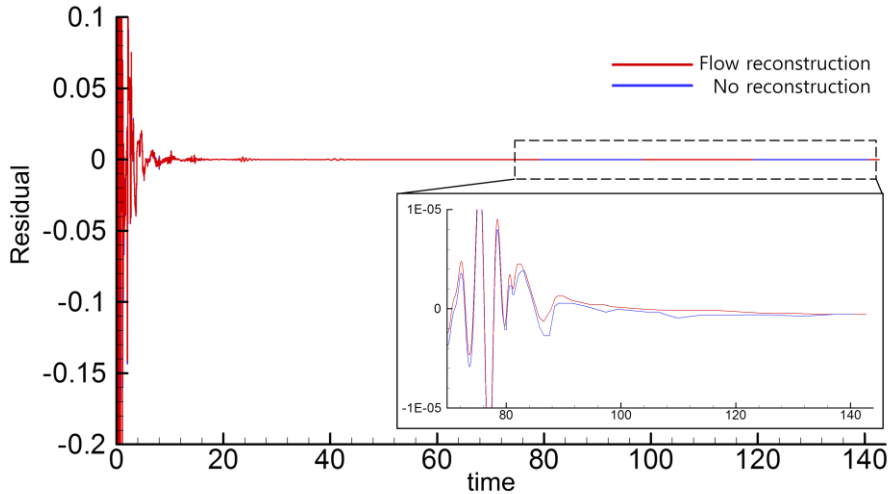
Figure 10. Residuals of mass conservation of stationary cylinders for flow reconstructed (red line) and non-reconstructed (blue line) cases.

From the enlarged figure, the field reconstruction seems to dramatically diminish the spurious oscillations near the cylinder compared to the non-flow field reconstruction result. Moreover, when the flow reconstruction is used, the Mach contour seems continuously distributed at the rear part where the cancellation error occurs. This could be attributed to the reduced jump-discontinuity by minimizing the jump-correction term. In Fig. 10, the residuals of mass conservation are plotted. It proves that there is no distinct difference in conservation due to the flow reconstruction which results in smooth solution near the immersed boundary. The results of the reduced jump-discontinuity and the pressure coefficient are depicted in
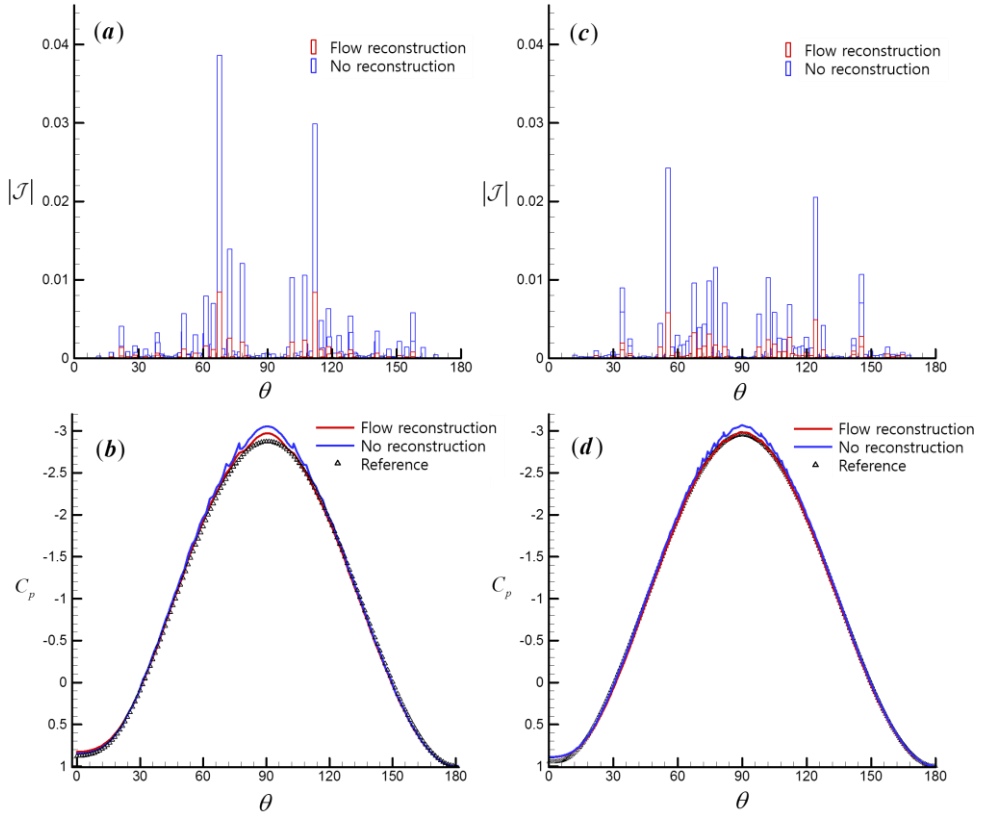
Figure 11. Jump-discontinuity magnitude and pressure coefficient distribution plots with respect to the circumferential position at the wall for the grid size $\Delta = D/80$ (a-b) and $\Delta = D/160$ (c-d).

Fig. 11 for coarse, $\Delta = D/80$ (a-b) and fine, $\Delta = D/160$ (c-d) grids. The $x-$axis refers to the circumferential position from the rear ($\theta = 0^{\circ}$) to front ($\theta = 180^{\circ}$) part. Here, body-fitted grid simulations that have the equivalent grid sizes to each case are taken as reference solutions. From Fig. 9 (a) and (c), it can be found that the jump-discontinuity increases as the angle between the normal vector of the geometry and the flow direction increases, which implies the jump-discontinuity increases as the conformity of the immersed boundary to the grid line direction decreases. Although the jump-discontinuity is not completely eliminated, a distinct decrease could be found when the flow reconstruction is applied for both coarse and fine grids.

When it comes to the pressure coefficient plots in Fig. 11 (b) and (d), it can be found that the positions of oscillations are well matched to those of the jump-discontinuity plots, which confirms the effects of the jump-discontinuity to the oscillations near the immersed boundary. For the coarse grid in Fig. 11 (b), both flow reconstructed and the non-reconstructed results show discrepancies in comparison with the body-fitted result, but relatively smaller error was found when flow reconstruction is applied, which reduced the overshoot near $\theta = 90^{\circ}$. For the finer grid sizes case in Fig. 11 (d), the error between body-fitted and immersed boundary grid solutions more reduced than coarse grid. However, it can be found that the oscillatory behavior still persists in the original IBM case where the flow reconstruction is not applied while the current solution shows good agreement with the body-fitted solution. These results imply that non-physical oscillatory behavior does not readily reduce by conventional ghost-point IBM which has no constraint except for the boundary condition. Without flow reconstruction, the ghost values inside the solid wall behave arbitrarily and this behavior becomes severe where the conformity of the immersed boundary to the grid line direction decreases. On the other hand, when the flow reconstruction is applied, ghost cell values become smoothly correlated with the flow field because the interpolations are performed with the ghost cell values and flow values in a coupled manner.

4.1.2 Subsonic viscous flow over a circular cylinder

The flow field around a circular cylinder is a well-established test case for the analysis of incompressible flows or low-Mach-number compressible flows. In this chapter, a two-dimensional viscous compressible flow with $M = 0.2$ is computed to validate the developed IBM. The two-dimensional circular cylinder is considered in a range of Reynolds numbers, from $Re = 20$ to $Re = 200$. This Reynolds number range covers both steady and unsteady states, and it is experimentally known that vortex shedding appears around $Re = 45$. The non-reflective radiation and the outflow boundary conditions are imposed [50].

Along with the high-resolution numerical method, a sufficient grid is required for computing the lift and drag coefficients, as unphysical wave reflections from the boundaries could lead to a non-negligible error. For this reason, a multi-block method is utilized, which maintains uniform structured grids for the entire domain as Fig. 12 (a). It could capture the aeroacoustics phenomenon as well as avoid domain confinement effects. Multi-grids with seven levels are used in this case study and grid sizes are doubled as the multi-grid level progresses. For the diameter of the cylinder, D, the first level grid size is set to $D/80$ to capture the nonlinear phenomena near the immersed boundary with high resolution.

For the grid level 1st to 6th, the domain size is doubled at each level from $4D \times 4D$ to $128D \times 128D$ and for the 7th level, domain size is $200D \times 200D$. As shown in Fig. 12 (b), the length of the separation region (l), the positions of the vortex center (a and b), and the flow separation angle (θ_s) are compared from the results of the steady flow. In the case of unsteady flow, periodic vortex shedding with a frequency of f_0 is captured along with the Kármán vortex street. Thus, the Strouhal number, $St = Df_0/M$, is calculated to quantify the results. For both steady and unsteady cases, lift and drag coefficients are also measured, which is known as

$$C_D = \frac{F_x}{\rho U_\infty^2 D}, \quad C_L = \frac{F_y}{\rho U_\infty^2 D} \tag{72}$$

where the total boundary force, F, by pressure and viscous effects is

$$F = -\oint_\Gamma p \cdot \boldsymbol{n} \, ds + \oint_\Gamma \tau \cdot \boldsymbol{n} \, ds \tag{73}$$

In Tables 1 and 2, the results of the flow shape parameters (for steady flow only), lift and drag coefficients, amplitude of their changes, and Strouhal number of this study are compared. The results confirm that all results of the present simulation agree very well with those reported in previous studies for both steady and unsteady flows.
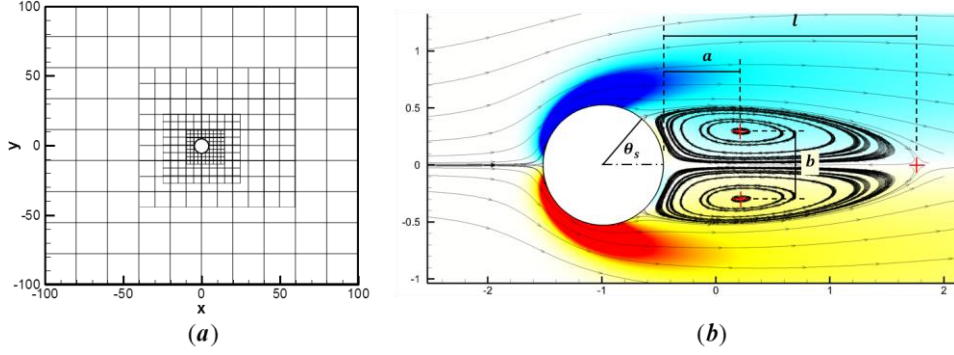
Figure 12. (a) Schematic of multigrid configuration around immersed boundary; (b) nomenclature used to capture the steady cylinder flow characteristics.

In addition, the tonal sound generation of the circular cylinder is investigated to validate the acoustic wave propagation by IBM for the $\mathrm{Re} = 200$ case. Fig. 13 (a) shows that sound pressure waves generated by vortex shedding are radiated in a dipolar nature. Alternate vortex shedding from the upper and lower sides of the cylinder produces negative and positive sound pressure waves. Because there is a free-stream with a finite Mach number, Doppler Effect can be found as well. The vorticity seems to be smeared in the downstream since the grids become coarse in the far field, but the grid size is sufficiently small enough to resolve the radiating sound waves. In Fig. 13 (b), the instantaneous fluctuation ($\Delta \tilde{p} = p - \tilde{p}$) normalized by $M^{2.5}$ along the line at $\theta = \pi/2$ and $\theta = 3\pi/2$ is shown where the mean pressure $\tilde{p}$ is defined as

$$\tilde{p} = \frac{1}{t_2 - t_1} \int_{t_1}^{t_2} p(x, y, t) \, dt \tag{74}$$

According to Curle's acoustic analogy, the scaling law $\Delta \tilde{p}/M^{2.5} \propto r^{-1/2}$ holds true in two-dimensional wave propagation. In this case, the normalized amplitudes in log

34

scale shows the slope of $-1/2$, which may confirm that the current IBM is suitable to analyze aeroacoustics problems.

**Table 1.** Comparison of flow characteristics for steady flow around two-dimensional circular cylinder.

	Re = 20					Re = 40				
	l	a	b	θ_s	C_D	l	a	b	θ_s	C_D
Coutanceau and Bouard	0.93	0.33	0.46	45.0	-	2.13	0.76	0.59	55.8	-
Linnick and Fasel	0.93	0.36	0.43	43.5	2.06	2.28	0.72	0.60	53.6	1.52
Taira and Colonius	0.94	0.37	0.43	43.3	2.06	2.30	0.73	0.60	53.7	1.54
Daniel Canuto and Taira	0.92	0.36	0.42	43.7	2.07	2.24	0.72	0.59	53.7	1.54
Brehm	0.96	0.36	0.42	44.0	2.02	2.26	0.72	0.58	52.9	1.51
Present	0.92	0.36	0.43	43.8	2.01	2.28	0.72	0.59	53.7	1.50

Table 2. Comparison of flow characteristics for unsteady flow around two-dimensional circular cylinder.

	Re $= 100$			Re $= 200$		
	C_D	C_L	St	C_D	C_L	St
Liu	1.35 ± 0.012	± 0.339	0.165	1.31 ± 0.049	± 0.690	0.192
Mimeau	1.40 ± 0.010	± 0.320	0.165	1.44 ± 0.050	± 0.750	0.200
Linnick	1.34 ± 0.009	± 0.333	0.166	1.34 ± 0.044	± 0.690	0.197
Brehm	1.32 ± 0.010	± 0.320	0.165	1.30 ± 0.040	± 0.660	0.192
Present	1.36 ± 0.011	± 0.320	0.166	1.33 ± 0.040	± 0.680	0.194
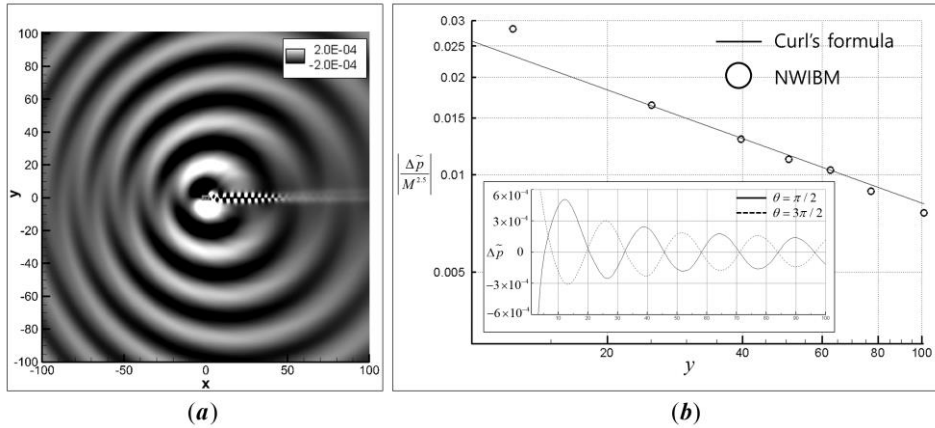
Figure 13. (a) Gray contour of non-dimensional instantaneous fluctuation pressure propagation; (b) amplitude of scaled non-dimensional instantaneous fluctuation pressure (inset is non-dimensional instantaneous fluctuation pressure at $\theta = \pi/2$ and $\theta = 3\pi/2$)
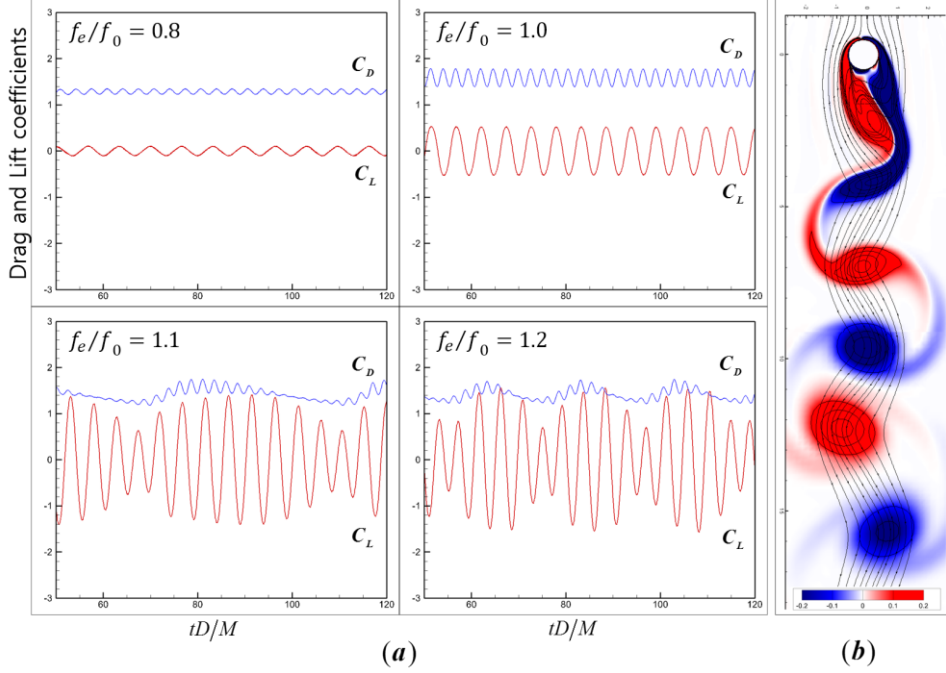
Figure 14. (a) Drag and lift coefficients as functions of non-dimensional time for transversely oscillating cylinder with various excitation frequencies; (b) instantaneous streamlines and vorticity contours at $f_e/f_0 = 0.8$.

To verify the proposed IBM working in a moving situation, a transversely oscillating cylinder in a free stream is also demonstrated. The equation of motion, $y(t) = A\cos(2\pi f_e t)$, is determined by the oscillation amplitude A and the excitation frequency f_e. All of the computational methods and domains remain the same as the previous case, and the grid size near the cylinder is $D/40$. The computation is performed at $\mathrm{Re}_D = 185$ with the motion parameters of $A = 0.2D$ and f_e/f_0, $\in \{0.8,\ 0.9,\ 1.0,\ 1.1,\ 1.12,\ 1.2\}$ where the natural shedding frequency in this case is found to be $f_0 = 0.189 U_\infty/D$ at the free stream velocity $M_\infty = 0.2$.

Fig. 14 (a) presents the drag and lift coefficients in the inertial reference frame for various excitation frequencies. The drag and lift behaviors are fairly regular once vortex shedding is established, but the flow pattern changes evidently with respect to f_e/f_0. The force variations shows stable vortex shedding up to $f_e/f_0 = 1.0$, showing a classical Kármán vortex phenomenon. This regularity of force variations

36

is lost at some point near $f_e/f_0 > 1.0$, and the drag and lift exhibit regular signs of the influence of a higher harmonic. One can refer to previous studies to find good consistency of the present results of force variations with the incompressible results [51]. Quantitative comparison by the average and root-mean-square values of the force coefficients are drawn in Fig. 15 (a). It can be seen that at $f_e/f_0 = 1.1$, the time-averaged drag force $\bar{C}_d$ peaks and decreases as the excitation frequency increases, indicating that the point of resonant synchronization occurs at $f_e/f_0 = 1.0$. The lift force C'_{rms} grows monotonically with increased excitation frequency. The pressure coefficient distribution along the cylinder surface is shown in Fig. 15 (b) and (c) for $f_e/f_0 = 0.8$ and $f_e/f_0 = 1.1$ at the instant of the positive peak.
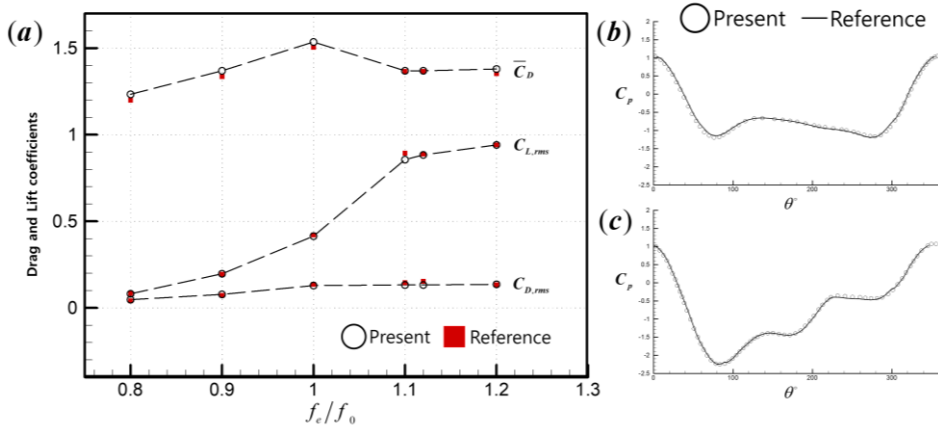
Figure 15. (a) Comparison of the mean drag coefficient, root-mean-squared drag coefficient and lift coefficient of a transversely oscillating cylinder; pressure coefficient distribution along the cylinder surface at (b) $f_e/f_0 = 0.8$ and (c) $f_e/f_0 = 1.1$.
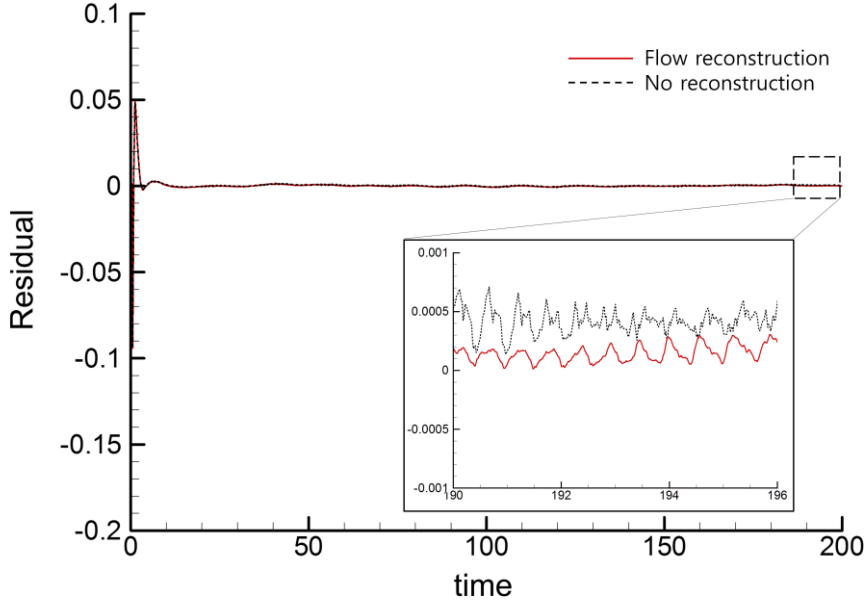
Figure 16. Residuals of mass conservation of oscillating cylinders for flow reconstructed (red line) and non-reconstructed (black dotted) cases.

The present results do not seem to be distinguished from those in the original research by Guilmineau et al. [51] in terms of the accuracy compared to the results of the incompressible body-fitted method. This implies the flow reconstruction method does not hamper the overall accuracy.

Throughout the application of the moving body problem, it can be verified that the validity of present compressible IBM, which is meaningful considering that it is quite challenging to accurately predict the vortex shedding dynamics as well as it can be further applied to fluid-structure interaction problems. In order to verify the conservation property in moving case, mass conservation for $f_e/f_0 = 0.8$ case is calculated.

In Fig. 16, time dependent residuals show similar conservation property for both flow reconstructed and non-reconstructed results, which proves there is no distinct difference in conservation due to the flow reconstruction in moving case as well. From the enlarged inset figure, flow reconstructed case shows even better conservation property compared to non-reconstructed case. It can be attributed to

38

reduced jump-discontinuity which results in less oscillations that hampered the conservation in original IBM.

4.1.3 Blade Vortex Interaction

The present method is applied to Blade-Vortex Interaction (BVI) in order to demonstrate the effects of NWIBM with field reconstruction. Since BVI is highly related to discrete frequency noise generation in practical engineering problem, uniform grid system where IBM can readily be used is recommended in order to capture the acoustic wave propagation by minimizing dispersion and dissipation.

In this study, a counter rotating vortex located five times of chord length (c) from the leading edge of NACA0012 airfoil with zero angle of attack within the uniform flow of $M = 0.5$ is calculated. For the analytical structure of the vortex to closely resemble the one measured in the experiments [52], a vortex model by Sculley [53] is used that is expressed as

$$\frac{v_\theta}{M} = \frac{\Gamma}{2\pi r}\left(\frac{r^2}{r^2 + r_v^2}\right) \tag{75}$$

where Γ is the maximum circulation divided by the freestream velocity and the chord length (c), r_v is the core radius vortex and r is the distance from the center of the vortex. Following Lee's experiments [52], the initial vortex parameters are set as $\Gamma = -0.283$ and $r_v = 0.018c$. The pressure and density for the vortex convecting in the freestream are related by

$$\frac{dp}{dr} = \frac{\rho v_\theta^2}{r} \tag{76}$$

where the density is obtained from

$$\frac{\gamma p/\rho}{\gamma - 1} + \frac{v_\theta^2}{2} = \frac{\gamma p_\infty/\rho_\infty}{\gamma - 1} \tag{77}$$

The domain size is $[10 \times 10]$ with grid sizes of $\Delta = c/200$ and initial vortex propagates after steady solution by uniform flow is calculated. The steady static pressure solution of present method is compared with when only low-order (IDW) or high-order IBM (WLSQ) is used in Fig. 17. The overall numerical results in the left of Fig. 17 seem almost identical to each other, but spurious oscillations near leading edge are observed for both IDW and WLSQ cases in the enlarged figure

39

(right). In addition, the solution by NWIBM shows more attached pressure distribution around leading edge while the other solutions show discrete pressure distributions.
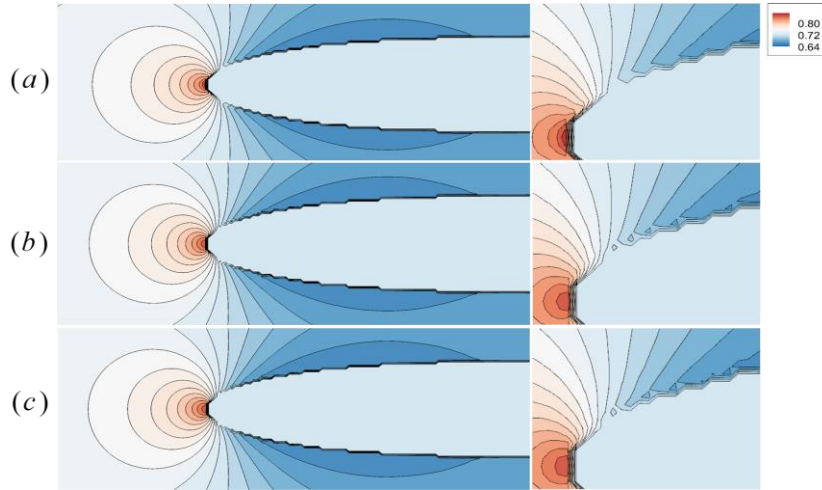

Figure 17. Pressure distribution of steady solutions by (a) NWIBM, (b) IDW and (c) WLS
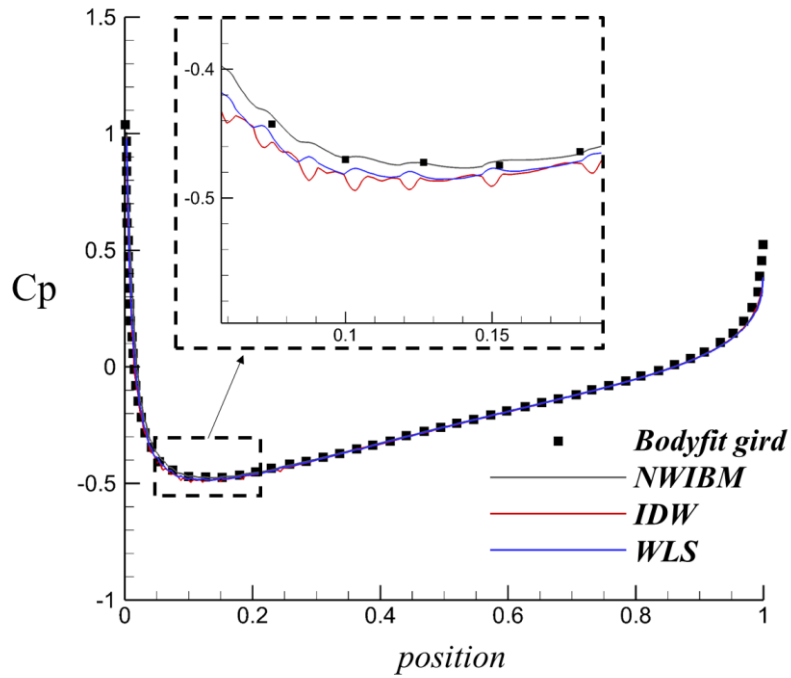
Figure 18. Pressure coefficients of steady solutions

This discrepancy is more clearly observed in the pressure coefficient (C_p) plot in Fig. 18. As a reference, body-fitted grid solution [54] is also plotted. It can be found that the effects of the field reconstruction seem to enhance the accuracy in the leading edge where the grid non-conformity is more severe.

As vortex approach, precursor wave which is negligible to the secondary acoustic waves is generated. Fig. 19 shows pressure perturbation by $\Delta p = p - p_{steady}$ after vortex collides to the airfoil. At the leading edge, the initial vortex is split into two each of which propagates to pressure side and suction side of the airfoil, respectively. This vortex splitting induces three dipole type acoustic waves which seem to be bended by steady flow that propagates in downstream as shown in Fig. 19 (a). As vortices move forward along with the upper and lower walls of the airfoil, third acoustic waves are observed when these vortices pass the trailing edge of the airfoil in Fig. 19 (b). However, the magnitude of this 3rd acoustic waves are much smaller than the 2nd acoustic waves that are created by vortex head-on the airfoil.
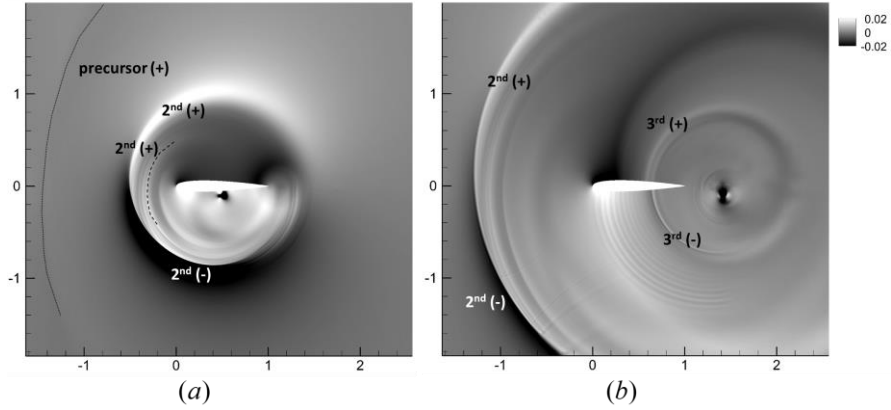
Figure 19. Instantaneous acoustic pressure at (a) *t*=5.4 and (b) *t*=6.8

In Fig. 20, quantitative comparison by pressure coefficient at the lower wall position of $0.02c$ and $0.1c$ from the leading edge. It has been found that NWIBM shows better agreement with the experiment. Moreover, the oscillations after vortex passes by were not observed in the present method. Similar to the steady solution, it can also be attributed to field reconstruction that reduces oscillations near the immersed wall boundary. Hence, the current algorithm has advantages over conventional IBMs even in the numerical analysis for the aeroacoustics.
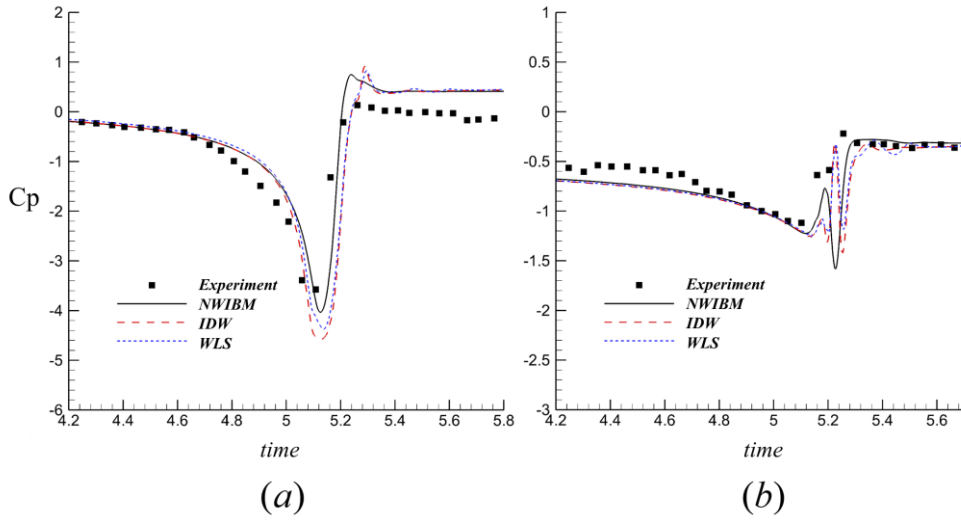
Figure 20. Time history of pressure coefficient at lower wall positions of (a) *0.02c* and (b) *0.1c*

4.2 Supersonic flow problems

### 4.2.1 Flow over a circular cylinder

Inviscid flow past a two-dimensional circular cylinder was considered as a suitable verification problem to show enhanced performance for general inflow condition within the incompressible and compressible ranges. The viscous effect was not considered, because physical damping by viscous flux can eliminate the spurious oscillations stemming from the ill-conditioned immersed boundary or jump discontinuity. Numerical analysis was conducted within a rectangular domain with dimensions $100D \times 100D$ for the subsonic inflow case and $18D \times 10D$ for the supersonic inflow case, with D being the diameter of the circular cylinder located at the center of the domain. In the subsonic inflow case, Mach number $M = 0.2$ was chosen as the initial inflow condition, which can approximate the incompressible flow. Because the incompressible potential flow solution is known, the numerical results of the subsonic inflow cases were compared with the analytical solution based on the assumption that the pressure deviation error between the low Mach number and incompressible flow is proportional to $O(M^4)$ [55]. On the surface of the cylinder, the potential theory solution was used to calculate the

pressure coefficient. Fig. 21 (a) shows that the conventional high-order direct (WLS) and low-order mirror-image (IDW) IBMs fail to reproduce the pressure coefficient of the potential theory solution in the subsonic flow.
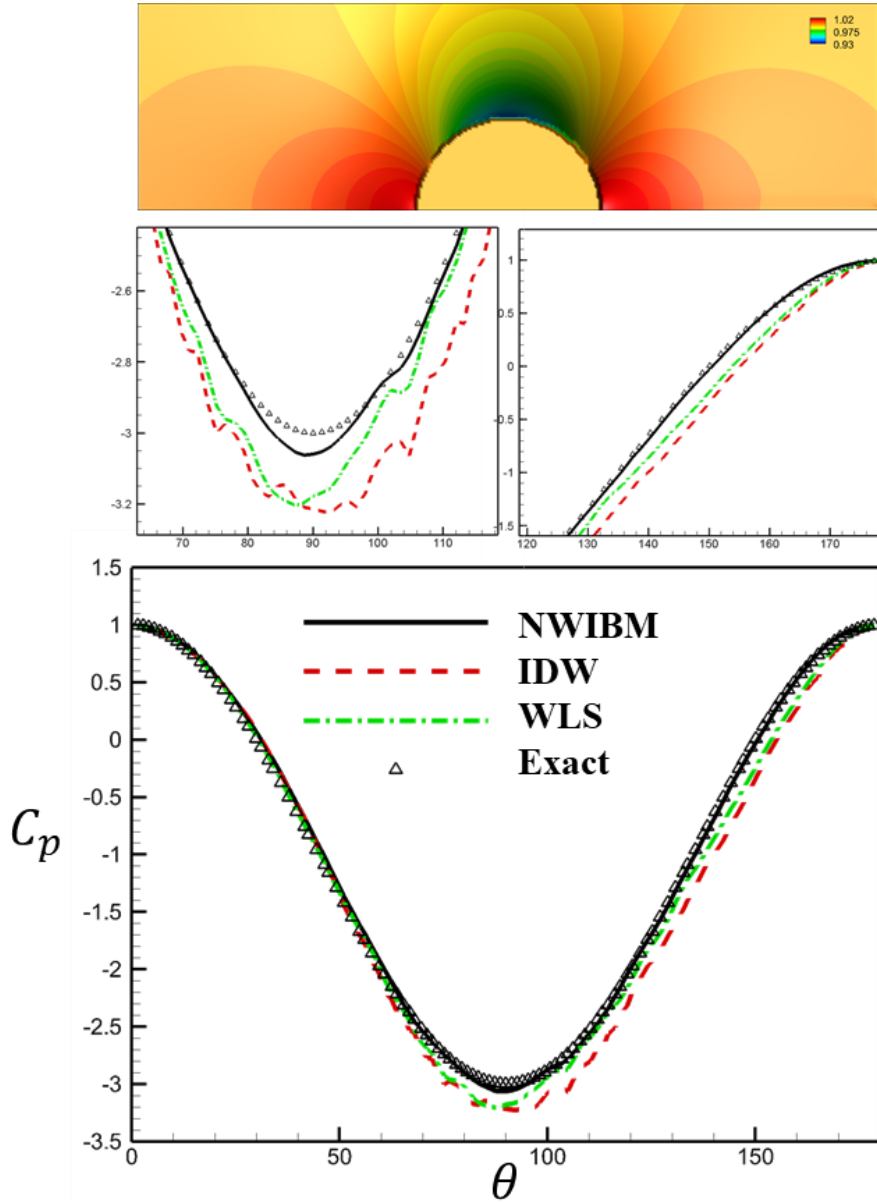
Figure 21. Pressure coefficient distributions with respect to the circumferential position of subsonic ($M = 0.2$) flow over two-dimensional circular cylinder

Even if the high-order reconstruction shows better results than the low-order one, the discrepancy still persists as the gradient near the wall becomes smoother where the jump discontinuity by the immersed boundary becomes dominant. However, the NWIBM shows good agreement with the potential theoretical solution with smooth variation of the pressure coefficient. Such enhanced smoothness near the wall can be attributed to the reduction of the jump discontinuity by field extension. NWIBM was designed to include the field-extension process where the high-order weighted reconstruction is dominant to obviate the jump discontinuity.
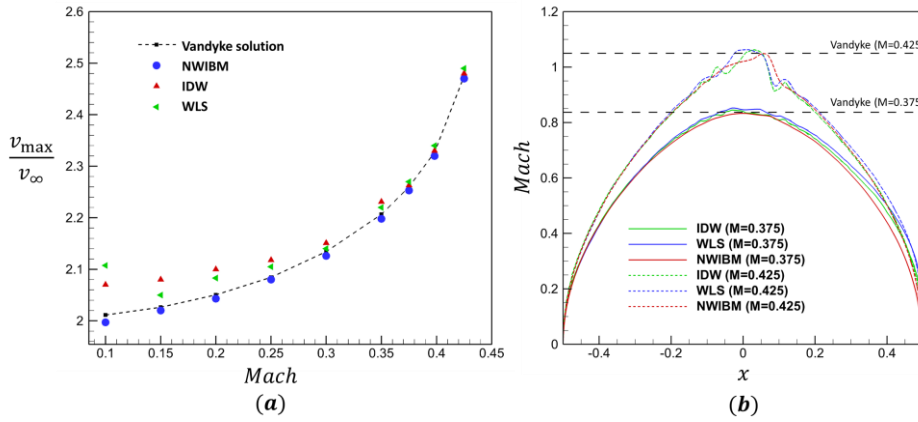
Figure 22. Comparison of IBMs with respect to (a) Dependence of maximum velocity on freestream Mach number and (b) Mach number plot along the flow directional position

In addition, quantitative comparison with respect to Mach number is calculated. Figure 22 (a) shows the maximum velocity on the circle as a function of the freestream Mach number. The value of this maximum increases with freestream Mach number, and it reaches critical Mach number theoretically [56] when Mach number is 0.3982. The results are compared with those found from Van Dyke's series expansion [57]. It can be found that NWIBM shows good agreement with the theoretical solutions, while the conventional high-order (WLS) and low-order (IDW) methods show large errors especially in the low Mach numbers. In case of IDW method which uses low-order reconstructions for ghost-cell, the errors become more severe as Mach approaches to the incompressible limit, while errors of WLS which

uses high-order reconstructions show larger error as Mach approaches to the compressible regime that slightly includes the discontinuity. Such discrepancy is due to oscillations near the immersed boundary as shown in Fig. 22 (b).
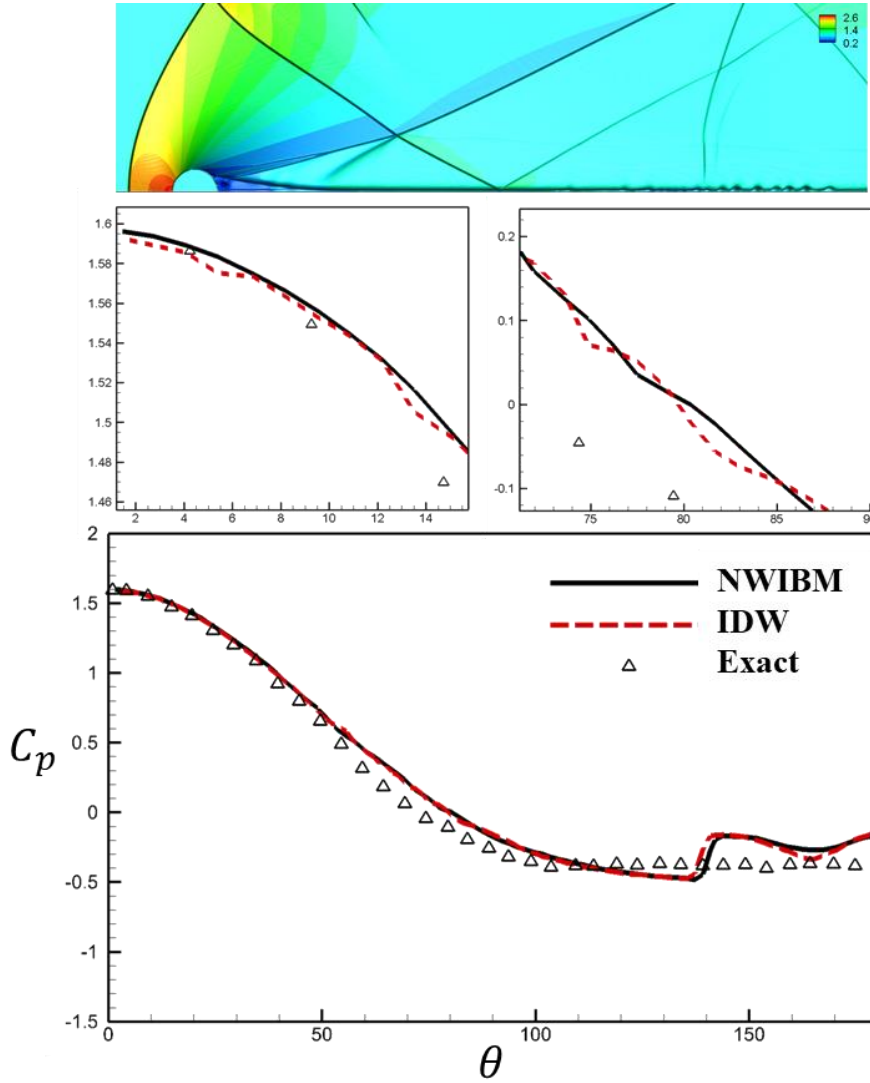
Figure 23. Pressure coefficient distributions with respect to the circumferential position of supersonic ($M = 1.7$) flow over two-dimensional circular cylinder

In the case of supersonic inflow, the inflow condition of $M = 1.7$ was chosen. Because there is no analytical solution, the computational results was compared with experimental results [58]. In Fig. 23, the supersonic flow result of the pressure coefficients obtained by the present method was compared with that of the IDW

method. In this case, immersed boundary reconstruction by WLS was found to diverge because it accommodates high-order interpolation. The accuracy also increased in the supersonic flow, but not as much as in the subsonic case. Because the upwind characteristics of the WENO scheme removed the spurious oscillations, the overall pressure coefficients obtained by both methods agree reasonably well with the experimental data. However, the conventional mirror-image method still shows inferior oscillatory behavior along with the geometry because of low-order interpolation, which results in an inaccurate solution. Meanwhile, the NWIBM shows a more accurate solution because of its introduction of high-order interpolation.

4.2.2 Supersonic flow over a wedge

The supersonic flow over a solid body is tested to confirm the numerical validity of the current method where the flow discontinuity occurs. A well-known test case motivated by Chaudhuri [13] is adopted, as illustrated in Fig. 24(a). A wedge with deflection angle θ in supersonic flow with Mach number M produces an oblique shock wave with angle β over the wedge, and their theoretical relation $\theta - \beta - M$ is known to have the following form:

$$\tan \theta = 2 \cot \beta \left[\frac{M^2 \sin \beta - 1}{M^2 (\gamma + \cos 2\beta) + 2} \right] \tag{78}$$

In this example, the inviscid flow field initialized with $M = 3.5$ is considered on a computational domain size of 12×3, normalized by the horizontal length with 2000×501 grids, which have been found to be suitable for convergence in this problem. The supersonic inflow and outflow boundary conditions are applied to the inlet and outlet boundaries. In the case of the wall boundary, the adiabatic slip-wall condition with zero-normal velocity is imposed on the immersed boundary and both upper and lower boundaries. For comparison, a simulation in the body-fit grid simulation with around 1.1 million cells is also carried out as in Fig. 24(b), where the grid size near the body is matched to the grid for the immersed boundary case.
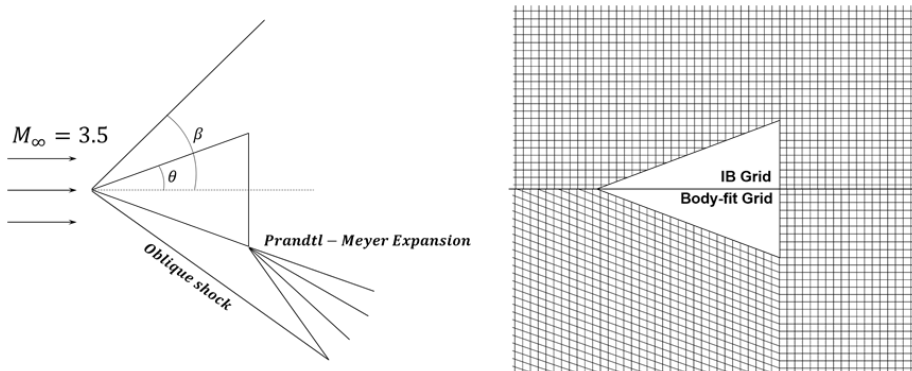
Figure 24. Schematic diagram for the supersonic flow over the triangular prism (left) and enlarged pictures of two different grid configurations for simulation (right)

Figure 25 shows the numerical Schlieren for the solutions at the deflection angles of $\theta = 5°$, $10°$, and $20°$ of the present results (upper half) and the body-fit grid simulation (lower half). The generation of oscillating wakes behind the objects are due to the numerical viscosity by non-linear governing equations that become more complex for the more-deflected wedge. As the deflection angle gets larger, the oblique shock angles also increased. The oblique shock angles for three deflected prisms are reported in Table 3. The predicted oblique shock angles by the current solver show good agreement with the analytical solutions.

This consistently excellent agreement with the analytical solutions for all three different prism deflection angles demonstrate the validity of the NWIBM even for the supersonic compressible flow problems accompanying local flow discontinuous and smooth regions.
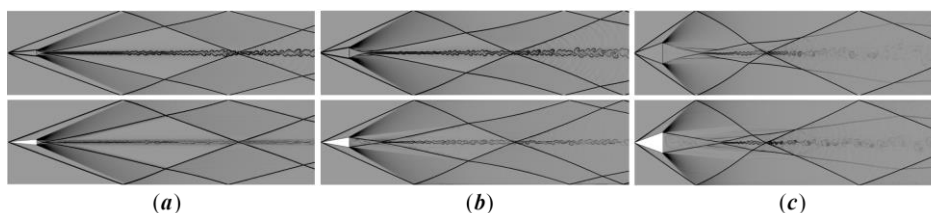
Figure 25. Schematic diagram for the supersonic flow over the triangular prism (left) and enlarged pictures of two different grid configurations for simulation (right)

Table 3. Comparison of oblique shock angles for three deflected wedges

	$\theta = 5°$	$\theta = 10°$	$\theta = 20°$
NWIBM	20.2°	24.4°	34.6°
Body fit	20.3°	24.5°	34.7°
IDW	20.1°	24.4°	34.5°
Exact	20.19°	24.39°	34.61°

4.2.3 Shock-vortex interaction problem

Let us consider the case of shock-vortex interaction and diffraction problem by moving the shock wave past a two-dimensional triangular prism with a deflection angle of $30°$. This kind of flow-wedge interaction, the so-called Schardin's problem [59], occurs when a valve or membrane is suddenly opened. Subsequently, ejected shock waves hit an object, resulting in unsteady flow characteristics. The initially prescribed discontinuity moves to the downstream only to collide against the triangular prism as shown in Fig. 26 (a). When the right state of the normal shock waves (ρ_R, u_R, p_R) are considered quiescent ambient state, the flow variables of the left state can be defined based on shock relations as:

$$u_L = M_s - c_L \sqrt{\frac{M_s^2(\gamma-1)+2}{2\gamma M_s^2 - (\gamma-1)}}, \quad \rho_L = \rho_R \frac{(\gamma+1)M_s^2}{(\gamma-1)M_s^2+2}, \quad p_L = p_R \frac{2\gamma u_1^2 - \gamma+1}{\gamma+1} \quad (79)$$

where M_s is the moving shock Mach number, and c_L is speed of sound.

After the moving shock is impinged on the prism, complex flow patterns arise with time evolution before and after the moving shock front, such as reflected shock, slip lines, vortices, and vortexlets. For the analysis, 3360×2500 grids are used, and a body-fit grid simulation is also performed with the equivalent grid size.

The numerical results by a sequence of numerical Schlieren snapshots are qualitatively compared with the experimental results [60] in Fig. 26 (b). It can be found that the overall flow physics such as vortex cores and shear lines have been well reproduced from the present simulation. In particular, the vortexlets are

distinctively matched with the experiment in the last sequence. Detailed flow characteristics of the present problem are reported by Chang and Chang [60] .
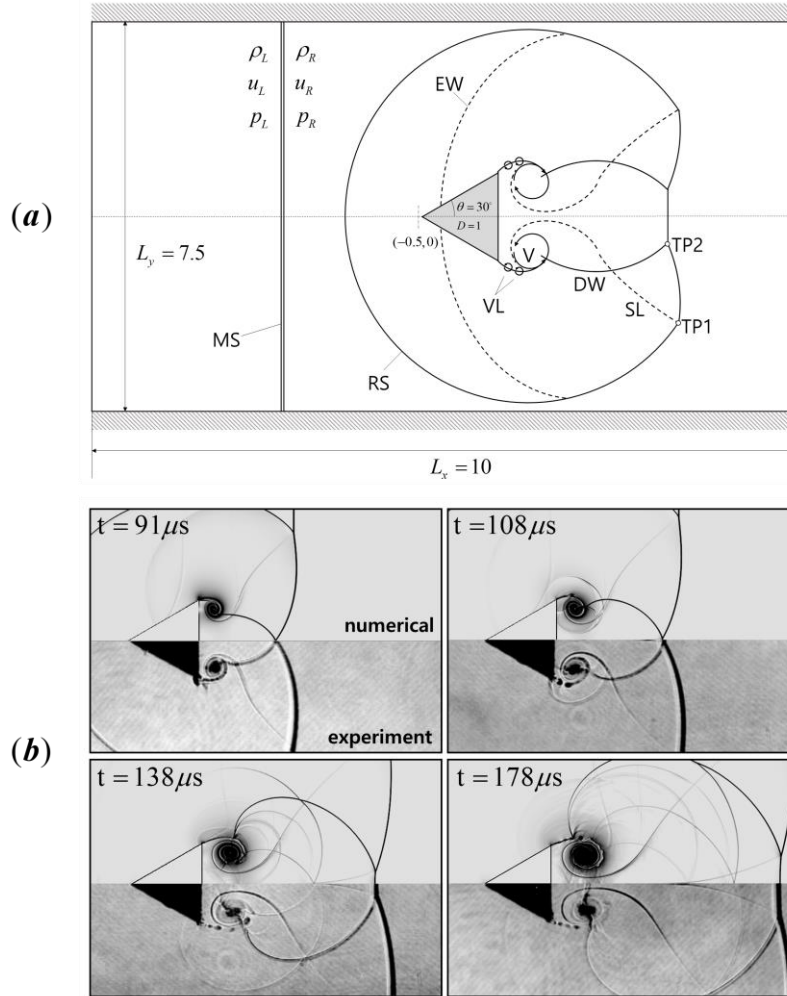
Figure 26. (a) Schematic diagram of shock–vortex interaction problem within the computational domain. MS: moving shock; RS: reflected shock; EW: expansion wave; V; vortex core; VL; vortexlet; DW: decelerated wave; SL: slip line; TP1, TP2: Mach triple points; (b) Comparison of numerical (upper) and experimental (lower) shock-vortex dynamics for Schardin's problem.
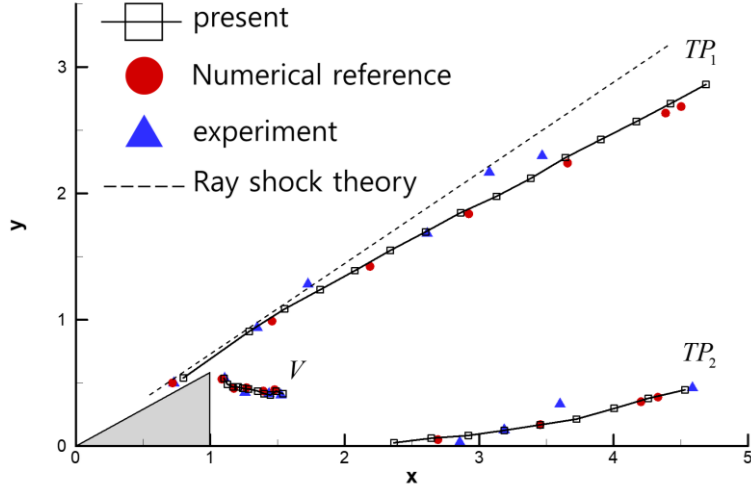
Figure 27. Comparison of triple points and vortex core trajectory.

Time evolutionary trajectories of triple points and vortex locus are compared between the present result and previous numerical and experimental studies in Fig. 27. The behavior of triple points and vortex locus seem comparable to the previous studies, which confirms the validity of applying the present IBM to complex flow problems. Additionally, the results by NWIBM are qualitatively compared with IDW and body-fitted grid results in order to verify the non-oscillatory behavior in the supersonic flow. In the first and second column of Fig. 28, density plots of the upper half-plane of the prism are compared at $50\mu s$ and $100\mu s$. The global behavior among three cases seem similar, but it can be found that IDW results show propagation of oscillation stemmed from the slant face of the prism.

This can be found more evidently in the shadowgraph plots in Fig. 29. Since the smooth region being developed after the reflected shock expanding into the upstream passes by, the conventional IBM is found to induce spurious waves. This again confirms the lemma from previous studies that the non-grid conforming interface is highly prone to the jump-discontinuity, which induces oscillations hampering the high-resolution simulation. However, such phenomenon is dramatically reduced in the present result because of nonlinear weighting process along with the reduction in the jump-discontinuity. Compared to the conventional approach, the result shows better agreement with that of the body-fitted grid simulation.
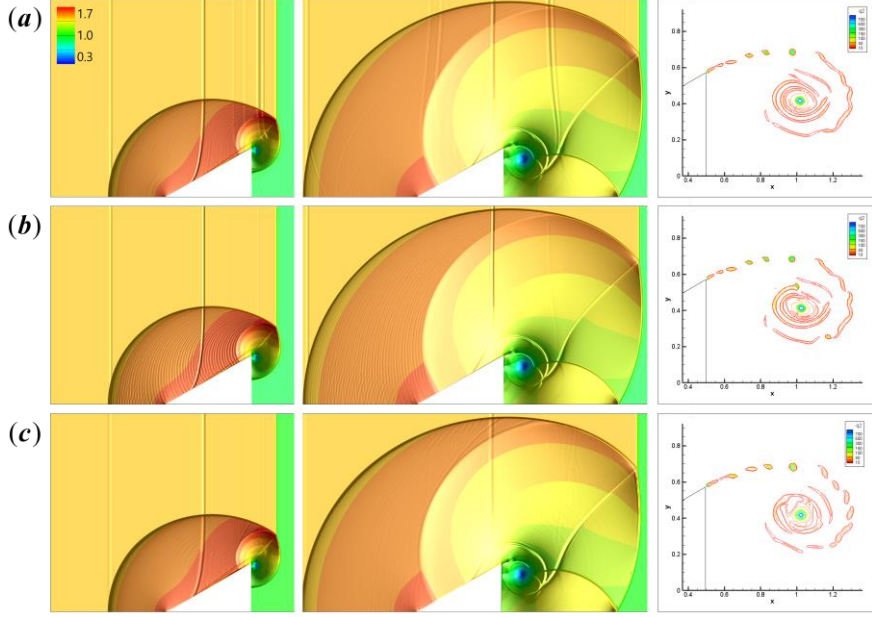
Figure 28. Density contours of shock-vortex interaction transition (first and second column) and Q_2 contours of vortexlets at the rear edge of the prism (third column) for (a) body-fit grid results, (b) IDW; (c) NWIBM.

The vortex behavior of the rear side by utilizing the $Q_2 - criterion$ is also analyzed, which is defined as

$$Q_2 = \left(\partial u_x \partial v_y - \partial u_y \partial v_x \right) - \left(\partial u_x + \partial v_y \right)^2 \tag{80}$$

For $Q_2 > 0$, the embedded shocks are excluded while capturing the coherent vortex effectively. In the third column in Fig. 28, Q_2 contours are shown at $150\mu s$ when the flow become sufficiently developed. Because the Kelvin–Helmholtz instability occurs at the rear edge of the prism along the slip lines, a string of vortexlets is captured. It is shown that the configuration and numbers of vortexlets seem identical to each other except for experiencing slightly different behavior after the vortexlets are merged because of the numerical hysteresis by different wall boundary methods. Hence, it can be confirmed that the current algorithm accurately captures the flow physics in the complex discontinuous region as well as shows non-oscillatory performance in the smoothly varying region.

(b)
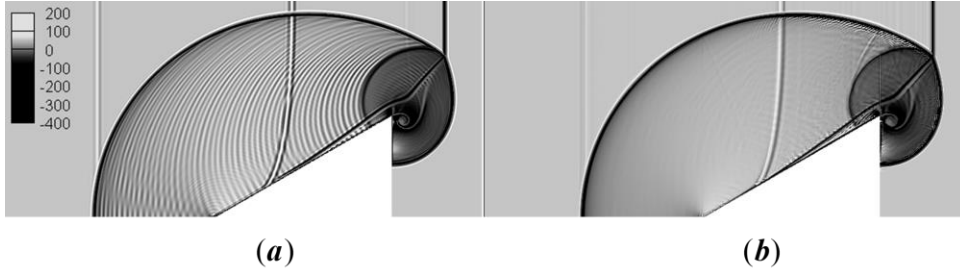
Figure 29. Shadowgraph plots of upper half-plane of the prism (first column) for (a) IDW and (b) NWIBM.

4.2.4 Double Mach reflection

The double Mach reflection of a strong shock is an extensively studied benchmark problem [19,20,25] for numerical analysis of Euler equations in that the jet flow formed along the boundary is highly sensitive to numerical schemes. Moreover, it is a particularly well-suited example to test the new method because the numerical solution depicts a highly discontinuous region as well as smooth regions. Numerical analysis was carried out in a rectangular domain with dimensions 3×2, and the rigid ramp starts from $x = 1/6$ with an angle of $30°$ to the moving-shock direction. An initial moving shock starts with a shock speed of $M = 10$ with preshock values of density $\rho = 1/4$ and pressure $p = 1$, and their postshock values can be found by Rankine–Hugoniot shock relations. In this study, two set of configurations are chosen, one of which is IBM and the other is body-fitted grid configuration as shown in Fig. 30.

Mach 10 shock Immersed wall boundary 30°
(a)

Mach 10 shock 60° Bodyfitted wall boundary
(b)
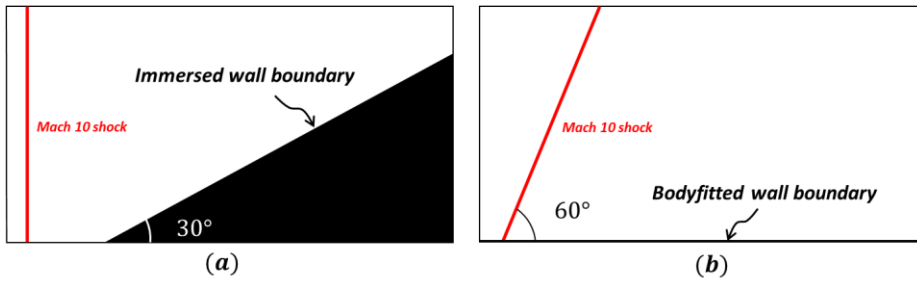
Figure 30. Geometry configurations for (a) immersed boundary and (b) body fitted calculations.

In Fig. 31 (a), the density contours obtained by the NWIBM and the IDW method are plotted over the contour of a body-fitted grid with the same grid size of $\Delta = 0.003$ at nondimensional time $t = 0.2$.

It was observed that complex structures of shock evolve as the moving shock runs up the ramp. As the reflected shock runs into the primary slip line, a curled jet flow is formed. In the enlarged Figs. 31 (b) and (c), the NWIBM shows a better resolution of this jet flow. Moreover, the smooth region behind the slip line shows oscillatory behavior in the IDW method, whereas it is clearly formed in the NWIBM. Such improved results of the present method are more evident in the density plots in Fig. 32. Although the global behaviors of both approaches seem to agree well with the body-fit grid solution, oscillations were found near the smoothly varying regions. Such a discrepancy was also found in the coarse grid, which implies that grid refinement increases the accuracy of the solution. However, it cannot fundamentally solve the oscillatory behavior stemming from jump discontinuity and low-order boundary formulation.
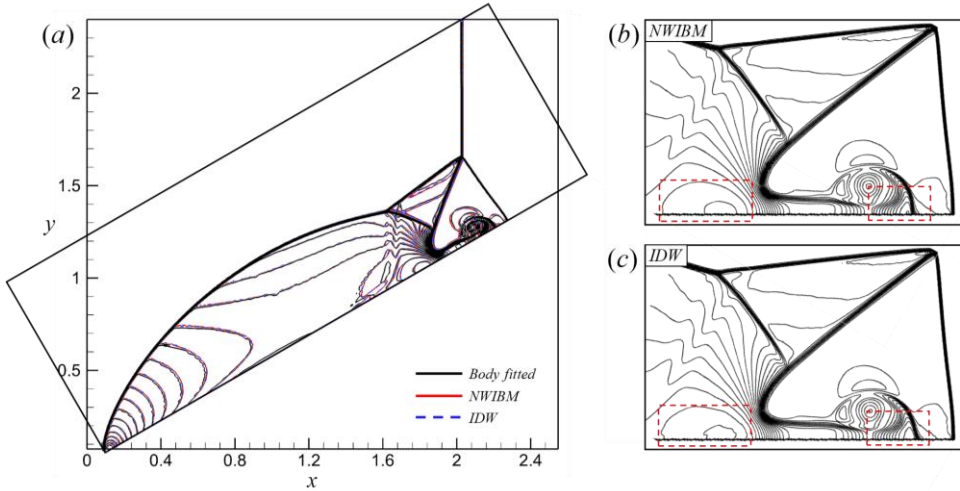
Figure 31. (a) Line density contour results of NWIBM and IDW plotted over a body-fitted grid result and enlarged figures of (b) NWIBM and (c) IDW: 50 density lines from 1.4 to 20
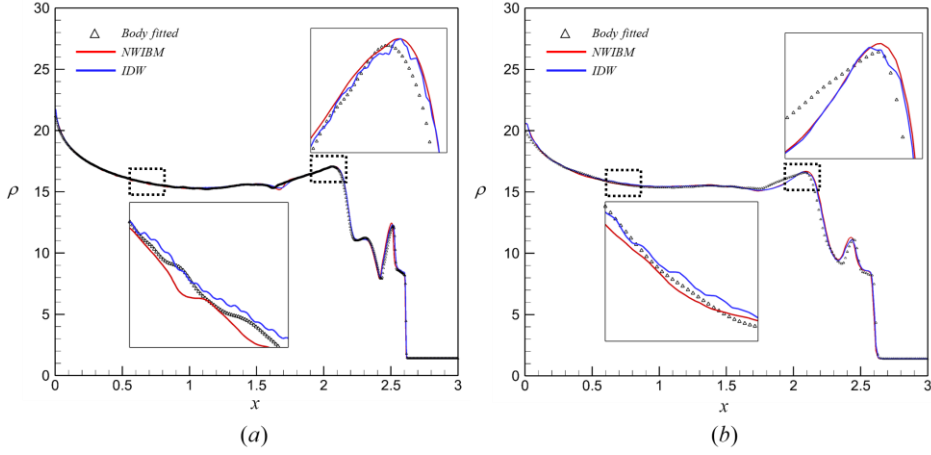
Figure 32. Density along the ramp wall with (a) fine and (b) coarse grids: inset is the enlarged plot in the smoothly varying region
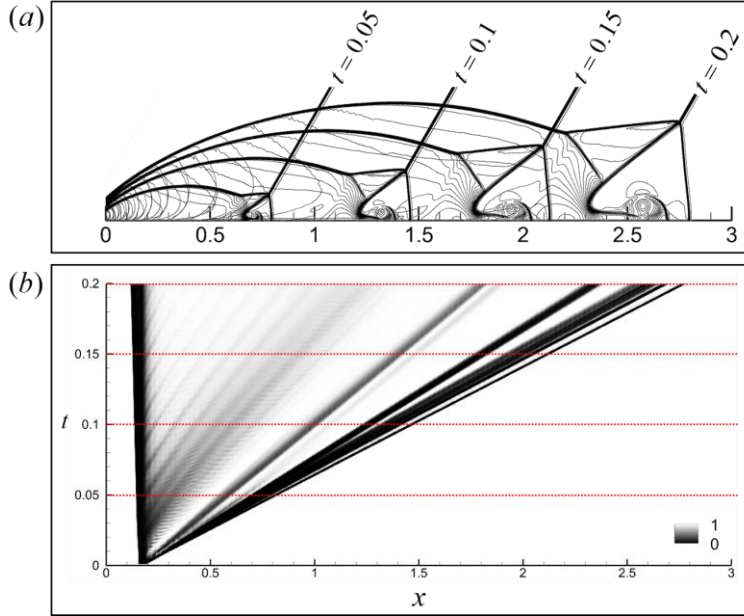

Figure 33. (a) Overlapped density contours by NWIBM at four time sequences and (b) time–space diagram of the nonlinear weighting

In Fig. 33 (a), four time sequences of overlapped density contours obtained by the NWIBM are plotted as the incident shock passes along the ramp. To determine how practically the nonlinear weighting operates as the flow field evolves, a time–space diagram of the nonlinear weightings was plotted, as shown in Fig. 33 (b), where

$x-axis$ is the position along the ramp, as in Fig. 33 (a). It was determined that the high-order interpolation is maintained before the shock arrives by showing a unity nonlinear weighting ($\omega^H = 1$). The nonlinear weighting radically decreases when the incident shock arrives, which implies the portion of high-order weighting decreases and low-order interpolation becomes active. After the incident shock passes, nonlinear weighting continuously recovers to unity because of the smoothly varying region behind the shock waves. Such a variation of nonlinear weighting corresponds well to the density contour. As a result, it was validated that the proper operation of the nonlinear weighting makes the solution more accurate and stable than those of the conventional IBMs.

Computational costs are also compared in Fig. 34, which shows discrepancies among each approaches. It is obvious that body-fitted configuration requires large computational cost compared to immersed boundary configuration since immersed boundary configurations take less fluid region as can be found in Fig. 30. When it comes to the comparison between NWIBM and conventional IDW approach, NWIBM takes more computational time because of its additional nonlinear weighting algorithm. However, it becomes negligible as the grid size decreases, which implies that the portion of the algorithm calculation is marginal compared to the calculation costs of flux and time integration.
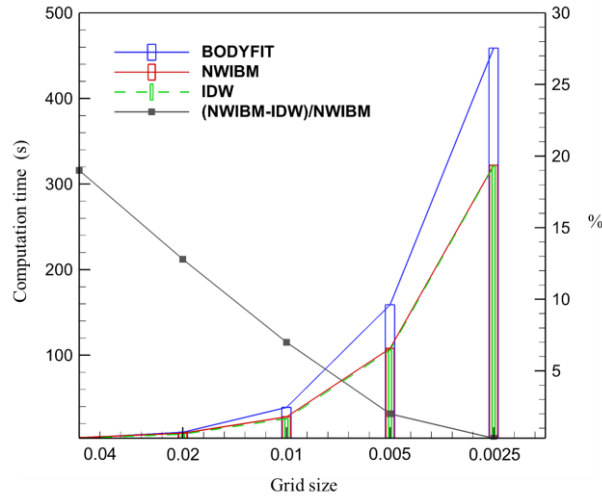
Figure 34. Comparison of computational cost with respect to the grid sizes
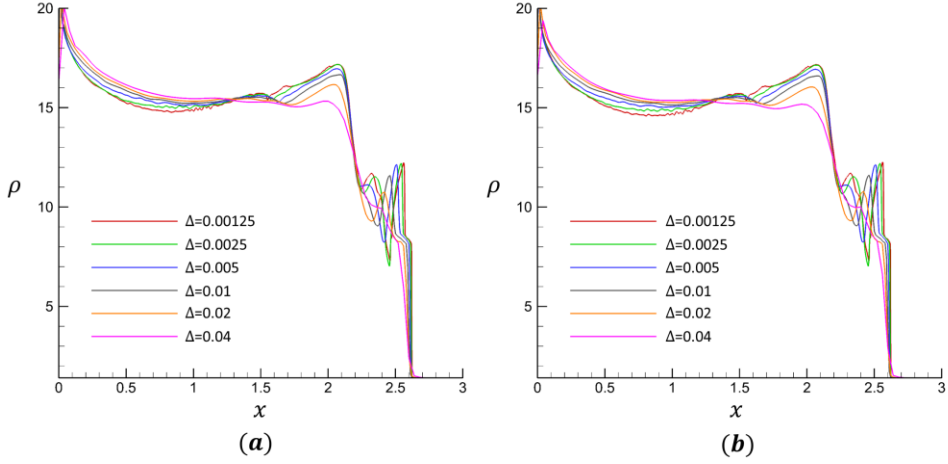
Figure 35. Density along the ramp with body-fitted configuration using (a) NWIBM and (b) conventional body fitted method with respect to grid sizes
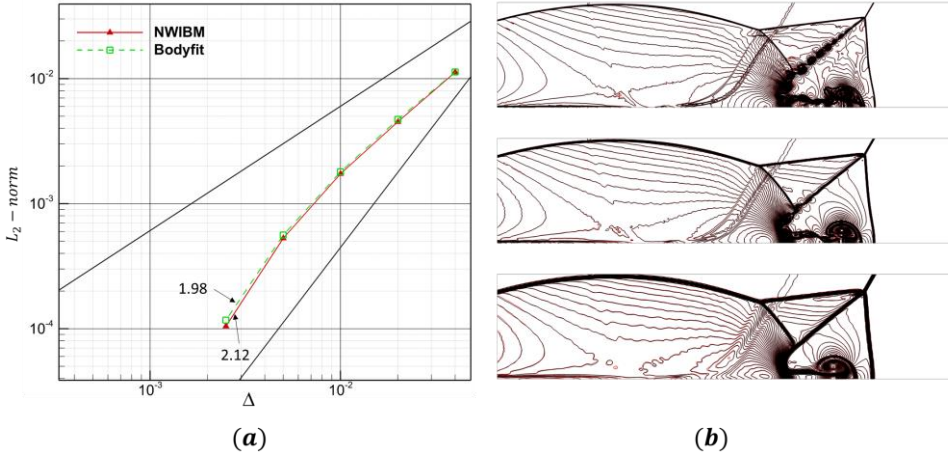
Figure 36. (a) Global order of accuracy comparison and density line contours by (b) NWIBM (black line) and Body fitted (red line) results

In order to analyze the global order of accuracy, NWIBM has been applied to the body-fitted configuration in the same manner of body-fitted grid in Fig. 30 (b). In this case, conventional IDW becomes equivalent to the body-fitted method. In Fig. 35, density plots using NWIBM and conventional body fitted method with respect to grid sizes from $\Delta = 0.00125$ to $\Delta = 0.04$ are shown and its global order of accuracy is plotted in Fig. 36 (a).
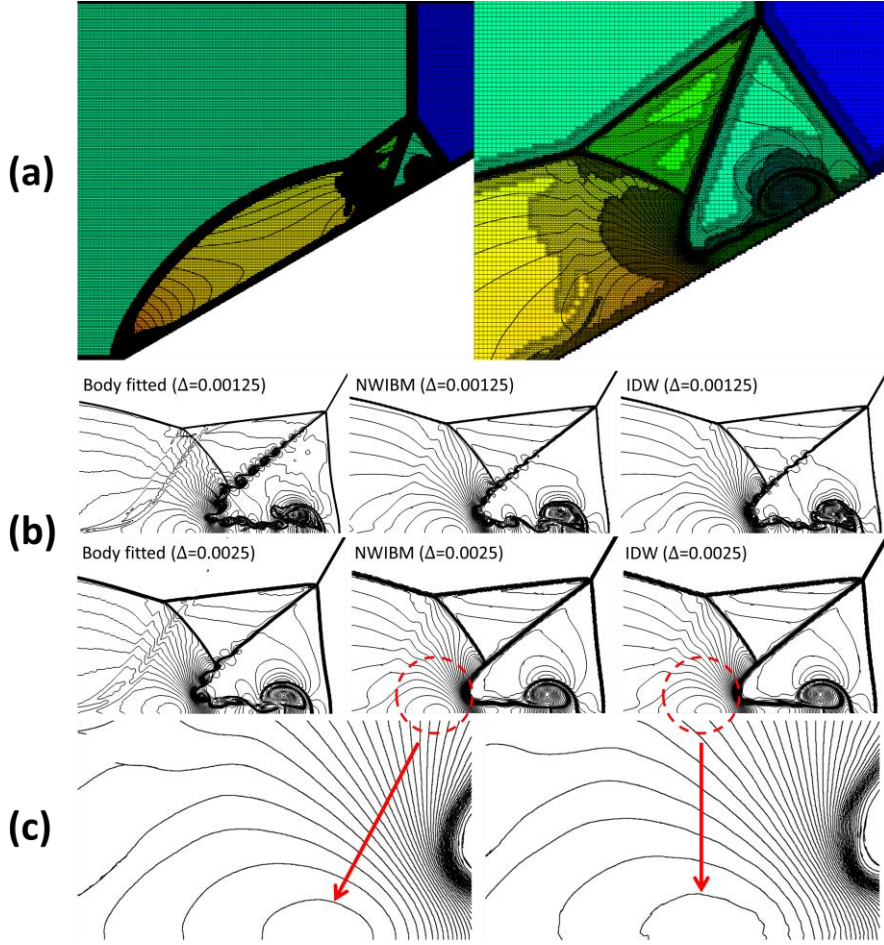
Figure 37. (a) Global clustering of AMR $t = 0.2$; (b) Comparison of body-fitted method using body-fitted configuration, NWIBM and IDW with grid sizes of $\Delta = 0.00125$ and $\Delta = 0.0025$; (c) Enlarged figure near smoothly varying region for $\Delta = 0.0025$

It has been found that NWIBM in body-fitted configuration well matches with the body-fitted method qualitatively (Fig. 36 (b)), but the order of accuracy with respect to the finest grid ($\Delta = 0.00125$) using NWIBM is 2.12 which is higher than body fitted method (1.98). This enhanced accuracy can be attributed to the high-order extension in the smoothly varying region using nonlinear weighting process. An inherent inability to cluster grids in the vicinity of the immersed boundary is one of the major drawbacks of the IBM. The grid clustering near the immersed boundary is required to solve the flow physics near the solid boundaries more accurately. To

overcome this problem, IBM with local, manual or adaptive, mesh refinement technique is adopted, which requires powerful solver capability to solve the governing equation in locally refined grid. Hence, the present method is solved by using adaptive mesh refinement (AMR) in order to prove the applicability of NWIBM in AMR as well as the enhanced performance even in highly refined mesh. A fully threaded tree (FTT) data structure [61] is used to organize the adaptive meshes up to three levels. In Fig. 37 (a), global clustering of refined mesh at $t = 0.2$ is shown where the finest grid size is $\Delta = 0.00125$. In Fig. 37 (b), body-fitted method using body-fitted configuration, NWIBM and IDW are compared using the grid sizes of $\Delta = 0.00125$ and $\Delta = 0.0025$. It is interesting to find out that the results from body-fitted configuration shows more evident Kelvin-Helmholtz instability even in the coarse $(\Delta = 0.00125)$ grid set, compared to the immersed boundary configurations. Qualitative difference between NWIBM and IDW can be found in the smooth region in Fig. 37 (c), which shows reduced oscillations in NWIBM result even in AMR. This improvement can be found more clearly by the density plot along the ramp in Fig. 38.
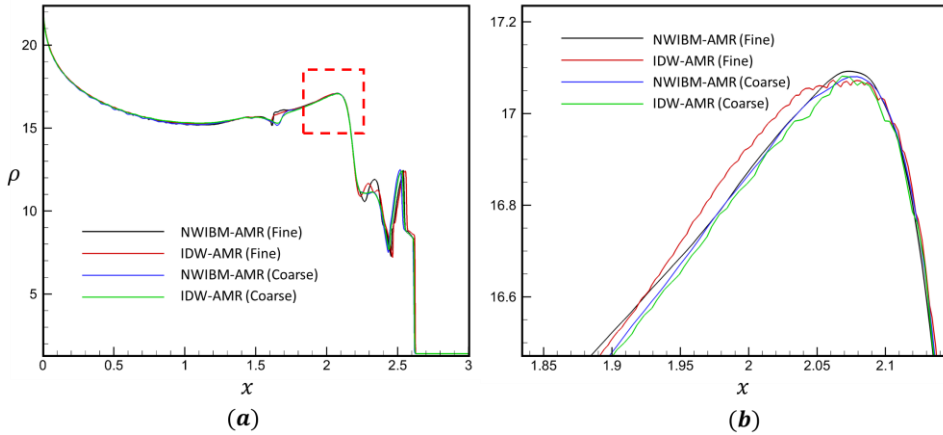

Figure 38. (a) Density along the ramp wall using AMR with NWIBM and IDW; (b) Enlarged figure near the smoothly varying region

4.3 Three-dimensional Extension

The interaction of the shock wave with a sphere results in complex shock–boundary interaction. It involves incident shock, direct or inverse Mach reflections, transmitted and reflected shocks, triple points, and slip lines [13]. The shock–boundary interaction and its wake region have both smooth and discontinuous flow near the immersed boundary; therefore, it is one of the best examples to showcase switching between high and low order during shock-wave interaction with a sphere. The interaction of the shock wave with a sphere was investigated to demonstrate the extension of the proposed method to 3D and the capability of the proposed NWIBM.

In the experimental studies carried out by Tanno et al. [62], the interaction of a planar shock wave of Mach number (Ms) 1.22 with an 80-mm-diameter sphere was selected, and the flow field was initialized based on Rankine–Hugoniot shock relations. Although the experimental results are not inviscid flow, because the flow is supersonic, the effect of convection is dominant. Therefore, the numerical results of the inviscid flow were quantitatively compared with the experimental results at four different times. For the diameter of the sphere, D, the numerical investigation was performed in two grids, i.e., $\Delta = D/100$ and $\Delta = D/200$. The numerical domain size was kept large enough that the boundary condition provided at different boundaries did not interact with complex flow features of the interaction of the shock wave with a sphere at four experimentally measured result times (92 μs, 140 μs, 296 μs, and 380 μs). As in the experimental measurement, after the incident shock wave reaches the sphere front side, the measurement time starts, i.e., at 0 μs, the incident shock is at the frontal stagnation point.
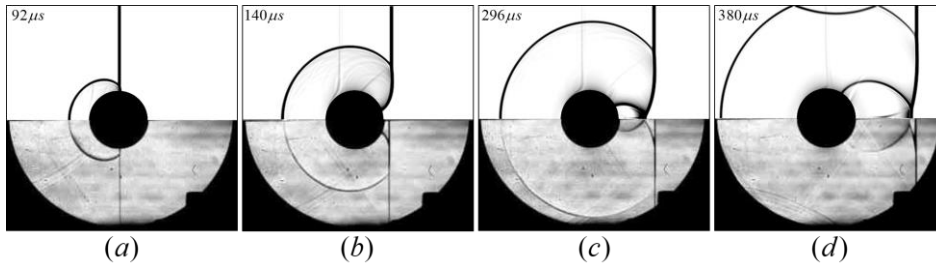

Figure 39. Comparison of numerical shadow graph (top half) and experimental shadow graph [62] (bottom half) at different times

In addition to the comparison with experimental results, the proposed NWIBM results were compared with those of the IDW method. In the numerical simulation, the transition to Mach reflection time appeared, and the place of observation matched well with the experimentally measured values. A qualitative comparison of numerical schlieren snapshots with the experimental results — see Figs. 39 (a)–(d) — shows that the complex flow features of the shock front, shock reflection, diffraction of the shock wave, ring shape formation from the gradually curved Mach stem, and its collision at the rear stagnation point are well captured by the proposed method. In addition, the quantitative comparison of the numerical and experimentally measured pressure at the midsection of the sphere shows that the pressure distribution follows a trend similar to the experimental results, as shown in Figs. 40 (a)–(d). The numerical result shows some deviation from the experimental results in some points at different times. It is difficult to quantify because of the uncertainty in experimental measurement. The details of the uncertainty in experimental measurement are discussed elsewhere [62].

Moreover, comparisons of nondimensional pressure at the sphere surface computed by the IDW method and NWIBM reveals that the NWIBM-computed pressure distribution is smooth and more accurate in the smooth region, as in Figs. 30 (a)–(d), and the pressure distribution at the discontinuous flow region closely matches the results of the IDW method — see Figs. 40 (a)–(b).

Further investigation of the computed nonlinear weighting reveals that, even in the shock region, the nonlinear weighting is assigned appropriately based on the flow field, i.e., the nonlinear weightings are different in strong and weak shock regions, as recognized by the multidimensional smoothness indicator. Fig. 31 demonstrates the transient nonlinear weighting during the interaction of a moving shock wave with a sphere. After the incident shock wave passes the equator of the sphere, the Mach stem becomes diffracted. The variations of the nonlinear weightings well reflect the physics of shock strength changes during diffraction. Owing to the ability of weightings to distinguish the smooth and continuous regions, the solution obtained from the present method was found to be more accurate and stable than that obtained by the conventional IBMs.
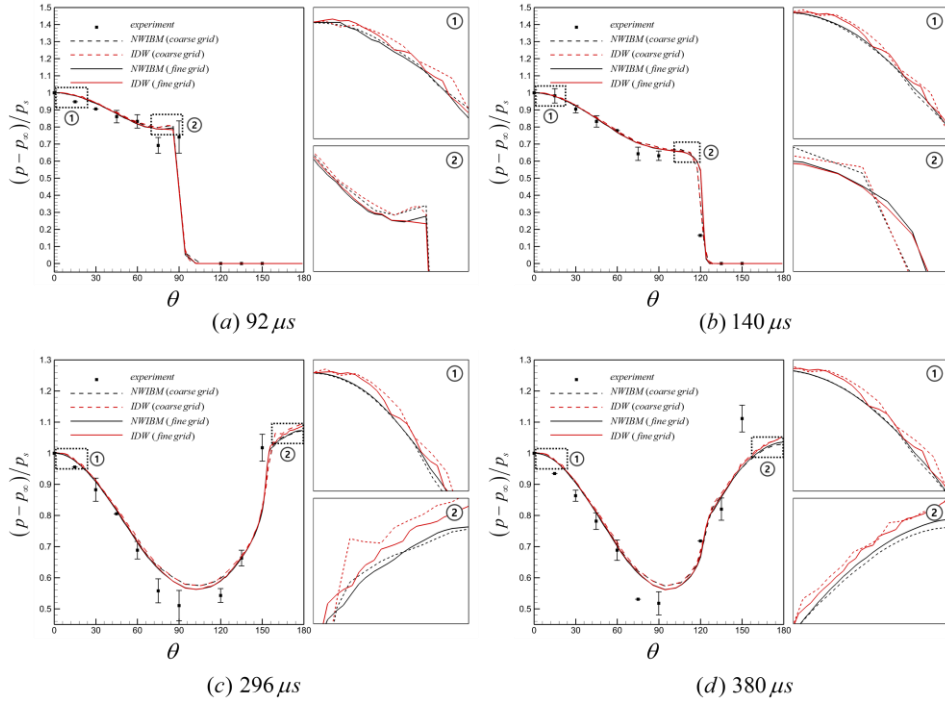
Figure 40. Comparison of numerically obtained nondimensional pressure with experimentally measured [62] results at sphere midsection at four different times
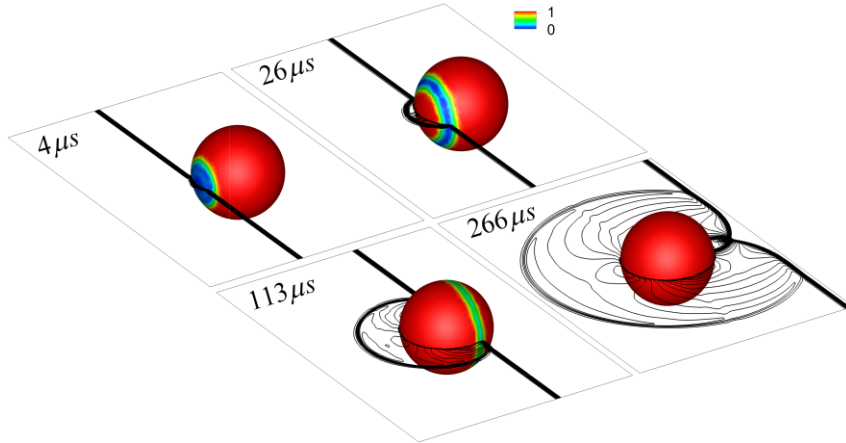

Figure 41. Demonstration of nonlinear weight change during shock-wave interaction with sphere at different nondimensional times.

4.4 Fluid-Structure Interaction

4.4.2 Cylinder lift-off problem

As part of the FSI test, the so-called cylinder liftoff problem was considered, which has frequently occurred in many studies since it was originally proposed [63]. In this problem, the rigid cylinder of a nondimensional diameter 0.1 and density 10.77 is initially centered at (0.15,0.05) on the floor of a two-dimensional channel with a size of 1×0.2. The domain is initialized by pressure 1 and density 1.4 with the initial shock $M_s = 3$ positioned at 0.08 from the left end. The top and bottom of the domains are rigid walls, the left boundary is set to the post-shock state, and an outflow boundary condition is used for the right boundary. The calculation grid included 1000×200 cells.

The positions of the mass center of the cylinder is listed in Table 4 for two time instants at t = 0.1641 and 0.30085 s after the lifted motion of the cylinder occurs because of the effect of moving shock waves. With respect to the grid resolution, the present results match well with the results of previous studies. Even though a slight discrepancy is found, which can be attributed to the spatial schemes or time integration method of dynamics, it is a quantitatively reasonable behavior of cylinder motions.
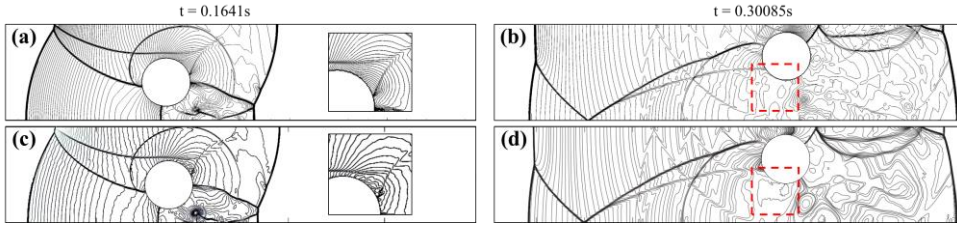
Figure 42. Pressure contours at two different time steps from NWIBM (a and b) and reference studies (c and d)

Qualitative comparisons with the pressure flow field of a recent study [64,65] where the conventional IDW interpolation is utilized for sharp-interface IBM are shown in Fig. 42. The present simulations agree well with the reference results in terms of overall flow patterns including vortex structures and incident and reflected shock waves. However, both reference results seem to produce slight oscillations near the circular cylinder. One possible reason for this spurious flow pattern is the

low-order interpolation of IBM, which results in numerical errors accrued as time goes by because the dissipation of the nonlinear flux scheme is less in the smoothly varying region. Another reason could be the interpolation error when freshly emerged cells occur, which magnifies the jump discontinuity.

Table 4. Positions (x, y) of the mass center of the cylinder

Grid size	t = 0.1641 s		t = 0.30085 s	
	x	y	x	y
1/250	0.3345	0.0750	0.6123	0.1322
1/500	0.3437	0.0762	0.6101	0.1305
1/1000	0.3449	0.0787	0.6137	0.1341
Reference 1 [64]	-	-	0.6269	0.1370
Reference 2 [65]	-	-	0.6173	0.1312

Meanwhile, the present result shows a nonoscillatory flow pattern near the cylinder in the enlarged inset of Fig. 42 (a) and (b) because NWIBM sustains high-order interpolation and jump-discontinuity treatment. This reduced oscillatory behavior proves the enhanced performance of the present method in addition to validation with previous studies.

4.4.2 Shock wave impacts on deforming panel
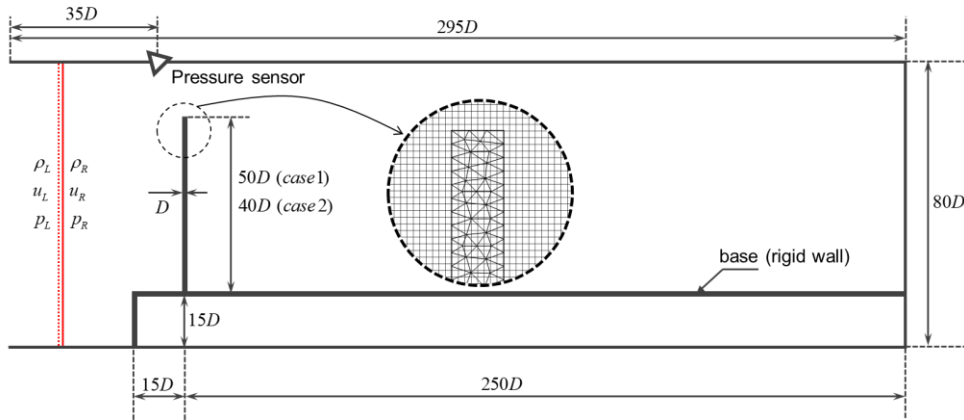
Figure 43. Numerical configuration and geometric dimensions for shock wave impact on deforming panel (inset is a schematic diagram of the structure element)

As an application of the present method, the fluid–structure interaction (FSI) problem was chosen to analyze the behavior induced by a moving shock wave of a cantilever panel. Based on a numerical and experimental study [66], the NWIBM was applied to FSI to solve this benchmark problem, and the result was compared with those of previous studies [66–68]. The experimental setup used for the numerical calculation is shown in Fig. 43 with a length scale normalized by the thickness of the panel (1 mm). Within a two-dimensional channel with a size of $295\text{mm}\times80\text{mm}$ discretized by $\Delta = 0.15$ mm, a steel panel composed of 1756 triangular structure elements is clamped to a rigid forward-facing base at the lower bottom. In this study, two lengths (50 and 40 mm) of steel panels (Young's modulus: $E_s = 220\,\text{GPa}$, density: $\rho_s = 7600\,\text{kg/m}^3$, Poisson's ratio: $\upsilon_s = 0.33$) clamped to a rigid forward-facing base at the lower end were considered. In the left inlet boundary, the moving shock with a Mach number of 1.21 in air at rest ($10^5\,\text{Pa}$ and 293K) was imposed with the postshock values formulated based on Rankine–Hugoniot shock relations. In the other boundary, including the cantilever beam and base, a Neumann wall boundary condition was applied. The computational grid was composed of four-level grid sets with respect to the smallest one.

A qualitative analysis of case 1 (0.05-m cantilever beam) was performed to validate the global flow field evolution by the present code. In Fig. 44, the numerical results using the NWIBM (on the right) are compared with the experimental visualizations (on the left) [66]. The results are shown from $t = 0\,\mu\text{s}$ in which the moving shock has already run over the beam, showing the initiation of the reflection and transmission of the incident shock wave as well as the bending of the beam to the downstream side. Because the shock wave undergoes the abrupt change of the area in the downstream from the region in between the beam and the top wall boundary, the normal shock wave transits to a cylindrical shock front. While this cylindrical wave moves forward, the vortex shedding starts at the right tip of the beam because of the roll-up of the slipstream ($t = 140\,\mu\text{s}$). The reflected wave on the base wall interacts with the vortices ($t = 280 - 700\,\mu\text{s}$), which induces unpredictably complex flow features. The spherically moving shock wave finally meets the right end wall, and it reflects back toward the upstream direction, which

64

induces the reverse bending of the beam ($t = 980 - 1560 \mu s$). The qualitative comparison of the flow evolution shows no evident discrepancy between the numerical simulation and the experiment except for experimental pictures at $t = 140 - 280 \mu s$ because of the flow leakage between the panel and the shock tube walls.
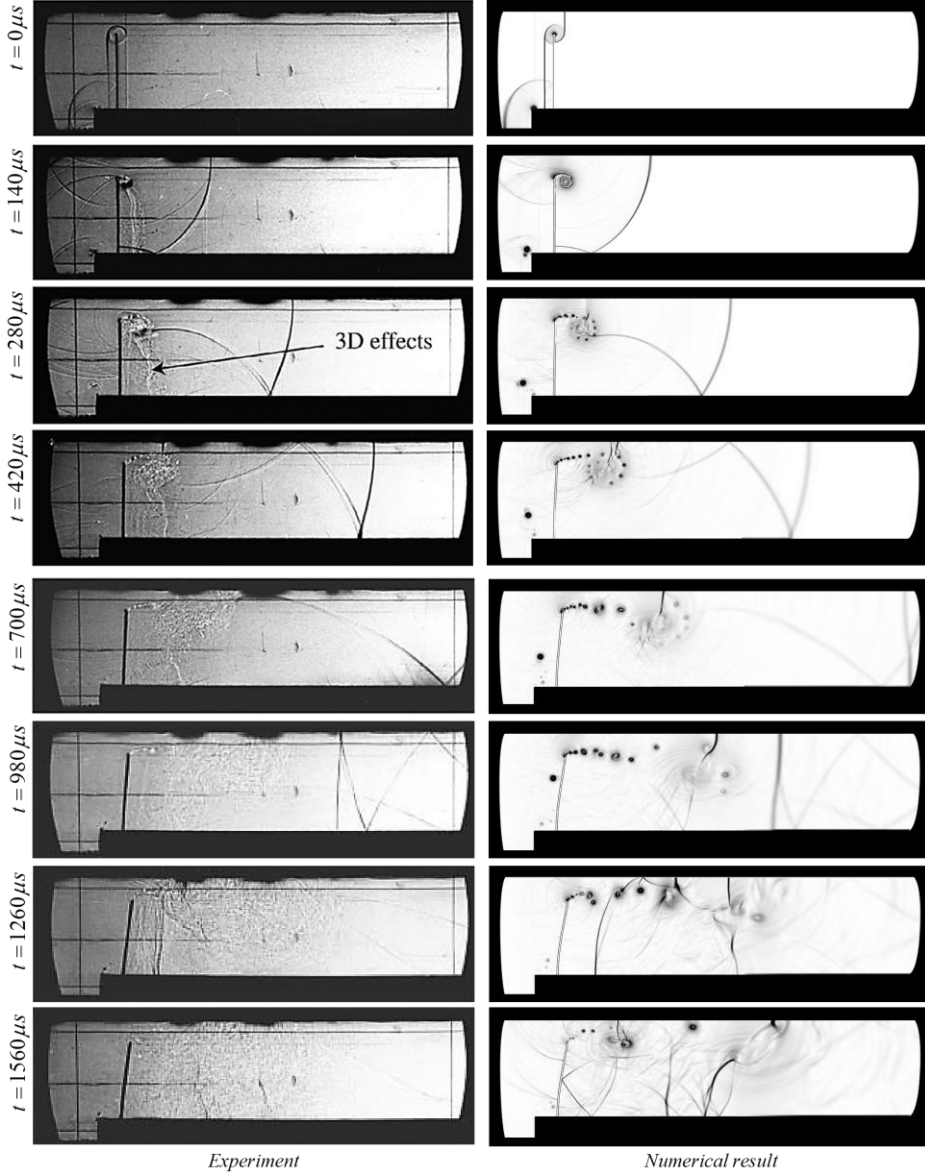
Figure 44. Qualitative comparison between experimental shadow graph (left) [66] and numerical schlieren (right) for case 1

To evaluate the numerical results quantitatively, the time evolutions of the tip displacement and the pressure variations at the sensor are plotted in Figs. 44 and 45 for cases 1 and 2, respectively. In addition to the experimental measurement, the numerical result [67] obtained by a cut-cell IBM is also compared. Because the cut-cell IBM basically employs the finite-volume approach, which is known to preserve mass conservation, this recent study was chosen as a pertinent reference to validate the present study.
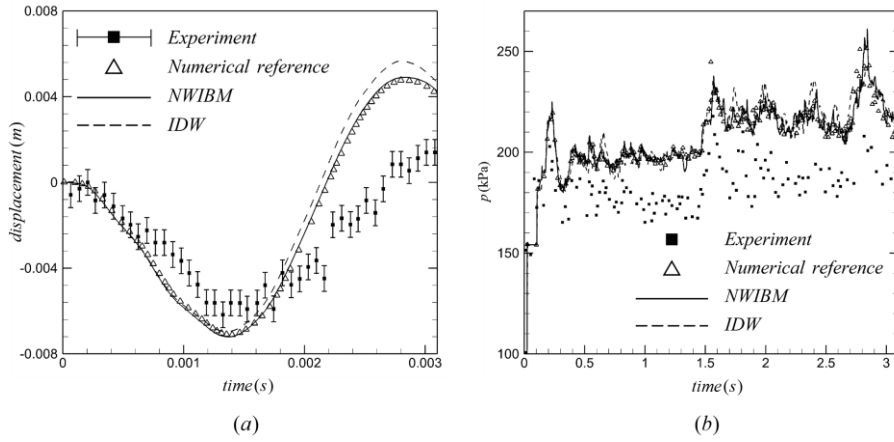
Figure 45. (a) Time evolutions of panel tip displacement and (b) pressure signals recorded at sensor position for case 1
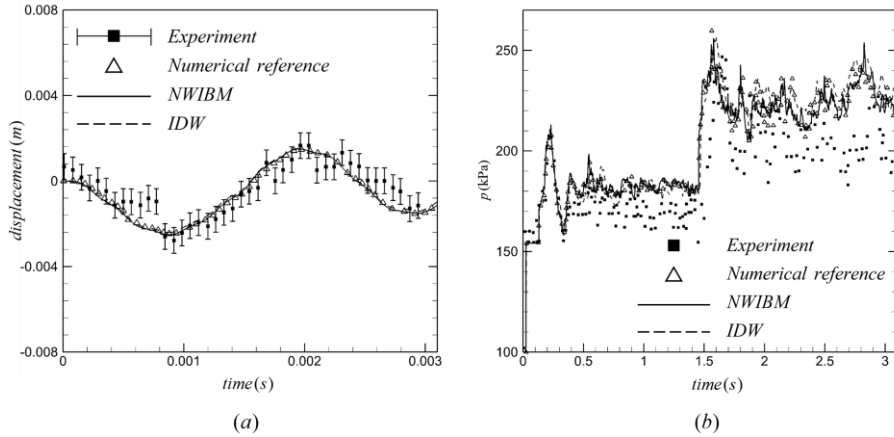
Figure 46. (a) Comparison of time evolutions of panel tip displacement and (b) pressure signals recorded at sensor position for case 2

For case 1 (Fig. 45), all the numerical simulations predict a similar behavior of the beam in terms of the maximum amplitude and frequency of the first period. The panel oscillation period obtained with the present method was 2.85 ms, which is close to the analytical period of 2.87 ms when considering the first eigenmode of a clamped plate subjected to an impulse load [66]. The experimental period was 3.8 ms. Even if the coarse grid case shows a slight deviation to the references after the first peak, the error was mitigated when a fine grid is used. This can be attributed to the inaccurate force imposition as the bending displacement becomes larger. In comparison with the experimental values, both the frequency and amplitude of the behavior differ from the numerical results. This deviation can be explained by the experimental error resulting from the small deformations of the base in the direct vicinity of the fixing point, which cause the uncertainties.

For case 2 in Fig. 46 (a), the numerical results of a shorter cantilever beam show excellent agreement with experimental data compared with case 1. Moreover, the coarse grid case shows less deviation from the other numerical results. This result explains more about the error in case 1 because the reduced stresses on the base diminishes the influence of the base on the panel motion and uncertainties in the experiment. Finally, the pressure signals recorded at $(35D, 80D)$ for both panel lengths are compared with the same numerical and experimental database (b) in Figs. 45 and 46. Again, all the numerical results are similar with respect to the time of arrival of pressure waves at the sensor and the pressure difference across the waves. While larger deviations are observed between numerical and experimental data for case 1, almost identical time evolutions up to t = 2 ms are observed for case 2.

In Fig. 47 (a), the enlarged figure of Fig. 35 (b) is used to compare the pressure signals obtained using NWIBM and the conventional IDW method. Except for the reasonable peaks caused by the reflections of shock waves, high-frequency peaks are generated in the IDW method because of the spurious waves that occur owing to jump discontinuity. Further, these features are shown in the density contours of Fig. 47 (b). The evident diminution of spurious oscillation was captured compared to the IDW method with a flow field disturbed by high-frequency waves; NWIBM produces a less oscillatory flow field. Hence, the nonlinear weighting process

67

including jump reduction results in more accurate and physical solutions in the overall flow field as well as near the immersed boundary.
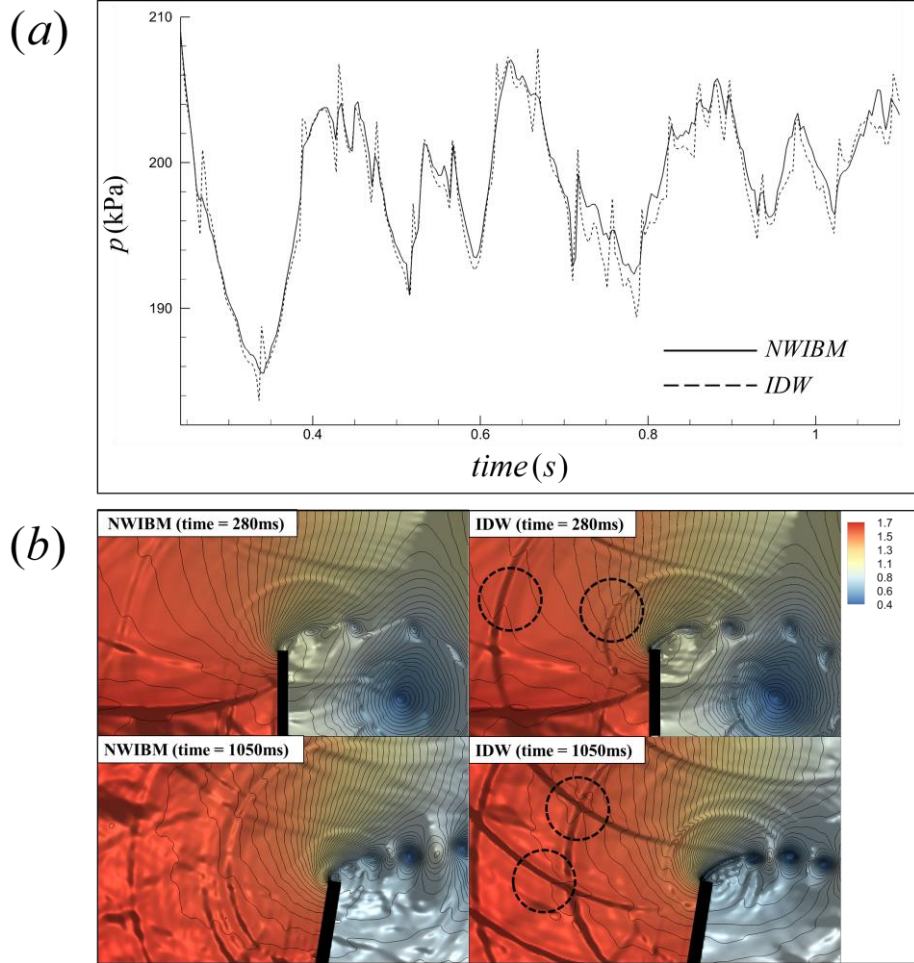
Figure 47. Comparison of NWIBM and IDW by (a) enlarged pressure signals recorded at sensor position and (b) enlarged density contours.

Chapter 5. Application problem

5.1 Flexible cylinder impinging on the wall

Contact between bodies is a very common problem in applied mechanics. This phenomenon is particularly relevant to the problems such as impinging of particles, vocal fold vibration, collision of supersonic projectiles and so on. In the current study, a penalty coefficient method [69] is used to model the contact in between solid wall and flexible cylinders as an extension of Chapter 4.4.2. in order to validate the applicability of NWIBM in contact problems. According to [69], the contact force is defined as

$$F^{contact} = \int \gamma g \nabla g dA \tag{81}$$

where γ, g and A are a penalty coefficient, penetration distance and the contact area, respectively. The integrated contact force ove the contact area creates the contact force that opposes penetration of cylinders.

As illustrated in Fig. 48, even if the contact problem were properly solved, there are one critical problem when applying the contact in IBM. When the distance between two bodies is very small, there is a chance that not sufficient number of cell is defined to reconstruct the ghost-cell values. In NWIBM, it is readily handled by interpolation of the ghost cell values using the values and derivatives at BI point obtained in the previous time steps.

t^n: **Before contact** t^{n+1}: **After contact**
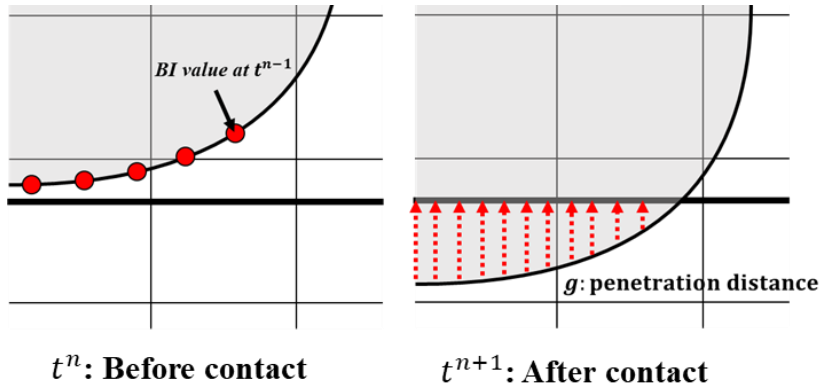
Figure 48. Before contact occurs using NWIBM (left) and after contact occurs using penetration algorithm (right)

In Fig. 49 (a), numerical results of cylinder trajectories with three different Young's modulus including rigid body case are shown. It can be found that the overall behavior of cylinders differs as the flexibility changes. Compared to rigid case which shows perfectly elastic collision, the other cases show nonlinear behavior with delayed reflections. Moreover, there is a critical point when the behavior of lift-off itself totally changes when the Young's modulus becomes lower than 1kPa. These characteristics could be quantitatively compared in density contour in Fig. 49. (b) where the reflecting position differs.
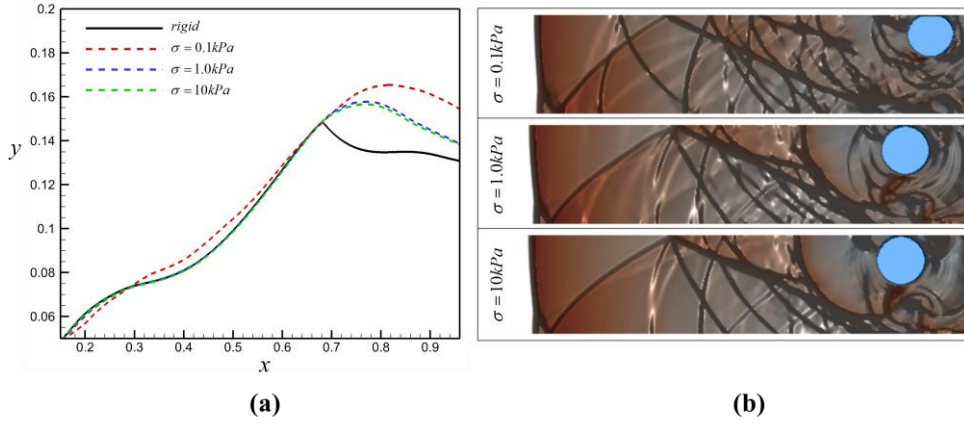
Figure 49. (a) Cylinder trajectories with respect to Young's modulus and (b) density contours of cylinder when it reflects off the wall.

5.2 Shock-flame interaction in channel with flexible obstacles

5.2.1 Evolution of detonation formation

In this chapter, currently developed NWIBM is applied to reactive flow problem with fluid-structure interaction. Before the analysis, complex flow phenomena including the validation of the reactive Navier–Stokes equations via the detonation formation problem [70] have been discussed. The formulations of reactive Navier-Stokes equations including models for chemical reactions with energy release can be written by changing Eq. (1) to

$$\rho_t + \nabla \cdot \rho \boldsymbol{u} = 0$$
$$(\rho \boldsymbol{u})_t + \nabla \cdot (\rho \boldsymbol{u} \boldsymbol{u}) + \nabla p + \nabla \cdot \boldsymbol{\tau} = 0$$
$$(\rho e)_t + \nabla \cdot \big(\boldsymbol{u}(\rho e + p) \big) + \nabla \cdot (K \nabla T) + \nabla \cdot (\boldsymbol{u} \cdot \boldsymbol{\tau}) = q \dot{\omega} \tag{82}$$
$$(\rho Y)_t + \nabla \cdot (\rho Y \, \mathbf{U}) + \nabla \cdot (\rho D \nabla Y) = -\dot{\omega}$$

where the variables of chemical reaction, Y is the mass fraction of a reactant, q is the chemical energy release, and $\dot{\omega}$ is a one-step reaction model described by the first-order Arrhenius kinetics, which is defined as

$$\dot{\omega} = \frac{dY}{dt} = A\rho Y e^{-E_a/RT}, \tag{83}$$

where A is the pre-exponential factor and E_a is the activation energy. In this study, an ideal gas assumption is taken for the equation of state as $p = \rho RT / M$ with the universal gas constant R and molecular weight M.

Within a rectangular domain with dimensions $[0,150] \times [-0.5, 0.5]$, the reactive gas is at rest in thermal equilibrium with the nondimensional initial condition

$$\rho_0 = Y_0 = T_0 = 1, \quad u_0 = v_0 = 0 \tag{84}$$

and the specific heat ratio of $\gamma = 1.4$. The nondimensional pre-exponential factor, chemical energy release, and activation energy are defined as, $A = 15$, $q = 15$, and $E_a = 13.79$, respectively. In the left and right boundaries, the wall boundary condition is imposed while the upper and lower boundaries are set as periodic boundaries.

In the initial few moments, the spatial distribution of the transient thermal power source term in $1 < x \le 5$,

$$\dot{W} = 2.1\{\tanh[5(t - 0.5)] - \tanh[5(t - 10)]\} \tag{85}$$

is added on the right-hand side of Eq. (1), which reproduces the flame and shock propagation.

The results of the chemical heat release rate,

$$\dot{Q} = \int_\Omega \dot{\omega} q \, d\Omega, \tag{86}$$

are shown in Fig. 50 (a) with respect to four grid sizes with $\Delta = (0.0195, 0.039, 0.078, 0.156)$ and compared with the reference study [70]. The transient heat release behavior of the current simulations with the finest grid size shows good agreement with the reference result. Two noticeable peaks of the heat release rate correspond to power addition by the source term and the overdriven detonation, respectively. The prolonged peak after the overdriven detonation is caused by the consumption of a localized pocket of unburned fuel.

After the overdriven detonation, it shows relaxation to a steady-state detonation. The grid refinement study shows convergence when the grid size is $\Delta = 0.039$; however, even in the most coarse grid case ($\Delta = 0.156$), the peak heat release time lies within 5% of the reference value. This implies that the global structure of the DDT process is a weak function of numerical resolution because the smallest-scale structures contain very little reactants and are the sources of a tiny amount of energy release. To evaluate the characteristics of complex flow and combustion phenomena, the space-time diagram at $y = 0$ is plotted in Fig. 50 (a) and (b). The initial spark caused by thermal power deposition creates two shock waves that travel in both the upstream and downstream directions. In Fig. 50 (a), the lead shock wave that propagates downstream induces the chemical reaction by heating the inert gas, thereby leaving the material interface behind around $t > 5$. Meanwhile, the upstream propagated shock wave reflects back at the left wall and runs into the material interface where both transmission and reflection occur. In Fig. 50 (b), it is shown that the transmitted shock wave coalesces with the lead shock, which in turn formulates the hot spot. After the hot spot formulation, an induction zone occurs, and the chemical heat release starts to increase. It can be found that a localized explosion occurs where the reflected shock trespasses the induction zone, which subsequently creates an accelerating reaction. Overdriven detonation eventually occurs $t = 21$ when the accelerating reaction front reaches the lead shock by introducing an immediate rapid reaction on the acoustic timescale.

72

From the series of complex flow behaviors, it is notable that multiple shock reflections subsequently heat the temperature, which becomes the major source of deflagration to detonation transition.
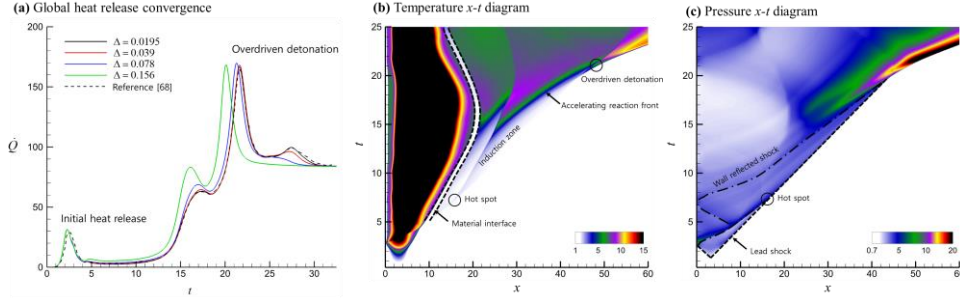
Figure 50. (a) Chemical heat release rate with respect to four grid sizes, and space-time diagram for (b) temperature and (c) pressure

5.2.2 Problem description

Let us consider a two-dimensional channel with evenly spaced obstacles, as shown in Fig. 51, with a characteristic length D = 10 mm and grid size 0.1 mm where the reaction zone thickness is resolved. Initially, the channel is filled with a stoichiometric inert ethylene–air mixture and burnt circular shaped flame. To facilitate the DDT process, a moving shock wave with $M_s = 3.0$ is modeled to function as an ignition mode. The initial flame and shock are located at 20 and 5 mm from the left boundary, respectively. Inflow and outflow boundary conditions are imposed on the left and right boundaries. A slip-wall boundary condition is imposed on the upper and lower boundaries, except for the obstacles where a no-slip wall boundary is applied to separately consider the boundary layer effects caused by the obstacles.
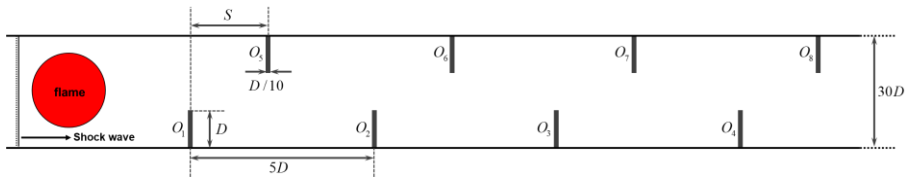
Figure 51. Schematic of straight tube with eight obstacles, initial flame and shock wave.

Because there are neither direct experimental data nor reliable detailed chemical one-step reaction models for the ethylene–air mixture, the input parameters of the current reactive system are calculated by the theoretical equations based on adiabatic flame temperature and CJ detonation velocity [71]. The initial flow, stoichiometric, and structural properties for the numerical simulations are described in Table 5.

Table 5 Input parameters and properties of stoichiometric ethylene-air mixture.

| Input parameters		
ρ_0	$1.58\times10^{-1}\,\mathrm{kg/m^3}$	Initial density
p_0	$1.33\times10^4\,\mathrm{J/m^3}$	Initial pressure
T_0	293K	Initial temperature
Y_0	1	Initial composition
γ	1.15	Specific heat ratio
M	29	Molecular weight
E_a	$29.3RT_0$	Activation energy
A	$3.2\times10^8\,\mathrm{m^3/kg\cdot s}$	Pre-exponential factor
q	$35RT_0/M$	Chemical energy release
$\nu_0=\mu_0=D_0$	$1.3\times10^{-6}\,(g/s\cdot\mathrm{cm}\cdot\mathrm{K}^{0.7})$	Transport constants
Output parameters		
T_b	2340K	Adiabatic flame temperature
ρ_b	$1.98\times10^{-2}\,\mathrm{kg/m^3}$	Adiabatic flame density
T_s	1500K	Postshock detonation temperature
ρ_s	$1.15\,\mathrm{kg/m^3}$	Postshock detonation density
D_{CJ}	$1870\,\mathrm{m/s}$	CJ detonation velocity
Structure material properties for flexible obstacles		
YM	68GPa and 6.8GPa	Young's modulus
ν_s	0.33	Poisson's ratio
ρ_s	2700kg/m³	Material density

5.2.3 Effects of geometrical configuration

First, the effect of the geometrical configuration is considered with respect to detonation transition and energy release. As an example, the process of detonation transition is shown for two differently staggered obstacle configurations (case 2 and case 3) in Figs. 52 and 53. In each figure, the temperature contours and enlarged pressure contour at the time between detonations occur to capture the hot spot formation. In both cases, the first detonation seems to occur when the flame accelerated at the first obstacle (O_1) impact on the second obstacle (O_5). In the pressure contours, the hot spot can be found with the CJ detonation pressure at O_5.
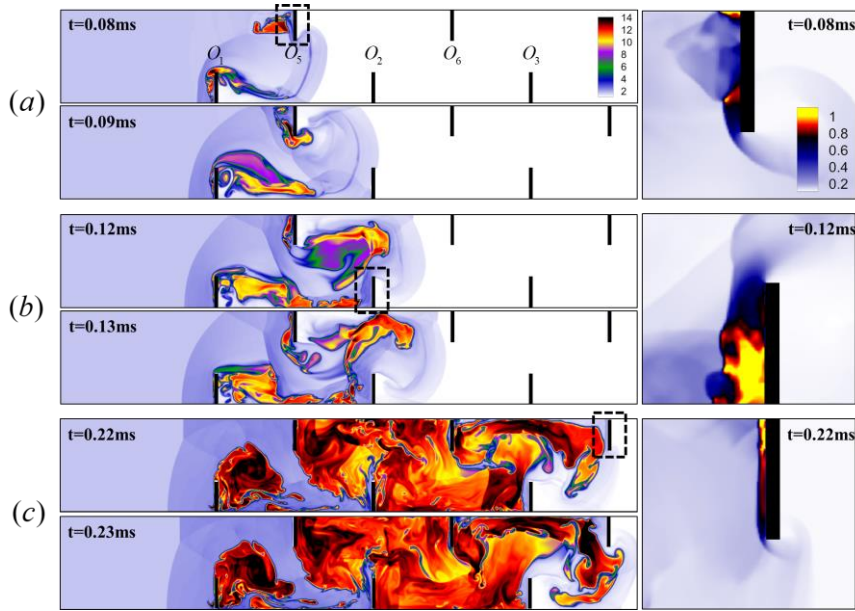
Figure 52. Temperature (left) and pressure (right) under shock-flame interaction to detonation transition for case 2.

In the other time sequences, similar characteristics where an abrupt rise in pressure induces hot spots are shown, which results in local detonation transition. The detonation seems weaker when the lower and upper obstacles are aligned as in case 3. This can be attributed to the blockage effect that keeps the shock wave from propagating and the reactant from entering the chemical reaction. The temperature contours (c) in Figs. 52 and 53 clearly show the results of the blockage effect because

the temperature in case 3 is delayed as the flame propagates through the obstacles compared to case 2.
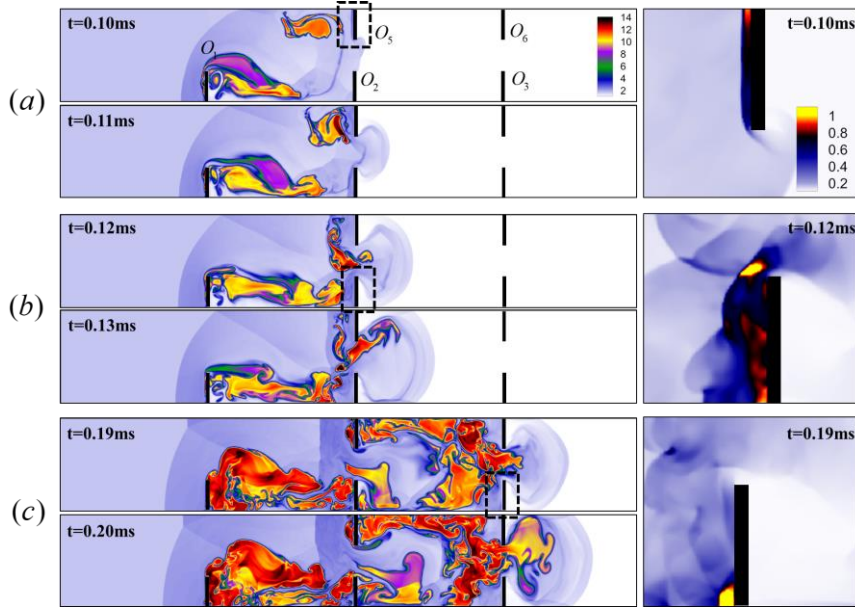
Figure 53. Temperature (left) and pressure (right) under shock-flame interaction to detonation transition for case 3.

A quantitative comparison of each obstacle case is performed by the energy release rates in Fig. 54. In a short, smooth channel without a boundary effect, a flame ignited by a shock hardly transits to a detonation for an ethylene–air mixture. However, DDT always occurs when the pressure is sufficiently high to reach the CJ detonation point by the obstacles.

Up to 0.15 ms, both aligned (case 1) and staggered (case 2) cases show similar energy increments because the first upper and lower obstacles affect the acceleration of the flame propagation and energy release rate. Meanwhile, the fully staggered (case 3) case shows slower DDT because the first obstacle in the upper wall is not effective. After the flame passes the first obstacles, case 2 reaches the local maximum energy release rate around 0.2 ms while the other cases reach at 0.25 ms. Overdriven detonation is first captured at 0.3 ms for case 2, which does not occur in case 1 until 0.5 ms. For case 3, overdriven detonation occurs after 0.3 ms when the last upper and lower obstacle changes from aligned to staggered. The maximum

energy release rate is found in case 2 compared to the other cases that make smaller areas for the flame to propagate. These results imply that proper blockage in the propagation direction accelerates DDT.
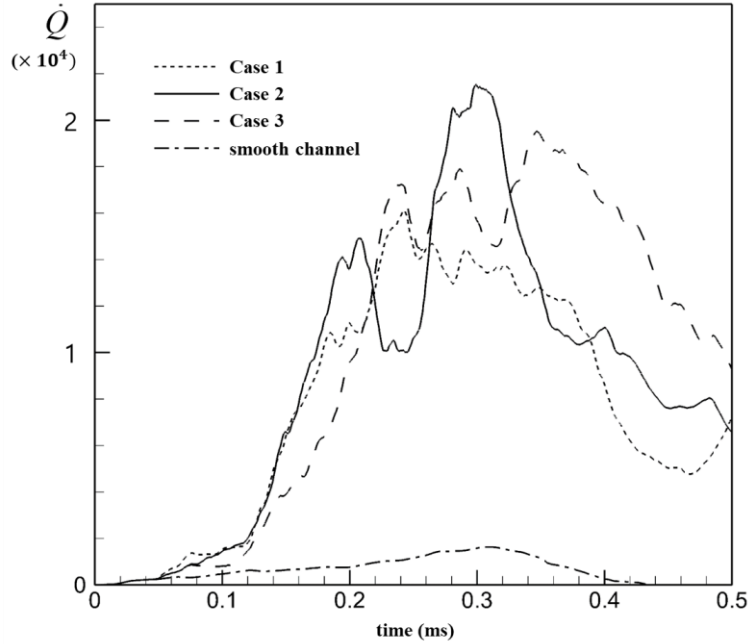
Figure 54. Chemical heat release rate for each case of the straight tube with and without rigid obstacles.

5.2.4 Flow behavior based on flexibility

Now the effects of FSI is considered in addition to the previously discussed rigid-body analysis. Time sequences of temperature (left) and density gradient magnitude (right) for case 2 are depicted in Figs. 55 to 58. In each figure, the obstacle is rigid (a), flexible with $YM = 68$ GPa (b), and highly flexible with $YM = 6.8$ GPa (c); the other conditions remain the same as those listed in Section 5.3.1. In addition, these qualitative results were compared with the pressure histories at four probe locations and the chemical heat release rate shown in Fig. 59.
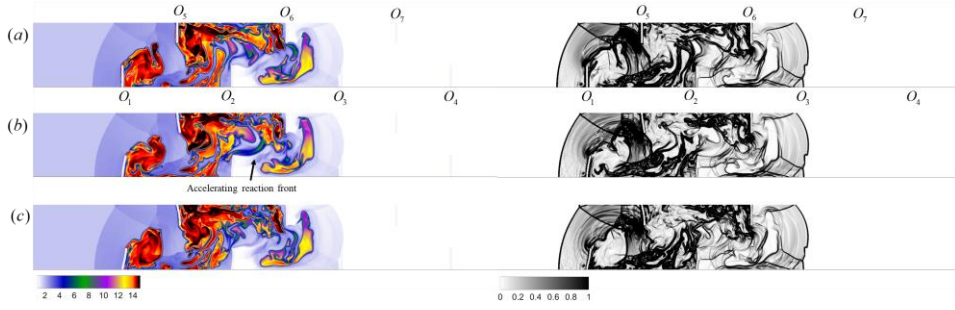
Figure 55. Temperature (left) and density gradient magnitude (right) under shock-flame interaction in straight tube with (a) rigid, (b) flexible and (c) highly-flexible obstacles at t = 0.17 ms.

In Fig. 55 (at t = 0.17 ms,) the fast flame propagation occurs after the first weak detonation near O_1 caused by the shock–flame interaction. In the flexible obstacle case, it is observed that the accelerating reaction front near O_2 is more evident compared to the rigid case, which can be attributed to the bending of O_2 and O_5 that widens the effective area in the axial direction. Further, in the highly flexible obstacle case, it was found that the reversely bent O_2 trapped the flame, thereby resulting in weak flame propagation. The effect of the structural deformation is shown in Fig. 59.
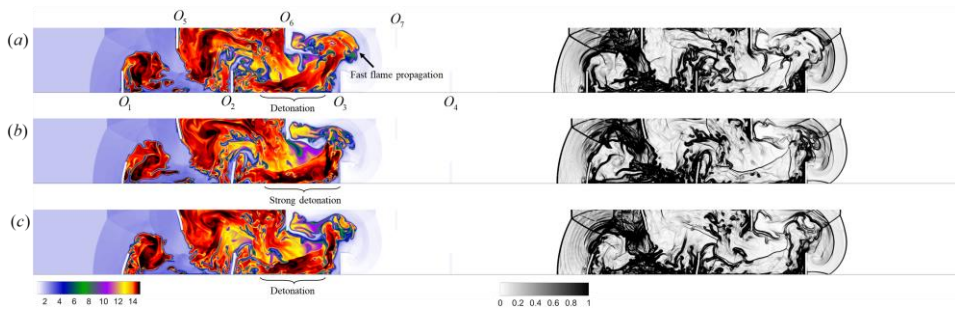
Figure 56. Temperature (left) and density gradient magnitude (right) under shock-flame interaction in straight tube with (a) rigid, (b) flexible, and (c) highly-flexible obstacles at t = 0.2 ms.

78

This accelerating reaction front in a flexible obstacle leads to stronger detonation (Fig. 56) and a large emission of energy with faster reaction at t = 0.2 ms, where energy release is locally maximized (Fig. 59). Further, it is observed that flexible and highly flexible obstacles O_2 delay flame propagation in the region above O_3 compared to the rigid case. The delayed shock resulted in a more complex and focused density region in the right figures of Fig. 56 (b) and (c).
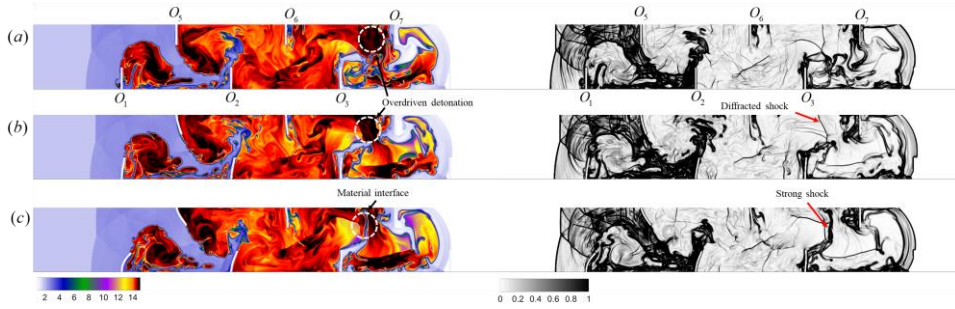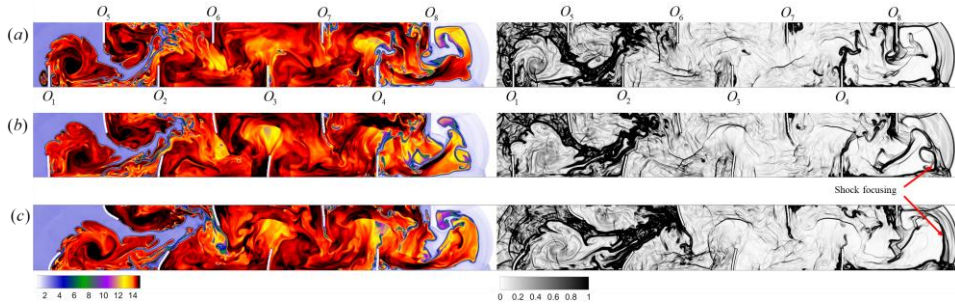

Figure 57. Temperature (left) and density gradient magnitude (right) under shock-flame interaction in straight tube with (a) rigid, (b) flexible, and (c) highly-flexible obstacles at t = 0.25 ms.

As the flame propagates further, the overdriven detonation occurs around t = 0.25 ms. In Fig. 57, all cases show a strong shock wave toward the bottom wall after the detonation occurs behind O_7. However, the chemical reaction and detonation seem to occur less in the highly flexible case, which can be attributed to the formation of the material interface by a chain reaction of strong shock, as marked in Fig. 57 (c). This material interface hinders the induction of energy and the feeding of the fuel that results in less, but sustaining energy release rate as shown in Fig. 59 (b). Meanwhile, the flexible obstacle case showed the maximum over detonation. Thus, it can be inferred that elastically deforming obstacles could accelerate or decelerate the DDT process. In terms of shock wave propagation, the deformation of obstacles forms a more complex flow field and strong diffracted shock (Fig. 57).

Figure 58. Temperature (left) and density gradient magnitude (right) under shock-flame interaction in straight tube with (a) rigid, (b) flexible, and (c) highly-flexible obstacles at t = 0.17 ms.

In the last snapshot (Fig. 58), the effects of deforming structures on shock wave propagation can be found. Because of the increased multiple reflections by obstacles, shock focusing occurs after the flame exits O_8, which results in a strong shock wave. It is evident from Fig. 59 (a) that the pressure magnitude of the flexible obstacle cases increases at P4 compared to the rigid case. Comparing the energy release rate in Fig. 59 (b) with Fig. 54, it is interesting to find that the effect of flexibility is as much as that of the geometrical configuration changes in the DDT process.
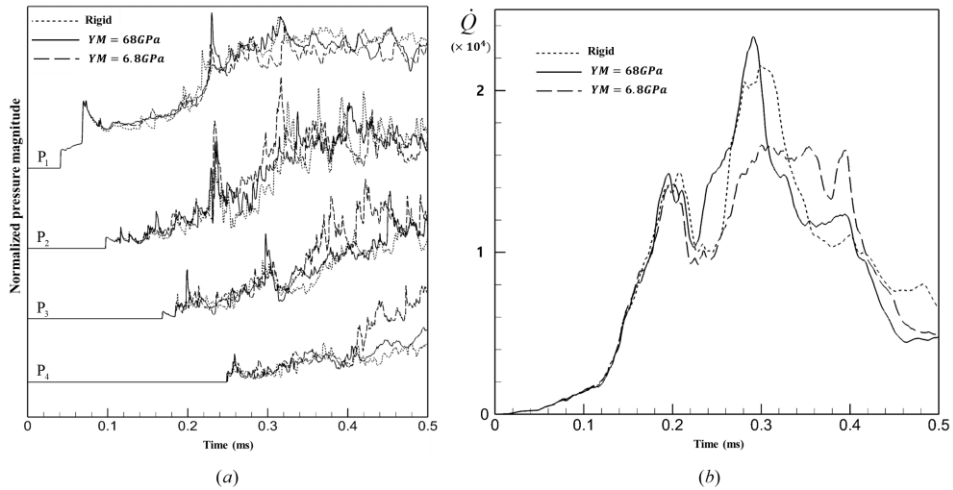

Figure 59. (a) Normalized pressure magnitude histories at four probe locations and (b) chemical heat release rates

In addition, the space-time diagram has been analyzed to investigate the effects of flexibility at the bottom wall. In Fig. 60, the temperature variation caused by the detonation shows a noticeable difference at the bottom wall as well. In the $O_1 - O_2$ region, all three cases show similar behavior up to 0.14 ms. Compared to the other two cases, the temperature increase is more evident in the flexible case in the $O_1 - O_2$ region, which affects the accelerating reaction front, as shown in Fig. 55 (a). In the $O_2 - O_3$ region, where the first detonation wave reaches approximately 0.18 ms, it is found that the rigid case shows a lower temperature near O_3 compared to the flexible cases. It can be inferred that the reduced blockage by flexible obstacles accelerated flame propagation toward the bottom wall.

Finally, the transient temperature change due to the overdriven detonation can be found in the $O_3 - O_4$ region. The material interface is clearly observed in the highly flexible case, while the high-temperature region caused by the detonation wave is found, especially in the flexible case. From the quantitative and qualitative comparison with respect to the flexibility of obstacles, it was found that not only the overall behavior, but also detailed features of the flame-shock interaction change.
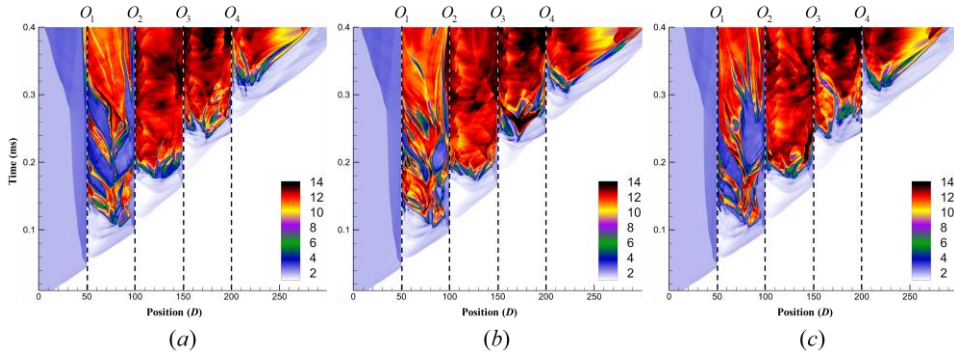
Figure 60 Space–time diagram of the temperature at the bottom wall for (a) rigid, (b) flexible, and (c) highly flexible obstacle case.

Chapter 6. Concluding Remarks

A new ghost-cell IBM, NWIBM, was developed by combining the conventional low-order and high-order polynomial reconstructions. To enforce the boundary conditions, two different polynomials are combined during the ghost-cell value estimation by the nonlinear weighting process. The nonlinear weightings are assigned based on a smoothness indicator that has been designed in a multidimensional way using spatial derivatives obtained from the high polynomial to evaluate the flow discontinuity. Because of the nonlinear weightings that cause the immersed boundary reconstruction to utilize adaptively the high-order and low-order interpolations, the flows near the discontinuous and smooth regions show stable and accurate behavior, respectively. When the high-order stencils are spread in the smoothly varying region, weightings from the high-order polynomials become dominant, while the weightings from the low-order polynomials become negligible. Such a process operates the other way around in the discontinuous region, which is attributed to a more stable and accurate numerical solution.

In addition, flow field reconstruction is implemented where a smooth condition near the boundary is determined by nonlinear weighting process. It has been found that the jump-discontinuity is minimized, which facilitates a high-order stable solution for compressible flow simulation, not previously explored actively in the IBM research field. The fundamental idea is the correlation between ghost and fluid fields that makes the function across the immersed boundary close to the analytic function. It is quite notable that the reduced jump-discontinuity induces less spurious waves and enhances stability of the solution. The magnitude of the jump-correction term, the major source of the jump-discontinuity, has been diminished when the present method is applied.

The performance of the proposed method was investigated using various numerical test problems. The numerical results reveal that the NWIBM is less oscillatory than conventional low-order IBMs in a compressible flow in cylinder, sphere, shock-obstacle interaction cases including fluid-structure interaction problems, which validates the applicability of the proposed method in fluid–structure interaction problems.

Two engineering application problems were solved as an application of NWIBM with FSI. Firstly, flexible cylinder lift-off with collision was considered. It was found that the reflection of cylinders after collision differs as well as there are critical point the behavior of lift-off itself totally changes with respect to the flexibility of cylinders.

In addition, the present NWIBM was applied to investigate the effects of the structure response on the deflagration to detonation transition. Compared to previous studies that addressed the effects of the size or shape of the obstacles in the channel, the current study highlighted the importance of FSI in deflagration to detonation transition in that the transient change of structures could induce the formation of different positions of the hot spot and detonation and the overall flow patterns. In addition to the current DDT applications, the present method is expected to be utilized in other research involving compressible flow that requires stable and accurate imposition of boundary conditions.

However, there are still limitations of the current algorithm. One is the efficiency issue due to the introduction of additional complexity of algorithm in calculating the nonlinear weightings. Even if it has been found that the efficiency becomes negligible compared to flux calculation and time integration when the number of grid increases, it is still problematic that computational cost is acceptable in FSI case which calculate the IBM subroutine iteratively. Another issue has to do with the smoothness indicator in nonlinear weighting calculation. Since the smoothness indicator is found spatially, not directionally like conventional WENO schemes, it is possible to locate discontinuous region more conservatively. Lastly, no optimal value of linear weighting for general problems are proven mathematically in this study. Thus, the order of accuracy can be hampered by using low-order reconstruction in not discontinuous region.

Despite above issues not dealt with in this study, the proposed algorithm based on nonlinear weighting and jump-discontinuity reduction processes is expected to be effective in various engineering problems that requires stable and accurate solutions in compressible flow.

References

[1]   C.S. Peskin, Flow patterns around heart valves: A numerical method, J.
        Comput. Phys. 10 (1972) 252–271. https://doi.org/10.1016/0021-
        9991(72)90065-4.

[2]   F. Sotiropoulos, X. Yang, Immersed boundary methods for simulating fluid-
        structure interaction, Prog. Aerosp. Sci. 65 (2014) 1–21.
        https://doi.org/10.1016/j.paerosci.2013.09.003.

[3]   C.S. Peskin, Flow patterns around heart valves: A numerical method, J.
        Comput. Phys. (1972). https://doi.org/10.1016/0021-9991(72)90065-4.

[4]   L. Zhu, C.S. Peskin, Simulation of a flapping flexible filament in a flowing
        soap film by the immersed boundary method, J. Comput. Phys. (2002).
        https://doi.org/10.1006/jcph.2002.7066.

[5]   J.M. Stockie, B.T.R. Wetton, Stability analysis for the immersed fiber
        problem, SIAM J. Appl. Math. (1995).
        https://doi.org/10.1137/S0036139994267018.

[6]   M.C. Lai, C.S. Peskin, An immersed boundary method with formal second-
        order accuracy and reduced numerical viscosity, J. Comput. Phys. (2000).
        https://doi.org/10.1006/jcph.2000.6483.

[7]   M. Uhlmann, An immersed boundary method with direct forcing for the
        simulation of particulate flows, J. Comput. Phys. 209 (2005) 448–476.
        https://doi.org/10.1016/j.jcp.2005.03.017.

[8]   D. Hartmann, M. Meinke, W. Schröder, A strictly conservative Cartesian
        cut-cell method for compressible viscous flows on adaptive grids, Comput.
        Methods Appl. Mech. Eng. 200 (2011) 1038–1052.
        https://doi.org/10.1016/j.cma.2010.05.015.

[9]   M. Meinke, L. Schneiders, C. Günther, W. Schröder, A cut-cell method for
        sharp moving boundaries in Cartesian grids, Comput. Fluids. 85 (2013)
        135–142. https://doi.org/10.1016/j.compfluid.2012.11.010.

[10]   L. Schneiders, D. Hartmann, M. Meinke, W. Schröder, An accurate moving
        boundary formulation in cut-cell methods, J. Comput. Phys. 235 (2013)
        786–809. https://doi.org/10.1016/j.jcp.2012.09.038.

[11]   V. Pasquariello, G. Hammerl, F. Örley, S. Hickel, C. Danowski, A. Popp,
        W.A. Wall, N.A. Adams, A cut-cell finite volume - finite element coupling
        approach for fluid-structure interaction in compressible flow, J. Comput.
        Phys. 307 (2016) 670–695. https://doi.org/10.1016/j.jcp.2015.12.013.

[12]   H. Choung, V. Saravanan, S. Lee, Jump-reduced immersed boundary
        method for compressible flow, Int. J. Numer. Methods Fluids. (2020) 1–27.
        https://doi.org/10.1002/fld.4821.

[13]   A. Chaudhuri, A. Hadjadj, A. Chinnayya, On the use of immersed boundary
        methods for shock/obstacle interactions, J. Comput. Phys. 230 (2011) 1731–
        1748. https://doi.org/10.1016/j.jcp.2010.11.016.

[14]   J.H. Seo, R. Mittal, A high-order immersed boundary method for acoustic
        wave scattering and low-Mach number flow-induced sound in complex
        geometries, J. Comput. Phys. 230 (2011) 1000–1019.
        https://doi.org/10.1016/j.jcp.2010.10.017.

[15]   J.H. Seo, R. Mittal, A sharp-interface immersed boundary method with

improved mass conservation and reduced spurious pressure oscillations, J. Comput. Phys. 230 (2011) 7347–7363. https://doi.org/10.1016/j.jcp.2011.06.003.

[16]   M.N. Linnick, H.F. Fasel, A high-order immersed interface method for simulating unsteady incompressible flows on irregular domains, J. Comput. Phys. 204 (2005) 157–192. https://doi.org/10.1016/j.jcp.2004.09.017.

[17]   C. Brehm, C. Hader, H.F. Fasel, A locally stabilized immersed boundary method for the compressible Navier-Stokes equations, J. Comput. Phys. 295 (2015) 475–504. https://doi.org/10.1016/j.jcp.2015.04.023.

[18]   H. Luo, H. Dai, P.J.S.A. Ferreira de Sousa, B. Yin, On the numerical oscillation of the direct-forcing immersed-boundary method for moving boundaries, Comput. Fluids. (2012). https://doi.org/10.1016/j.compfluid.2011.11.015.

[19]   C. Liu, C. Hu, An immersed boundary solver for inviscid compressible flows, Int. J. Numer. Methods Fluids. 85 (2017) 619–640. https://doi.org/10.1002/fld.4399.

[20]   C. Chi, B.J. Lee, H.G. Im, An improved ghost-cell immersed boundary method for compressible flow simulations, Int. J. Numer. Methods Fluids. 83 (2017) 132–148. https://doi.org/10.1002/fld.4262.

[21]   J. Yang, F. Stern, Sharp interface immersed-boundary/level-set method for wave-body interactions, J. Comput. Phys. 228 (2009) 6590–6616. https://doi.org/10.1016/j.jcp.2009.05.047.

[22]   Y.H. Tseng, J.H. Ferziger, A ghost-cell immersed boundary method for flow in complex geometry, J. Comput. Phys. 192 (2003) 593–623. https://doi.org/10.1016/j.jcp.2003.07.024.

[23]   M. Yousefzadeh, I. Battiato, High order ghost-cell immersed boundary method for generalized boundary conditions, Int. J. Heat Mass Transf. 137 (2019) 585–598. https://doi.org/10.1016/j.ijheatmasstransfer.2019.03.061.

[24]   F. De Vanna, F. Picano, E. Benini, A sharp-interface immersed boundary method for moving objects in compressible viscous flows, Comput. Fluids. 201 (2020) 104415. https://doi.org/10.1016/j.compfluid.2019.104415.

[25]   Y. Qu, R.C. Batra, Constrained moving least-squares immersed boundary method for fluid-structure interaction analysis, Int. J. Numer. Methods Fluids. 85 (2017) 675–692. https://doi.org/10.1002/fld.4400.

[26]   S.C. Schlanderer, G.D. Weymouth, R.D. Sandberg, The boundary data immersion method for compressible flows with application to aeroacoustics, J. Comput. Phys. 333 (2017) 440–461. https://doi.org/10.1016/j.jcp.2016.12.050.

[27]   R. Ghias, R. Mittal, H. Dong, A sharp interface immersed boundary method for compressible viscous flows, J. Comput. Phys. 225 (2007) 528–553. https://doi.org/10.1016/j.jcp.2006.12.007.

[28]   N. Peller, A. Le Duc, F. Tremblay, M. Manhart, High-order stable interpolations for immersed boundary methods, Int. J. Numer. Methods Fluids. (2006). https://doi.org/10.1002/fld.1227.

[29]   J. Yang, E. Balaras, An embedded-boundary formulation for large-eddy simulation of turbulent flows interacting with moving boundaries, J. Comput. Phys. 215 (2006) 12–40. https://doi.org/10.1016/j.jcp.2005.10.035.

[30]   C. Brehm, M.F. Barad, C. Hader, A High-Order Immersed Interface

Method for Compressible Flows, in: 2014. https://doi.org/10.2514/6.2014-2093.

[31]   A. Wiegmann, K.P. Bube, The explicit-jump immersed interface method: Finite difference methods for PDES with piecewise smooth solutions, 2000. https://doi.org/10.1137/S0036142997328664.

[32]   N. Peller, A. Le Duc, F. Tremblay, M. Manhart, High-order stable interpolations for immersed boundary methods, Int. J. Numer. Methods Fluids. 52 (2006) 1175–1193. https://doi.org/10.1002/fld.1227.

[33]   J. Zhu, J. Qiu, A new fifth order finite difference WENO scheme for solving hyperbolic conservation laws, J. Comput. Phys. 318 (2016) 110–121. https://doi.org/10.1016/j.jcp.2016.05.010.

[34]   C.-W. Shu, Essentially non-oscillatory and weighted essentially non-oscillatory schemes for hyperbolic conservation laws, in: 1998. https://doi.org/10.1007/bfb0096355.

[35]   M. Castro, B. Costa, W.S. Don, High order weighted essentially non-oscillatory WENO-Z schemes for hyperbolic conservation laws, J. Comput. Phys. (2011). https://doi.org/10.1016/j.jcp.2010.11.028.

[36]   G.S. Jiang, C.W. Shu, Efficient implementation of weighted ENO schemes, J. Comput. Phys. (1996). https://doi.org/10.1006/jcph.1996.0130.

[37]   K.H. Kim, C. Kim, Accurate, efficient and monotonic numerical methods for multi-dimensional compressible flows. Part II: Multi-dimensional limiting process, J. Comput. Phys. (2005). https://doi.org/10.1016/j.jcp.2005.02.022.

[38]   S. Kim, S. Lee, K.H. Kim, Wavenumber-extended high-order oscillation control finite volume schemes for multi-dimensional aeroacoustic computations, J. Comput. Phys. 227 (2008) 4089–4122. https://doi.org/10.1016/j.jcp.2007.12.013.

[39]   S. Osher, CONVERGENCE OF GENERALIZED MUSCL SCHEMES., SIAM J. Numer. Anal. (1985). https://doi.org/10.1137/0722057.

[40]   S. Gottlieb, C.-W. Shu, Total variation diminishing Runge-Kutta schemes, Math. Comput. Am. Math. Soc. (1998). https://doi.org/10.1090/s0025-5718-98-00913-2.

[41]   C.A. Felippa, B. Haugen, A unified formulation of small-strain corotational finite elements: I. Theory, Comput. Methods Appl. Mech. Eng. (2005). https://doi.org/10.1016/j.cma.2004.07.035.

[42]   H. Cho, H.S. Joo, S.J. Shin, H. Kim, Elastoplastic and contact analysis based on consistent dynamic formulation of co-rotational planar elements, Int. J. Solids Struct. 121 (2017) 103–116. https://doi.org/10.1016/j.ijsolstr.2017.05.019.

[43]   H. Cho, H. Kim, S.J. Shin, Geometrically nonlinear dynamic formulation for three-dimensional co-rotational solid elements, Comput. Methods Appl. Mech. Eng. (2018). https://doi.org/10.1016/j.cma.2017.08.037.

[44]   H. Cho, J.Y. Kwak, S.J. Shin, S.S. Lee, N.H. Lee, Flapping-wing fluid-structural interaction analysis using corotational triangular planar structural element, J. Aircr. (2016). https://doi.org/10.2514/1.J054567.

[45]   D. Levy, G. Puppo, G. Russo, Compact central WENO schemes for multidimensional conservation laws, SIAM J. Sci. Comput. (2001). https://doi.org/10.1137/S1064827599359461.

[46] M. Semplice, A. Coco, G. Russo, Adaptive Mesh Refinement for Hyperbolic Systems Based on Third-Order Compact WENO Reconstruction, J. Sci. Comput. (2016). https://doi.org/10.1007/s10915-015-0038-z.

[47] D. Gottlieb, M. Gunzburger, E. Turkel, On Numerical Boundary Treatment of Hyperbolic Systems for Finite Difference and Finite Element Methods, SIAM J. Numer. Anal. (1982). https://doi.org/10.1137/0719047.

[48] Z.J. Wang, Y. Sun, Curvature-based wall boundary condition for the Euler equations on unstructured grids, AIAA J. 41 (2003) 27–33. https://doi.org/10.2514/2.1931.

[49] M.E. Khalili, M. Larsson, B. Müller, High-order ghost-point immersed boundary method for viscous compressible flows based on summation-by-parts operators, Int. J. Numer. Methods Fluids. 89 (2019) 256–282. https://doi.org/10.1002/fld.4696.

[50] C.K.W. Tam, J. Fang, K.A. Kurbatskii, Non-homogeneous radiation and outflow boundary conditions simulating incoming acoustic and vorticity waves for exterior computational aeroacoustics problems, Int. J. Numer. Methods Fluids. 26 (1998) 1107–1123. https://doi.org/10.1002/(sici)1097-0363(19980515)26:9<1107::aid-fld689>3.0.co;2-n.

[51] E. Guilmineau, P. Queutey, A numerical simulation of vortex shedding from an oscillating circular cylinder, J. Fluids Struct. 16 (2002) 773–794. https://doi.org/10.1006/jfls.2002.0449.

[52] S. Lee, D. Bershader, Head-on parallel blade-vortex interaction, AIAA J. 32 (1994) 16–22. https://doi.org/10.2514/3.11945.

[53] M.P. Scully, Computation of helicopter rotor wake geometry and its influence on rotor harmonic airloads, Massachusetts Inst. Technol. ASRL TR. (1975) 470. http://scholar.google.com/scholar?hl=en&btnG=Search&q=intitle:Computation+of+Helicopter+Rotor+Wake+Geometry+and+its+Influence+on+Rotor+Harmonic+Airloads#0.

[54] E.O. M. Kouhi, G. Bugeda, A contribution to the Finite Element Analysis of High-Speed compressible flows and aerodynamic shape optimization, Monogr. Int. Cent. Numer. Methods Eng. 83 (2016) 69–73.

[55] G. Volpe, Performance of compressible flow codes at low Mach numbers, AIAA J. 31 (1993) 49–56. https://doi.org/10.2514/3.11317.

[56] M.D. Van Dyke, A.J. Guttmann, Subsonic potential flow past a circle and the transonic controversy, J. Aust. Math. Soc. Ser. B. Appl. Math. 24 (1983) 243–261. https://doi.org/10.1017/s0334270000002897.

[57] B.J. German, Laplacian equivalents to subsonic potential flows, AIAA J. 47 (2009) 129–141. https://doi.org/10.2514/1.36877.

[58] M.D. de Tullio, P. De Palma, G. Iaccarino, G. Pascazio, M. Napolitano, An immersed boundary method for compressible flows using local grid refinement, J. Comput. Phys. 225 (2007) 2098–2117. https://doi.org/10.1016/j.jcp.2007.03.008.

[59] P. Halder, S. De, K.P. Sinhamahapatra, N. Singh, Numerical simulation of shock-vortex interaction in Schardin's problem, Shock Waves. 23 (2013) 495–504. https://doi.org/10.1007/s00193-013-0448-5.

[60] S.M. Chang, K.S. Chang, On the shock-vortex interaction in Schardin's

problem, Shock Waves. 10 (2000) 333–343.
https://doi.org/10.1007/s001930000061.

[61] A.M. Khokhlov, Fully Threaded Tree Algorithms for Adaptive Refinement Fluid Dynamics Simulations, J. Comput. Phys. 143 (1998) 519–543. https://doi.org/10.1006/jcph.1998.9998.

[62] H. Tanno, K. Itoh, T. Saito, A. Abe, K. Takayama, Interaction of a shock with a sphere suspended in a vertical shock tube, Shock Waves. 13 (2003) 191–200. https://doi.org/10.1007/s00193-003-0209-y.

[63] J. Falcovitz, G. Alfandary, G. Hanoch, A Two-Dimensional Conservation Laws Scheme for Compressible Flows with Moving Boundaries, J. Comput. Phys. 138 (1997) 83–102. https://doi.org/10.1006/jcph.1997.5808.

[64] S. Brahmachary, G. Natarajan, V. Kulkarni, N. Sahoo, A sharp-interface immersed boundary framework for simulations of high-speed inviscid compressible flows, Int. J. Numer. Methods Fluids. 86 (2018) 770–791. https://doi.org/10.1002/fld.4479.

[65] Z. Du, J. Li, Accelerated piston problem and high order moving boundary tracking method for compressible fluid flows, SIAM J. Sci. Comput. 42 (2020) 1558–1581.

[66] J. Giordano, G. Jourdan, Y. Burtschell, M. Medale, D.E. Zeitoun, L. Houas, Shock wave impacts on deforming panel, an application of fluid-structure interaction, Shock Waves. 14 (2005) 103–110. https://doi.org/10.1007/s00193-005-0246-9.

[67] V. Pasquariello, G. Hammerl, F. Örley, S. Hickel, C. Danowski, A. Popp, W.A. Wall, N.A. Adams, A cut-cell finite volume - finite element coupling approach for fluid-structure interaction in compressible flow, J. Comput. Phys. (2016). https://doi.org/10.1016/j.jcp.2015.12.013.

[68] L. Wang, G.M.D. Currao, F. Han, A.J. Neely, J. Young, F.B. Tian, An immersed boundary method for fluid–structure interaction with compressible multiphase flows, J. Comput. Phys. 346 (2017) 131–151. https://doi.org/10.1016/j.jcp.2017.06.008.

[69] X. Zheng, Q. Xue, R. Mittal, S. Beilamowicz, A coupled sharp-interface immersed boundary-finite-element method for flow-structure interaction with application to human phonation, J. Biomech. Eng. 132 (2010) 1–12. https://doi.org/10.1115/1.4002587.

[70] J.D. Regele, D.R. Kassoy, O. V. Vasilyev, Effects of high activation energies on acoustic timescale detonation initiation, Combust. Theory Model. 16 (2012) 650–678. https://doi.org/10.1080/13647830.2011.647090.

[71] E.S. Oran, V.N. Gamezo, Origins of the deflagration-to-detonation transition in gas-phase combustion, Combust. Flame. 148 (2007) 4–47. https://doi.org/10.1016/j.combustflame.2006.07.010.

국문초록

　가상경계기법 (Immersed Boundary Method; IBM)을 이용한 압축성 전산 유동 해석시, 물체 주변 유동의 연속 및 불연속성에 따라 전산 해석에서 어려움이 발생한다. 본 연구에서는, 기존의 연속적 영역에서 발생하게 되는 저차의 IBM 의 정확도 문제와 불연속적 영역에서 발생 할 수 있는 고차 IBM 의 안정성 문제를 해결하기 위해 새로운 ghost-cell IBM 의 일환으로, 가중치가 적용된 가상경계기법 (Nonlinear Weighted Immersed Boundary Method; NWIBM)이 제안되었다. WENO 내삽 기법과 같이, 고차와 저차 내삽 다항식을 조합하여, 유동 상황에 맞는 적절한 가상경계의 ghost-cell 값을 구하게 된다. 다차원 연속 판별식을 고안하여 유동의 불연속성을 판단하였으며, 판별식에서 얻어진 비선형 가중치를 통해 연속적인 유동 영역에서는 고차 기법의 IBM 이, 불연속적인 유동 영역에서는 저차 기법의 IBM 이 지배적으로 사용되게 하였다. 또한, 충분한 유동의 연속성이 판별되게 되면, 기존 IBM 기법에서 발생하는 비약 불연속 (jump-discontinuity)을 감소시키기 위해 ghost-cell 에 인접한 유동영역을 재설계 (flow-field reconstruction) 하는 기법을 제안하였다. 본 연구에서는, 이러한 비선형 가중치 및 비약 불연속 감소를 위한 유동영역 재설계가 압축성 유동에서의 연속 및 불연속성에 따라 적절히 작동되며, 비물리적인 진동 감소 및 해석의 정확도를 높이는 것을 확인하였다.

주요 용어: 가상경계기법 (Immersed Boundary Method), 압축성 유동 (Compressible flow), 충격파 (Shock waves), 비선형 가중치 (Nonlinear weighting), 비약 불연속점 (Jump-discontinuity), 유체-구조 연성 (Fluid-Structure Interaction)

학번 : 2016-30193